NUCLEAR MODIFICATIONS OF PARTON DISTRIBUTION FUNCTIONS

A dissertation submitted
to Kent State University in partial
fulfillment of the requirements for the
degree of Doctor of Philosophy

by

Adeola Adeleke Adeluyi

August 2009

Dissertation written by

Adeola Adeleke Adeluyi

M. Sc., Obafemi Awolowo University (Nigeria), 2000

DICTP, International Center for Theoretical Physics (Italy), 2001

Ph. D., Kent State University (USA), 2009

Approved by

_____ Chair, Doctoral Dissertation Committee
Dr. George Fai

_____ Members, Doctoral Dissertation Committee
Dr. Declan Keane

_____
Dr. Peter C. Tandy

_____
Dr. Laura Leff

Accepted by

_____ Chair, Department of Physics
Dr. Bryon D. Anderson

_____ Dean, College of Arts and Sciences
Dr. Timothy S. Moerland

TABLE OF CONTENTS

List of Figures vi

Acknowledgements xi

1 Introduction **1**

1.1 Overview 1

1.1.1 High energy nuclear collisions 1

1.1.2 Theoretical methods in high-energy nuclear collisions 2

1.1.3 Quantum Chromodynamics 3

1.1.4 Quark-Gluon Plasma 3

1.1.5 Chiral symmetry 4

1.1.6 Hot and dense nuclear matter 4

1.1.7 Parton model, pQCD, and factorization 5

1.2 Outline of this work 6

2 Parton Distribution Functions of Free Nucleons **8**

2.1 Introduction 8

2.2 Parton distributions 8

2.2.1 Intuitive meaning of parton distribution functions 8

2.2.2 Factorization 9

2.2.3 Significance of PDFs 10

2.3 Translation to operators 11

2.3.1 Light-front coordinates 12

2.3.2 The quark distribution function 13

2.3.3 Gauge invariance 13

2.3.4 Interpretation of the eikonal gauge operator 14

2.3.5 Renormalization 14

2.3.6 Antiquarks and gluons . . . 16
2.4 Renormalization group . . . 17
2.5 Parton distributions of free nucleons . . . 18
2.5.1 Deep inelastic scattering: kinematics and structure functions . . . 19
2.5.2 Bjorken scaling . . . 21
2.5.3 Parton model . . . 22
2.5.4 Virtual Compton scattering . . . 23
2.5.5 QCD-improved parton model . . . 25
2.5.6 Global fits to nucleon parton distributions . . . 26

3 Nuclear Modifications **30**
3.1 Introduction . . . 30
3.2 Nuclear DIS and modifications of parton distributions . . . 30
3.2.1 Nuclear structure functions . . . 31
3.2.2 Nuclear Ratio . . . 32
3.2.3 Other measurements of nuclear parton distributions . . . 36
3.2.4 Global fits to nuclear parton distributions . . . 38
3.2.5 Importance of Shadowing . . . 40

4 Nuclear Shadowing at Small x from Gribov Theory **42**
4.1 Introduction . . . 42
4.2 Shadowing Ratio and Generalized Gribov Theory . . . 43
4.2.1 Nuclear Shadowing Ratio . . . 43
4.2.2 Gribov Theory . . . 44
4.2.3 Shadowing Correction From Generalized Gribov Theory . . . 45
4.3 Diffractive Dissociation . . . 48
4.3.1 Diffractive production . . . 48
4.3.2 Diffractive dissociation cross section . . . 49
4.4 Data Analysis and Fits . . . 51

4.4.1 FNAL Data . . . 52
4.4.2 HERA Data . . . 52
4.4.3 $W \simeq 24$ GeV . . . 53
4.5 Results: Shadowing Ratio and Mass Dependence . . . 56
4.5.1 Shadowing: NMC . . . 57
4.5.2 Shadowing: E665 . . . 57
4.5.3 Mass Dependence of Shadowing At Small x . . . 61
4.6 A simple approximate picture of small-x shadowing . . . 61
4.7 Comparison with other related approaches and theoretical uncertainties . . . 62
4.7.1 Comparison . . . 62
4.7.2 Uncertainties . . . 64

5 Nuclear Parton Distributions and Deuteron-Gold (d+Au) Collisions 67
5.1 Introduction . . . 67
5.2 Deuteron-gold Collisions: Basic Formalism . . . 69
5.3 Minimum Bias Nuclear Modification Factor . . . 72
5.4 Central-to-Peripheral Ratios . . . 77
5.5 Pseudorapidity Asymmetry . . . 81
5.5.1 Pseudorapidity and nuclear modifications . . . 82
5.5.2 Minimum-bias asymmetry: $|\eta| \leq 0.5$ . . . 82
5.5.3 Centrality-selected asymmetry: $|\eta| \leq 0.5$ . . . 85
5.5.4 Minimum-bias asymmetry: $0.5 \leq |\eta| \leq 1.0$ . . . 87
5.5.5 Centrality-selected asymmetry: $0.5 \leq |\eta| \leq 1.0$ . . . 87

6 Summary and Conclusion 93

A Kinematics 96
A.1 Minkowski four-vectors and scalar product . . . 96
A.2 Gamma Matrices . . . 96

A.3 Mandelstam variables 97
A.4 Light-cone coordinates 97
A.4.1 Definitions 97
A.5 Rapidity and Pseudorapidity 98
A.5.1 Rapidity 98
A.5.2 Pseudorapidity 101

B Triple-Regge Model of High-Mass Continuum **102**

LIST OF FIGURES

2.1 Hadron A + hadron $B \rightarrow$ 2 partons. 9

2.2 Deeply inelastic scattering. 11

2.3 World lines of the partons in a fast-moving proton. 12

2.4 Effect of the eikonal gauge operator. 15

2.5 An ultraviolet divergent diagram when integration over components of the quark momentum is carried out. 16

2.6 A quark can fluctuate into a quark plus a gluon in a small space-time volume. . . . 17

2.7 Evolution of the gluon distribution between $\mu = 10\,GeV$ and $\mu = 100\,GeV$. 18

2.8 Inclusive deep-inelastic lepton-nucleon scattering. The virtual photon momentum is q. The final hadronic state is not measured, and is denoted by X. 19

2.9 Gluon and up quark distributions in the proton according to the CTEQ3M parton distribution set at $\mu = 20$ GeV. 29

3.1 Schematic behavior of $R^A_{F_2}(x, Q^2)$ as a function of x for a given fixed Q^2. 33

3.2 Structure function ratio for some nuclei. 34

4.1 Illustration of Gribov's Theorem: The forward hadron-deuteron rescattering amplitude giving rise to the nuclear shadowing is proportional to the differential hadron-nucleon diffractive cross section at small momentum transfer ($t \sim 0$). 45

4.2 Double scattering contribution to shadowing correction, $\delta\sigma_{\gamma^* A}$ 46

4.3 Diffractive scattering from a proton. 49

4.4 (Color Online) Triple-Regge fit to the FNAL (12.8 GeV and 15.2 GeV) and HERA (187 GeV and 231 GeV) data in the nonresonant continuum ($M_X^2 > 4$ GeV^2). The dashed lines correspond to pomeron+reggeons. The shaded circles are experimental data. 54

4.5 (Color Online) Estimates for the fit parameters at $W = 24$ GeV as discussed in the text. The shaded upright triangles and squares are the $G_{\mathbb{P}\mathbb{P}\mathbb{P}}(0)$ and $G_{\mathbb{P}\mathbb{P}\mathbb{R}}(0)$ from Eq. (4.26) respectively. The dashed and dot-dashed lines are fits to the parameters respectively. The vertical dotted line corresponds to the values of these parameters at $W = 24$ GeV. 55

4.6 (Color Online) Shadowing ratio at FNAL energies. The thick lines correspond to pomeron+subleading reggeons with $\eta = 1$ while the dashed lines correspond to pomeron+reggeons with $\eta = -1$. The full triangles are data from the NMC experiment. 58

4.7 (Color Online) Shadowing ratio at $W = 24$ GeV. The thick line is the result from both pomeron and subleading reggeons with $\eta = 1$ while the dashed line corresponds to pomeron+reggeons with with $\eta = -1$. The full triangles are data from the E665 experiment. 59

4.8 (Color Online) Mass dependence of calculated shadowing ratio at small x for both the NMC (shaded squares) and E665 (shaded diamonds) kinematics. The dashed lines are fits according to Eq. (4.34) as described in the text. 60

4.9 (Color Online) Shadowing ratio calculated for different values of the diffractive slope B. Data are from the NMC (shaded circles) and E665 (shaded triangles) collaborations. 63

4.10 (Color Online) Calculated uncertainties as discussed in the text for $\eta_{\mathbb{R}} = 1$. From top: $W = 24$ GeV, $W = 15.5$ GeV. 66

5.1 (Color Online) $x_{b_{\min}}$ as a function of p_T for the four BRAHMS pseudorapidity intervals. The horizontal dashed line corresponds to $x_{bmin} = 0.05$, the approximate upper limit for shadowing. 75

5.2 (Color Online) Minimum bias nuclear modification factor R_{dAu} for total charged hadron production at different pseudorapidities. The solid line represents the EPS08 nPDFS (upper panels) and the FGS nPDFs (lower panels). The dashed line corresponds to the HKN07 LO (NLO) nPDFs for upper (lower) panels respectively. In the intervals $|\eta| \leq 0.2$ and $0.8 \leq \eta \leq 1.2$, the data are for average charged hadrons, while for the intervals $1.9 \leq \eta \leq 2.35$ and $2.9 \leq \eta \leq 3.5$, only negative hadrons are measured. The error bars represent statistical errors. 76

5.3 (Color Online) Central-to-peripheral ratio R_{CP} for total charged hadron production at different pseudorapidities. The solid line represents the EPS08 nPDFS (upper panels) and the FGS nPDFs (lower panels). The dashed line corresponds to the HKN07 LO (NLO) nPDFs for upper (lower) panels respectively. Solid triangles denote BRAHMS data. In the intervals $|\eta| \leq 0.2$ and $0.8 \leq \eta \leq 1.2$, the data are for average charged hadrons, while for the intervals $1.9 \leq \eta \leq 2.35$ and $2.9 \leq \eta \leq 3.5$, only negative hadrons are measured. The solid error bars are systematic errors, while dashed error bars represent statistical errors. 78

5.4 (Color Online) Semicentral-to-peripheral ratio R_{CP} for total charged hadron production at different pseudorapidities. The solid line represents the EPS08 nPDFS (upper panels) and the FGS nPDFs (lower panels). The dashed line corresponds to the HKN07 LO (NLO) nPDFs for upper (lower) panels respectively. Solid triangles denote BRAHMS data. In the intervals $|\eta| \leq 0.2$ and $0.8 \leq \eta \leq 1.2$, the data are for average charged hadrons, while for the intervals $1.9 \leq \eta \leq 2.35$ and $2.9 \leq \eta \leq 3.5$, only negative hadrons are measured. The solid error bars are systematic errors, while dashed error bars represent statistical errors. 80

5.5 (Color Online) Nuclear modifications, R_{dAu}, (left panels), and pseudorapidity asymmetry, Y_{asy}, (right panels), for pions at $|\eta| \leq 0.5$ and $0.5 \leq |\eta| \leq 1.0$ using EPS08 and HKN07 LO nPDFs. Filled triangles denote the STAR data. 83

5.6 (Color Online) Pseudorapidity asymmetry, Y_{asy} for different hadrons at $|\eta| \leq 0.5$. The solid line represents the EPS08 nPDFs (upper panels) and the FGS nPDFs (lower panels). The dashed line corresponds to the HKN07 LO (NLO) nPDFs for upper (lower) panels respectively. Filled triangles denote the STAR data. The solid error bars are systematic errors, while dashed error bars represent statistical errors. 84

5.7 (Color Online) Pseudorapidity asymmetry, Y_{asy}, for pions in two centrality classes at $|\eta| \leq 0.5$. The solid line represents the EPS08 nPDFs (upper panels) and the FGS nPDFs (lower panels). The dashed line corresponds to the HKN07 LO (NLO) nPDFs for upper (lower) panels respectively. Filled squares denote the STAR data. 86

5.8 (Color Online) Pseudorapidity asymmetry, Y_{asy}, for protons in two centrality classes at $|\eta| \leq 0.5$. The solid line represents the EPS08 nPDFs (upper panels) and the FGS nPDFs (lower panels). The dashed line corresponds to the HKN07 LO (NLO) nPDFs for upper (lower) panels respectively. Filled squares denote the STAR data. 88

5.9 (Color Online) Pseudorapidity asymmetry, Y_{asy} for different hadrons at $0.5 \leq |\eta| \leq 1.0$. The solid line represents the EPS08 nPDFs (upper panels) and the FGS nPDFs (lower panels). The dashed line corresponds to the HKN07 LO (NLO) nPDFs for upper (lower) panels respectively. Filled triangles denote the STAR data. The solid error bars are systematic errors, while dashed error bars represent statistical errors. 89

5.10 (Color Online) Pseudorapidity asymmetry, Y_{asy}, for pions in two centrality classes at $0.5 \leq |\eta| \leq 1.0$. The solid line represents the EPS08 nPDFs (upper panels) and the FGS nPDFs (lower panels). The dashed line corresponds to the HKN07 LO (NLO) nPDFs for upper (lower) panels respectively. Filled squares denote the STAR data. 90

5.11 (Color Online) Pseudorapidity asymmetry, Y_{asy}, for protons in two centrality classes at $0.5 \leq |\eta| \leq 1.0$. The solid line represents the EPS08 nPDFs (upper panels) and the FGS nPDFs (lower panels). The dashed line corresponds to the HKN07 LO (NLO) nPDFs for upper (lower) panels respectively. Filled squares denote the STAR data. 92

B.1 Triple-Regge model of difractive dissociation cross section 102

ACKNOWLEDGMENTS

The support and guidance of my research advisor, Prof. George Fai, is gratefully acknowledged. I am thankful for his patience, genuine interest, and kind advice through the years. I also acknowledge, with deep gratitude, the immense benefit I have derived from collaborating with Dr. Peter Levai and Dr. Gergely Barnafoldi. I especially wish to thank Dr. Gergely Barnafoldi for intellectual stimulations and exemplary kindness to me and my family.

Mr. Greg Putman has been of great help in diverse ways. I gratefully acknowledge his assistance. Lastly, I am highly indebted to my family for their support and understanding.

CHAPTER 1

INTRODUCTION

1.1 Overview

1.1.1 High energy nuclear collisions

The study of ultrarelativistic heavy-ion collisions can be thought of as an intradisciplinary field, which primarily connects high-energy physics of elementary particles with nuclear physics, and in addition has links to condensed matter physics, statistical physics, and astrophysics. Typically, high-energy elementary particle physics deals with structureless particles, and the interactions, mediated by gauge bosons, are derived from "first principles" (local gauge symmetries). Nuclear physics, on the other hand, deals with extended, complicated objects (nuclei) of many degrees of freedom, and the interactions are described by effective models. In the field of high-energy nuclear collisions, one tries to analyze the properties of nuclear/hadronic matter in terms of fundamental interactions.

The first experiments with ultrarelativistic heavy ions (i.e., with energies exceeding 10 GeV per nucleon in the projectile beam) took place at Brookhaven National Laboratory (BNL) and at the European Organization for Nuclear Research (CERN) in 1986. In 2000, the first data from the Relativistic Heavy Ion Collider (RHIC) were collected. RHIC was designed to accelerate fully stripped Au ions to a collision center-of-mass energy of 200 GeV per nucleon pair. The design luminosity corresponds to approximately 1400 Au+Au collisions per second. During the first year in 2000, the maximum energy of 130 GeV per nucleon pair was achieved. First collisions took place in June 2000 and the run continued till the end of August. In the years $2001 - 2004$ the next three runs took place with the maximum energy of 200 GeV per nucleon pair. One of these runs plus a high-statistics run in 2008 were devoted to the study of deuteron-gold collisions, which were studied in order to get the proper reference point for the more complicated gold on gold collisions.

Four experiments have taken data at RHIC: BRAHMS, PHOBOS, PHENIX, and STAR. The

two smaller experiments are BRAHMS and PHOBOS, and the two larger experiments are PHENIX and STAR. The experimental aim of BRAHMS was particle identification over a broad rapidity range (nearly 12 units). PHOBOS was designed to examine and analyze a very large number of unselected gold ions collisions. The PHENIX experiment measures electrons, muons, hadrons and photons. The STAR experiment concentrates on measurements of hadron production over a large solid angle. Future developments in the field are expected from the operation of the Large Hadron Collider (LHC) at CERN.

1.1.2 Theoretical methods in high-energy nuclear collisions

In ultrarelativistic heavy ion collisions, very large numbers of particles are produced (referred to as large multiplicities). For example, in Au+Au central collisions at RHIC, the total charged particle multiplicity is about 4200. Hence the number of produced particles exceeds the number of initial nucleons by a factor of 10. In this situation different theoretical methods are used, some borrowed from the description of large macroscopic systems, e.g., thermodynamics, hydrodynamics, kinetic (transport) theory, field theory at finite temperature and density, nonequilibrium field theory, Monte-Carlo simulations.

Many estimates of effects in high-energy nuclear collisions are done on the basis of purely thermodynamics or statistical considerations. However, the hadronic systems produced in the collisions are not static; thus the need for a dynamical description, which frequently involves rich applications of relativistic hydrodynamics. Furthermore, since the matter produced in the collisions lives only for a short while (thermalization or isotropization time $\tau \approx 0.17$ fm at RHIC), it is natural to expect that its space-time evolution proceeds far from equilibrium – thus the development and application of transport theories, which are suitable for the description of nonequilibrium processes. To a large extent, the successful modeling of ultrarelativistic reactions has been obtained with the help of microscopic Monte-Carlo simulations. Lastly, it is worth noting that the physics of ultrarelativistic heavy-ion collisions has benefitted from, and has also been instrumental in, developments in both equilibrium and nonequilibrium field theory.

1.1.3 Quantum Chromodynamics

In general, during high-energy nuclear collisions, a many-body system of strongly interacting particles is produced. The fundamental theory of the strong interactions is Quantum Chromodynamics (QCD), the theory of quarks and gluons which are confined in hadrons (baryons and mesons). Confinement is the most striking feature of QCD, though its physical nature still remains unclear. The intuitive picture of confinement can be illustrated by the concept of a string between quarks when we try to separate them. If the quarks are pulled apart too far, large energy is deposited in the string and it breaks into pieces. As a result the quarks form new hadrons from pieces of the initial string.

On the other hand, quarks and gluons interact weakly at small distances, or equivalently, at high energies. This phenomenon is called asymptotic freedom. It allows us to "observe" the quark and gluon degrees of freedom in highly energetic collisions. Indeed, the internal structure of hadrons was revealed in the deep inelastic electron collision experiments performed in the late sixties. This is the regime where perturbative techniques are applicable, termed perturbative QCD (pQCD).

At present, the nuclear force between baryons and mesons can be viewed as a residual of the force acting between quarks and gluons, similar to the way the chemical (van der Waals) force is the residual electromagnetic interaction. Since QCD is a complicated non-linear theory, the complete description of relativistic heavy-ion collisions based exclusively on first principles is impossible in practice. Thus very often effective models have to be employed, although QCD can be successfully applied to describe many subprocesses of the complicated collisions.

1.1.4 Quark-Gluon Plasma

The main challenge of ultrarelativistic heavy-ion collisions is the observation of the two phase transitions predicted by QCD, i.e., the deconfinement and chiral phase transitions. In the normal world (i.e., at low energy densities) quarks and gluons are confined in hadrons. However, with increasing temperature (heating) and/or increasing baryon density (compression), a phase transition can occur to the state where the ordinary hadrons do not exist anymore, and where quarks and gluons become the relevant degrees of freedom. Since the interaction of quarks and gluons is weaker at

high energies, we expect that this new state of matter may behave as a gas of weakly interacting constituents, the so-called quark-gluon plasma (QGP).

The present experimental evidence indicates that an extended and very dense system of hadronic matter is indeed formed in heavy nucleus-nucleus collisions. It behaves like a perfect fluid though, not a gas of weakly interacting constituents. Further progress is expected at LHC.

1.1.5 Chiral symmetry

There exists six different types (flavors) of quarks: up, down, strange, charmed, bottom and top. In our world the most common hadrons, protons, neutrons, and pions, are made of up and down quarks. The masses of these quarks are very small, and so are usually ignored in practical calculations. Consider now the subsector of QCD describing only these two quarks. In the limit of vanishing masses, the left- and right-handed quarks become decoupled and QCD becomes invariant under their interchange, leading to separate current conservations. This symmetry implies that each state should have a degenerate partner of opposite parity, contrary to observations. The paradox is resolved by the phenomenon of spontaneous breakdown of chiral symmetry, involving pseudoscalar pions as the Goldstone bosons.

In a very hot and dense hadronic medium, ordinary hadrons lose their identities and the quark-gluon plasma is produced. In this case the ground state of the strong interactions is significantly modified and the chiral symmetry is expected to be restored. Observation of chiral phase restoration is an exciting prospect of experiments with heavy ions.

1.1.6 Hot and dense nuclear matter

The study of high-energy nuclear reactions gives us important information about properties of hot and dense hadronic matter. Heavy-ion collisions are the only way to compress and heat up nuclear matter under laboratory conditions. Information extracted from data can be useful for construction of models of neutron stars and supernova explosions. Even at energies of tens of MeV per nucleon, one encounters many interesting and well established phenomena like collective flows or

subthreshold particle production.

1.1.7 Parton model, pQCD, and factorization

The parton model is applicable, with varying degrees of accuracy, to any hadronic cross section involving a large momentum transfer. It is in essence a generalization of the impulse approximation. We assume that any physically observed hadron, of momentum p^μ (see Appendix A), is made up of constituent particles, its "partons", which can be identified with quarks and gluons, the QCD degrees of freedom. At high energy the masses of hadrons and partons are neglected compared to the scale Q of the hard scattering. Furthermore, it is assumed that every relevant parton entering the hard scattering from an initial-state hadron has momentum xp^μ, with $0 \leq x \leq 1$; here p^μ is the momentum of the parent hadron. Parton-model cross sections are calculated from tree graphs (no loops) for partonic scattering, by combining them with probability densities, the parton distribution functions (PDFs). The PDFs are the probability densities of finding a parton of a given type in a hadron, with a momentum fraction x. In the naive parton model, these distributions depend only on x, and are not explicitly dependent on the momentum transferred Q^2. This is known as scaling. The PDFs are determined from structure functions measured in deep inelastic scattering.

Scaling is only approximate. The structure functions are known to depend on the momentum transferred Q^2, although rather weakly. Thus the PDFs also depend on Q^2, a condition referred to as scaling violation. This dependence is described by pQCD. Thus although the PDFs are not calculable in pQCD, their evolution with Q^2 is perturbatively calculable. Perturbative QCD also gives the general framework in which to calculate higher-order terms in the hard scattering; thus the parton model can be regarded as the lowest-order (only tree graphs) term in a systematic expansion under pQCD.

The general picture is thus as follows: to describe processes involving hadrons one separates the long distance (nonperturbative) parts from the short distance (perturbative) parts, a procedure known as factorization. The perturbative part (hard scattering) is calculable order by order in pQCD. The nonperturbative parts (for example the PDFs) are taken from experiments. This framework is

general enough not only for describing hadron-hadron collisions but also nucleus-nucleus collisions.

1.2 Outline of this work

In Chapter 2 we review parton distribution functions (PDFs) of free nucleons. This is a very vast subject, spanning both perturbative and nonperturbative aspects of Quantum Chromodynamics (QCD). An important topic is the technical definition of PDFs and their scaling violations, described by complex integro-differential evolution equations. These are deeply technical subjects, and we limit ourselves to a very brief review. More detailed and thorough treatments can be found in the various references cited in Chapter 2. Due to the inherently nonperturbative nature of the PDFs, first-principle derivations are still lacking, and they are thus most economically determined from experimental data on structure functions, especially from deeply inelastic scattering (DIS). We therefore also briefly review DIS and the approach to global analyses (global fits) of parton distributions.

The review of parton distributions in free nucleons sets the stage for a discussion of nuclear modifications to PDFs of free nucleons in Chapter 3, leading to nuclear parton distribution functions (nPDFs). Due to the limited availability of data on nuclear deeply inelastic scattering (nuclear DIS), nuclear modifications are parameterized in terms of ratios of the nuclear structure functions and free nucleon structure functions, termed nuclear ratios. The nPDFs are then expressed as a convolution of nuclear ratios and nuclear structure functions. We thus review in Chapter 3 nuclear DIS, nuclear ratios and, similar to the case of free nucleons, global fits to nuclear parton distributions.

Our original contributions are contained in Chapters 4 and 5. These two chapters are in some sense complementary, but the issues addressed in Chapter 4 directly affect the calculations presented in Chapter 5. Chapter 4 deals with the theoretical description of nuclear modifications in a special kinematic regime: small x and low Q^2. This is the regime relevant to the currently available data on small x from fixed-target experiments. We utilize Gribov theory, suitably generalized, and information on diffractive dissociation to describe nuclear modifications at small x (nuclear shadowing). We also investigate the mass dependence of these modifications. It should be borne in mind that nuclear modifications are encoded in nuclear parton distributions, which are a necessary ingredient

for the calculation of observables in Chapter 5.

We address ultrarelativistic nuclear collisions in Chapter 5. In view of the serious complications and diverse effects present in relativistic heavy nucleus-nucleus collisions, we focus attention on a relatively simpler and "cleaner" system: deuteron-gold (d+Au) collisions. Even in this simpler system, the description of relativistic collisions is still quite complex. To this end we apply existing nuclear PDFs (nPDFs) to calculate observables experimentally sensitive to nuclear modifications, and compare with available experimental data. We use three different parameterizations of nPDFs, first in order to assess their performances, and secondly to investigate the level of theoretical uncertainty emanating from our present understanding of nPDFs. The observables calculated are the deuteron-gold nuclear modification factors and the pseudorapidity asymmetries.

We summarize and conclude our investigations in Chapter 6.

CHAPTER 2

PARTON DISTRIBUTION FUNCTIONS OF FREE NUCLEONS

2.1 Introduction

In this Chapter we review basic information on parton distribution functions: their technical definition and determination from deeply inelastic scattering (DIS). Parton distribution functions (PDFs) give the probability to find partons (quarks and gluons) in a hadron as a function of the fraction x of the hadron's momentum carried by the parton. They are formally defined in terms of matrix elements of certain operators. In practice they are determined from experimental results on high-energy scattering of leptons and nucleons. The material presented in this review is essentially from [1] and [2] where further details can be found.

2.2 Parton distributions

2.2.1 Intuitive meaning of parton distribution functions

Parton distribution functions are defined in the framework of pQCD. Let $d\sigma$ be a cross section involving short distances. For instance, we may consider the process hadron A + hadron $B \rightarrow$ jet + X at a collider. A jet is an arbitrary set of hadrons contained within a small cone of opening angle δ and with a fixed total momentum; X denotes other reaction products. Let the jet have a high transverse momentum P_T. Intuitively, the observed jet begins as a single quark or gluon that emerges from a parton-parton scattering event with large P_T, as illustrated in Fig. 2.1. (Typically, this parton recoils against a single parton that carries the opposite P_T.) The large P_T parton fragments into the observed jet of hadrons.

The physical picture illustrated in Fig. 2.1 suggests how we may write the cross section to produce the jet as a product of three factors. A parton of type a comes from a hadron of type A. It

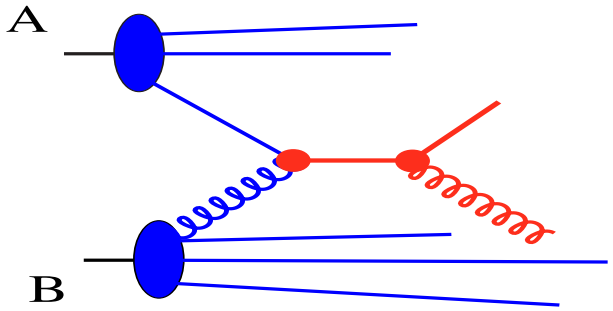


Fig. 2.1: Hadron A + hadron $B \to 2$ partons.

carries a fraction x_A of the hadron's momentum. The probability to find it is given by $f_{a/A}(x_A)\, dx_A$. A second parton of type b comes from a hadron of type B. It carries a fraction x_B of the hadron's momentum. The probability to find it is $f_{b/B}(x_B)\, dx_B$. The functions $f_{a/A}(x)$ are the parton distribution functions that are the subject of this review. The third factor is the cross section for the partons to make the observed jet, $d\hat{\sigma}$. This parton level cross section is calculated using perturbative QCD. (Parton-level variables conventionally carry a hat, like $d\hat{\sigma}$ above).

2.2.2 Factorization

We have been led by the intuitive parton picture of Fig. 2.1 to write the cross section for jet production in the following form

$$\frac{d\sigma}{dP_T} \sim \sum_{a,b} \int dx_A\, f_{a/A}(x_A,\mu) \int dx_B\, f_{b/B}(x_B,\mu)\, \frac{d\hat{\sigma}}{dP_T}\,. \tag{2.1}$$

Here the summation takes into account various partons in A and B, and the parton level cross section has a well behaved expansion in powers of α_s, the strong coupling constant:

$$\frac{d\hat{\sigma}}{dP_T} \sim \sum_N \left(\frac{\alpha_s(\mu)}{\pi}\right)^N H_N(x_A, x_B, P_T; a, b; \mu)\,. \tag{2.2}$$

The coefficients H_N are calculable in perturbative QCD.

The principle of *factorization* asserts that eq. (2.2) holds up to corrections of order $(m/P_T)^n$ where m is a typical hadronic mass scale and the power n depends on the process, and $(\alpha_s(\mu))^L$

from truncating the expansion of $d\hat{\sigma}/dP_T$. For the present study, we can regard factorization as an established theorem of perturbative QCD. A review may be found in Ref. [3].

As we have seen, Eq. (2.1) has a simple intuitive meaning. However, the appearance of a parameter μ in eq. (2.1) hints that there is more to the equation than just a model. The parameter μ, which has dimensions of mass, is related to the renormalization of the strong coupling $\alpha_s(\mu)$ and of the operators in the definition of the parton distribution functions $f_{a/A}(x_A, \mu)$. In principle two separate parameters can appear in these two places. In practice it is sufficient to use the same parameter. (This parameter is denoted by either μ or Q^2 in the following.)

At the lowest order (Born level), the parton cross section $d\hat{\sigma}/dP_T$ is calculated in a straightforward manner. At the next-to-leading order and beyond, the calculation is not so straightforward. Various divergences appear in a naive calculation. By a procedure called renormalization, the divergences are removed and, in any finite-order perturbative calculation, the dependence on the scale μ appears in their place. The precise rules for calculating $d\hat{\sigma}/dP_T$ follow once the definition of the parton distribution functions $f_{a/A}(x, \mu)$ has been set.

2.2.3 Significance of PDFs

Knowledge of parton distribution functions is necessary for the description of hard processes in pQCD with one or two hadrons in the initial state. With two hadrons in the initial state, as at Fermilab, RHIC, or the Large Hadron Collider (LHC), observed short distance cross sections take the form

$$d\sigma \sim \sum_{a,b} \int dx_A \, f_{a/A}(x_A, \mu) \int dx_B \, f_{b/B}(x_B, \mu) \, d\hat{\sigma} \, . \tag{2.3}$$

With one hadron in initial state, as in deeply inelastic lepton scattering at HERA (Fig. 2.2), the cross section has the form

$$d\sigma \sim \sum_{a} \int dx_A \, f_{a/A}(x_A, \mu) \, d\hat{\sigma}. \tag{2.4}$$

In either case, one has no predictions without knowledge of the parton distribution functions.

The essence of Eqs. (2.3) and (2.4) above is that in high-energy short distance collisions, a hard scattering probes the system quickly, while the strong binding forces act slowly. Thus one needs to

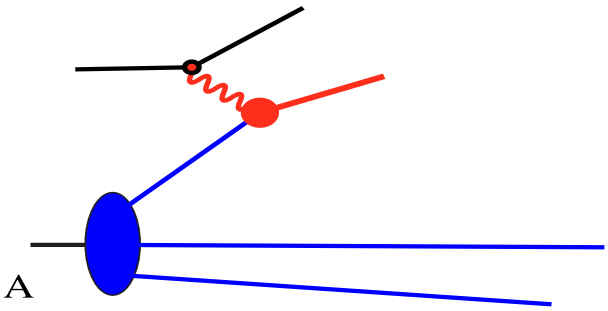


Fig. 2.2: Deeply inelastic scattering.

know probabilities to find partons in a fast moving hadron as seen by an approximately instantaneous probe. This is the information encoded in the parton distribution functions. This information is not only useful, but also valuable in understanding hadron structure. Parton distribution functions are not everything, however. They provide a relativistic view only, a view quite different from the view that might be most economical for the description of a hadron at rest. Furthermore, they provide no information on correlations among the partons.

2.3 Translation to operators

We briefly review a technical definition of parton distribution functions. The detailed treatment is quite involved and lengthy, here we summarize it for completeness. There are, in fact, two definitions in current use. We will describe the $\overline{\rm MS}$ definition, which is the most commonly used. (The designation $\overline{\rm MS}$ originally comes from "modified minimal subtraction" scheme). There is also a DIS definition, in which deeply inelastic scattering plays a privileged role. This is treated thoroughly in the CTEQ Collaboration's *Handbook of Perturbative QCD* [4] . There are also different ways to think about the $\overline{\rm MS}$ definition. Here, parton distributions are defined directly in terms of field operators along a light-like line, as in [5]. An equivalent construction from a different point of view may be found in [6]. Also, moments of the parton distribution functions are related to matrix elements of certain local operators, which appear in the operator product expansion for deeply inelastic scattering. This relation could be also used as the definition.

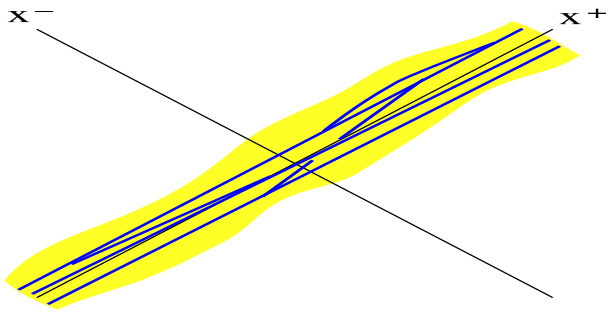


Fig. 2.3: World lines of the partons in a fast-moving proton.

It is important to distinguish between the parton distribution functions $f_{a/A}(x,\mu)$ and the structure functions $F_1(x,Q^2)$, $F_2(x,Q^2)$, and $F_3(x,Q^2)$ that are measured in deeply inelastic lepton scattering. Their connection in the framework of the QCD-improved parton model is displayed in Eq. (2.35)

2.3.1 Light-front coordinates

We use light-front coordinates and momenta defined by (see Appendix A)

$$x^{\pm} = (x^0 \pm x^3)/\sqrt{2}\,, \quad P^{\pm} = (P^0 \pm P^3)/\sqrt{2}\,. \tag{2.5}$$

Consider a highly relativistic (strongly Lorentz-boosted) proton, i.e. a proton with a big P^+, a small P^-, and $\vec{P}_T = 0$. The partons in such a proton move roughly parallel to the x^+ axis, as illustrated in Fig. 2.3. PDFs are defined by taking a snapshot of the proton on a plane of equal x^+ in Fig. 2.3. This definition is motivated by field theory quantized on planes of equal x^+ [3]. The $A^+ = 0$ gauge is used, where A^μ is the gluon field operator. The removal of this restriction will be discussed in Eq. (2.9). One can treat x^+ as "time," so that the system propagates from one plane of equal x^+ to another. For our fast moving proton, the interval in x^+ between successive interactions among the partons is typically large.

The invariant dot product between P^μ and x^μ is

$$P \cdot x = P^+x^- + P^-x^+ - \vec{P}_T \cdot \vec{x}_T\,. \tag{2.6}$$

2.3.2 The quark distribution function

Let $|P\rangle$ be the state vector for a hadron of type A carrying momentum P^μ. Take the hadron to be spinless in order to simplify the notation. Construct the unrenormalized (^{0}) distribution function (renormalization will be discussed in Sec. 2.3.5) for finding quarks of flavor j in hadron A as

$$f_{j/A}^{(0)}(x)\ \langle P^{+\prime}, \vec{P}_T' | P^+, \vec{P}_T \rangle = \frac{1}{2x(2\pi)^3} \int d\vec{k}_T \sum_s \langle P^{+\prime}, \vec{P}_T' |\, b_j^\dagger(xP^+, \vec{k}_T; s; x^+) \\ b_j(xP^+, \vec{k}_T; s; x^+) | P^+, \vec{P}_T \rangle \ , \qquad (2.7)$$

where b_j and $b_j^\dagger$ are quark annihilation and creation operators respectively. In Eq. (2.7) there are factors relating to the normalization of the states and the creation/destruction operators. There is a quark number operator $b^\dagger b$ for flavor j. We integrate over the quark transverse momentum $\vec{k}_T$ and sum over the quark spin s.

Introducing quark field operators that can be expanded in terms of creation/destruction operators [7] and extensive algebraic manipulations translate this to coordinate space as

$$f_{j/A}^{(0)}(x) = \frac{1}{4\pi} \int dy^- e^{-ixP^+y^-}\ \langle P^+, \vec{0}_T | \bar{\psi}_{0,j}(0, y^-, \vec{0}_T) \gamma^+ \psi_{0,j}(0, 0, \vec{0}_T) | P^+, \vec{0}_T \rangle \ , \qquad (2.8)$$

where γ^+ is as defined in Appendix A and $\psi_{0,j}$ is the quark field operator. Notice that the (still unrenormalized) quark distribution function is an expectation value in the hadron state of a certain operator. The operator is not local but "bilocal." The two points, $(0, y^-, \vec{0}_T)$ and $(0, 0, \vec{0}_T)$, at which the field operators are evaluated are light-like separated. The formula directs us to integrate over y^- with the right factor so that we annihilate a quark with plus momentum xP^+.

2.3.3 Gauge invariance

As mentioned above, the definition as it stands in Eq. (2.8) relies on the gluon field $A^\mu(x)$ being in the gauge $A^+ = 0$. The formula is modified so that gauge invariance is restored. The gauge invariant definition is

$$f_{j/A}^{(0)}(x) = \frac{1}{4\pi} \int dy^- e^{-ixP^+y^-}\ \langle P^+, \vec{0}_T | \bar{\psi}_{0,j}(0, y^-, \vec{0}_T) \gamma^+ \mathcal{O}_0\ \psi_{0,j}(0, 0, \vec{0}_T) | P^+, \vec{0}_T \rangle \ , \qquad (2.9)$$

where

$$\mathcal{O}_0 = \mathcal{P} \exp\left(ig_0 \int_0^{y^-} dz^- \, A^+_{0,a}(0, z^-, \vec{0}_T)\, t_a \right) . \tag{2.10}$$

Here $\mathcal{P}$ denotes a "path-ordered" product, while the t_a are the generators for the triplet representation of SU(3). There is an implied sum over the color index a. Eq. (2.10) is referred to as the eikonal gauge operator. The gauge invariance of this generalization is proven in [3].

2.3.4 Interpretation of the eikonal gauge operator

The appearance of the operator $\mathcal{O}_0$, Eq. (2.10), in the definition (2.9) seems to be just a technicality. However, this operator has a physical interpretation that is of some importance. Let us write this operator in the form

$$\mathcal{O}_0 = \bar{\mathcal{P}} \exp\left(-ig_0 \int_{y^-}^{\infty} dz^- \, A^+_{0,a}(0, z^-, \vec{0}_T)\, t_a \right) \mathcal{P} \exp\left(ig_0 \int_0^{\infty} dz^- \, A^+_{0,a}(0, z^-, \vec{0}_T)\, t_a \right) . \tag{2.11}$$

Inserting this form in the definition (2.9), we can introduce a sum over states $|N\rangle\langle N|$ between the two exponentials in Eq. (2.11). We take these states to represent the final states after the quark has been "measured."

Consider now a deeply inelastic scattering experiment that is used to determine the quark distribution. The experiment does not just annihilate the quark's color. In a suitable coordinate system, a quark moving in the plus direction is struck and exits to infinity with almost the speed of light in the minus direction, as illustrated in Fig. 2.4. As it goes, the struck quark interacts with the gluon field of the hadron.

We can now see that the role of the operator $\mathcal{O}_0$ is to replace the struck quark with a fixed color charge that moves along a light-like line in the minus-direction, mimicking the motion of the actual struck quark in a real experiment.

2.3.5 Renormalization

We now review the renormalization of the operator products in the definition (2.9). The subject of renormalization is vast; here we give a brief treatment only for completeness. Everywhere $\overline{\text{MS}}$ renor-

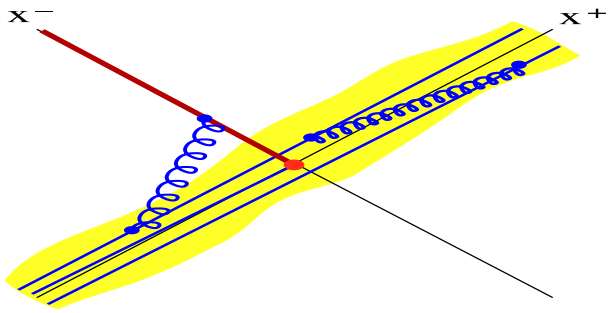


Fig. 2.4: Effect of the eikonal gauge operator.

malized fields $\psi(x)$ and $A^\mu(x)$ and the renormalized coupling g are used. The field operators are evaluated at points separated by Δx with $\Delta x^\mu \Delta x_\mu = 0$ (light-like). For this reason, there will be ultraviolet divergences from the operator products. The operator products are renormalized within the $\overline{\text{MS}}$ scheme.

For instance, Fig. 2.5 illustrates one of the diagrams for the distribution of quarks in a proton. Before it is "measured", the quark emits a gluon into the final state. There is a loop integration over the minus and transverse components of the measured quark's momentum. This loop integration is ultraviolet divergent. To apply $\overline{\text{MS}}$ renormalization, the integration is performed in $4 - 2\epsilon$ dimensions, including a factor $(\mu^2 e^\gamma/4\pi)^\epsilon$ that keeps the dimension constant while supplying some conventional factors. The integral will consist of a pole term proportional to $1/\epsilon$ plus terms that are finite as $\epsilon \to 0$. We simply subtract the pole term. Notice that $\overline{\text{MS}}$ renormalization introduces a scale μ.

The formal definition of the renormalized quark distribution function can then be written based on Eq. (2.8) as

$$f_{j/A}(x,\mu) = \frac{1}{4\pi}\int dy^- e^{-ixP^+y^-}\ \langle P^+, \vec{0}_T|\bar{\psi}_j(0,y^-,\vec{0}_T)\gamma^+\mathcal{O}\ \psi_j(0,0,\vec{0}_T)|P^+,\vec{0}_T\rangle_{\overline{\text{MS}}}\ , \quad (2.12)$$

where the $\overline{\text{MS}}$ denotes the renormalization prescription and where

$$\mathcal{O} = \mathcal{P}\exp\left(ig\int_0^{y^-} dz^-\ A_a^+(0,z^-,\vec{0}_T)\,t_a\right)\ . \quad (2.13)$$

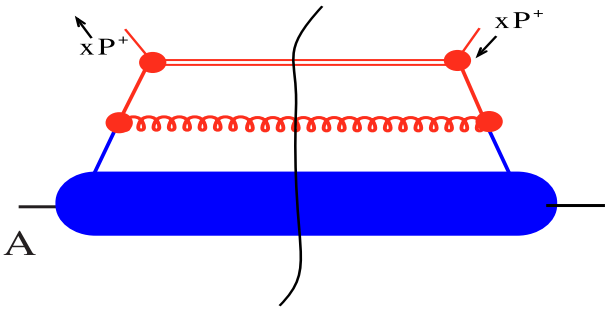


Fig. 2.5: An ultraviolet divergent diagram when integration over components of the quark momentum is carried out.

2.3.6 Antiquarks and gluons

We now have a definition of parton distribution functions for quarks. For antiquarks, we use charge conjugation to define

$$f_{\bar{j}/A}(x,\mu) = \frac{1}{4\pi}\int dy^- e^{-ixP^+y^-}\ \langle P^+,\vec{0}_T|\mathrm{Tr}\Big\{\gamma^+\psi_j(0,y^-,\vec{0}_T)\mathcal{O}\,\bar{\psi}_j(0,0,\vec{0}_T)\Big\}|P^+,\vec{0}_T\rangle_{\overline{\mathrm{MS}}}$$

Here

$$\mathcal{O} = \mathcal{P}\exp\left(-ig\int_0^{y^-} dz^-\ A_a^+(0,z^-,\vec{0}_T)\,t_a^T\right)\ . \tag{2.14}$$

For gluons the procedure again begins with the number operator in $A^+ = 0$ gauge. Proceeding analogously to the quark case, an expression involving the field strength tensor $F_a^{\mu\nu}$ with color index a is obtained:

$$f_{g/A}(x,\mu) = \frac{1}{2\pi\, xP^+}\int dy^- e^{-ixP^+y^-}\ \langle P^+,\vec{0}_T|F_a(0,y^-,\vec{0}_T)^{+\nu}\mathcal{O}_{ab}\ F_b(0,0,\vec{0}_T)_\nu{}^+|P^+,\vec{0}_T\rangle_{\overline{\mathrm{MS}}}$$

Here

$$\mathcal{O} = \mathcal{P}\exp\left(ig\int_0^{y^-} dz^-\ A_c^+(0,z^-,\vec{0}_T)\,t_c\right)\ , \tag{2.15}$$

and the t_c generate the octet representation of SU(3).

2.4 Renormalization group

A change in the scale μ induces a change in the parton distribution functions $f_{a/A}(x,\mu)$. The change comes from the change in the amount of ultraviolet divergence that renormalization is removing. Since the operators are non-local in y^-, the ultraviolet counterterms are integral operators in k^+ or equivalently in momentum fraction x. Since the ultraviolet divergences mix quarks and gluons, so do the counterterms.

An extensive effort in the 1970s by a number of leaders in the field of pQCD led to the equation

$$\mu^2 \frac{d}{d\mu^2} f_{a/A}(x,\mu) = \int_x^1 \frac{d\xi}{\xi} \sum_b P_{ab}(x/\xi, \alpha_s(\mu))\; f_{b/A}(\xi,\mu)\;, \tag{2.16}$$

known as the Dokshitzer-Gribov-Lipatov-Altarelli-Parisi (DGLAP) [8, 9, 10] equation. The DGLAP kernel P_{ab}, the parton splitting function (where a and b are parton types), is expanded in powers of α_s. The α_s^1 and α_s^2 terms are well known. This is how pQCD gives the scale evolution of the nonperturbative parton distributions. Further discussion can be found in Sec.2.5.5.

The derivation of the renormalization group equation (2.16) is rather technical. Its intuitive meaning can be summarized as follows. Parton splitting is always going on as illustrated in Fig. 2.6.

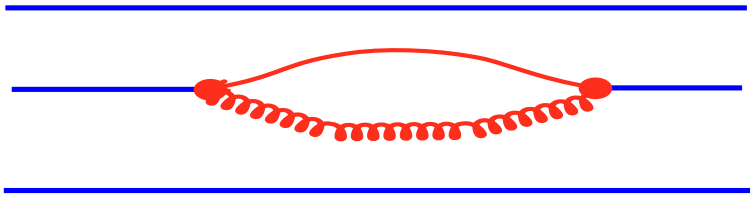


Fig. 2.6: A quark can fluctuate into a quark plus a gluon in a small space-time volume.

A probe with low resolving power does not see this splitting. The renormalization parameter μ corresponds to the physical resolving power of the probe. At higher μ, field operators representing an idealized experiment can resolve the mother parton into its daughters.

One can use the renormalization group equation (2.16) to find the parton distributions at a scale μ if they are known at a lower scale μ_0. Fig. 2.7 shows an example, the gluon distribution at $\mu = 10$

GeV and at $\mu = 100$ GeV (using the CTEQ3M parton distribution set [11, 12]). Notice that with greater resolution, a gluon typically carries a smaller momentum fraction x because of splitting.

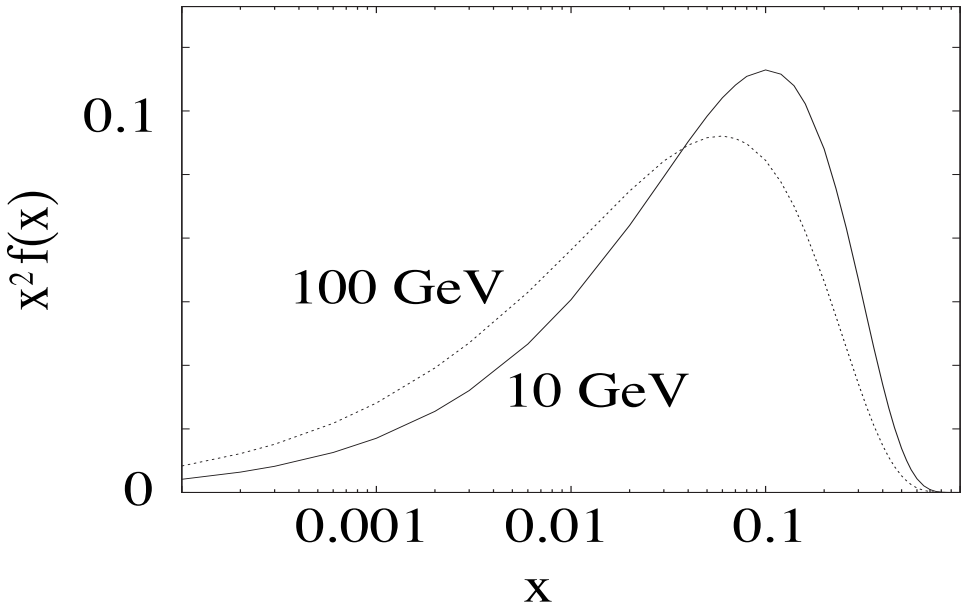


Fig. 2.7: Evolution of the gluon distribution between $\mu = 10\,GeV$ and $\mu = 100\,GeV$.

2.5 Parton distributions of free nucleons

Deep inelastic lepton-nucleon scattering provides the bulk of experimental data needed for the determination of parton distributions in free nucleons. Other important and complementary sources of data are Drell-Yan lepton-pair production, lepton-induced production of heavy quarks, direct photons at large transverse momenta, and neutrino scattering on nucleons. We review in detail deep inelastic lepton-nucleon scattering in this section, while discussion of Drell-Yan and other processes are presented in Chapter 3.

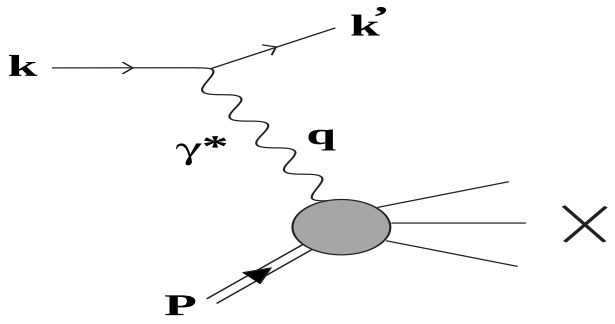


Fig. 2.8: Inclusive deep-inelastic lepton-nucleon scattering. The virtual photon momentum is q. The final hadronic state is not measured, and is denoted by X.

2.5.1 Deep inelastic scattering: kinematics and structure functions

In a typical deep inelastic scattering (DIS) experiment, an incoming beam of leptons with energy E scatters off a hadronic target. The energy and direction of the scattered lepton are measured in the detector, but the final hadronic state (usually denoted by X) is not measured experimentally. The lepton interacts with the hadron target through the exchange of a virtual photon; the target hadron absorbs the virtual photon, to produce the final state X. If the target hadron remains intact, the process is elastic scattering. Deep inelastic scattering corresponds to the case where the target hadron disintegrates into many particles after interacting with the virtual photon.

The basic diagram for deep inelastic scattering is shown schematically in Fig.2.8. Let us consider the scattering of a lepton (an electron or muon) with four-momentum $k^\mu = (E, \vec{k})$ and invariant mass m from a nucleon carrying the four-momentum $P^\mu = (E_{\rm p}, \vec{P})$ and mass M. Inclusive measurements observe only the scattered lepton with momentum $k'^\mu = (E', \vec{k'})$, scattered into the solid angle ω.

To leading order in the electromagnetic coupling constant $\alpha = e^2/4\pi \simeq 1/137$, and neglecting weak interactions which are relevant at very high energies only, the differential cross section is given by:

$$\frac{d^2\sigma}{d\Omega dE'} = \frac{\alpha^2}{Q^4}\frac{E'}{E} L_{\mu\nu} W^{\mu\nu} \ , \tag{2.17}$$

Here

$$q^\mu = k^\mu - k'^\mu = (\nu, \vec{q}) \tag{2.18}$$

is the four-momentum of the exchanged virtual photon, and $Q^2 = -q^2$. The lepton-photon interaction is described by the lepton tensor $L_{\mu\nu}$. Let us denote the spin projections of the initial and final lepton by s and s'. After summing over s' the lepton tensor can be split into pieces which are symmetric and antisymmetric with respect to the Lorentz indices μ and ν:

$$L_{\mu\nu}(k, s; k') = L^S_{\mu\nu}(k; k') + i\, L^A_{\mu\nu}(k, s; k') \,, \tag{2.19}$$

with:

$$L^S_{\mu\nu}(k; k') \;=\; 2\left(k_\mu k'_\nu + k_\nu k'_\mu\right) + g_{\mu\nu}\, q^2 \,, \tag{2.20}$$

$$L^A_{\mu\nu}(k, s; k') \;=\; 2\, m\, \epsilon_{\mu\nu\alpha\beta}\, s^\alpha\, q^\beta \,, \tag{2.21}$$

where the lepton spin vector is defined by $2m\, s^\alpha \;=\; \bar{u}\gamma^\alpha\gamma_5 u$. For unpolarized lepton scattering the average over the initial lepton polarization is carried out. Thus only the symmetric term, $L^S_{\mu\nu}$, remains.

The complete information about the target response is contained in the hadronic tensor $W_{\mu\nu}$. With the nucleon spin denoted by S, gauge invariance and symmetry properties allow a parameterization of the hadronic tensor,

$$W_{\mu\nu}(q; P, S) = W^S_{\mu\nu}(q; P) + i\, W^A_{\mu\nu}(q; P, S) \,, \tag{2.22}$$

in terms of four structure functions, W_1, W_2, G_1, and G_2. The symmetric part is

$$\begin{aligned} W^S_{\mu\nu}(q; P) \;&=\; \left(\frac{q_\mu q_\nu}{q^2} - g_{\mu\nu}\right) W_1(P\cdot q, q^2) \\ &+\; \left(P_\mu - \frac{P\cdot q}{q^2} q_\mu\right)\left(P_\nu - \frac{P\cdot q}{q^2} q_\nu\right) \frac{W_2(P\cdot q, q^2)}{M^2} \,, \end{aligned} \tag{2.23}$$

and the antisymmetric part can be written

$$W^A_{\mu\nu}(q; P, S) \;=\; \epsilon_{\mu\nu\alpha\beta}\, q^\alpha \left[S^\beta M G_1(P\cdot q, q^2) + \left(P\cdot q\, S^\beta - S\cdot q\, P^\beta\right) \frac{G_2(P\cdot q, q^2)}{M}\right] \,, \tag{2.24}$$

where $\epsilon_{\mu\nu\alpha\beta}$ is the totally antisymmetric fourth-rank tensor and M is the mass of the target. The structure functions $W_{1,2}$ can be measured in unpolarized scattering processes, whereas the complete determination of $G_{1,2}$ requires both beam and target to be polarized.

It is convenient to introduce dimensionless structure functions

$$F_1(x, Q^2) = M\, W_1(P \cdot q, q^2)\,, \tag{2.25}$$

$$F_2(x, Q^2) = \frac{P \cdot q}{M}\, W_2(P \cdot q, q^2)\,, \tag{2.26}$$

and

$$g_1(x, Q^2) = MP \cdot q\, G_1(P \cdot q, q^2)\,, \tag{2.27}$$

$$g_2(x, Q^2) = \frac{(P \cdot q)^2}{M}\, G_2(P \cdot q, q^2)\,, \tag{2.28}$$

which depend on the Bjorken scaling variable,

$$x = \frac{Q^2}{2P \cdot q} = \frac{Q^2}{2M\nu}. \tag{2.29}$$

Here, $\nu = E - E' = p \cdot q/M$ is the energy loss of the lepton.

In terms of $F_{1,2}$ the charged lepton scattering cross section (2.17) for an unpolarized lepton and nucleon is:

$$\frac{d^2\sigma}{dx\, dQ^2} = \frac{4\pi\alpha^2}{Q^4}\left[\left(1 - y - \frac{Mxy}{2E}\right)\frac{F_2}{x} + y^2 F_1\right]\,, \tag{2.30}$$

with

$$y = \frac{P \cdot q}{P \cdot k}. \tag{2.31}$$

2.5.2 Bjorken scaling

The variable x was first introduced by Bjorken, and is crucial to understanding deep inelastic scattering. This is because QCD predicts that structure functions are functions of x and do not explicitly depend on Q^2 to leading order, a property known as scaling.

In the Bjorken limit, i.e. at large momentum and energy transfers,

$$Q^2 = -q^2 \to \infty, \quad P \cdot q \to \infty, \tag{2.32}$$

but fixed ratio $Q^2/P\cdot q$, the unpolarized structure functions

$$F_1(x,Q^2) \xrightarrow{Q^2\to\infty} F_1(x)\ , \tag{2.33}$$

$$F_2(x,Q^2) \xrightarrow{Q^2\to\infty} F_2(x) \tag{2.34}$$

are observed to depend to a good approximation only on the dimensionless Bjorken scaling variable x. Variations of the structure functions with Q^2 at fixed x turn out to be small. They are discussed further in Sec.2.5.5.

A similar scaling behavior is expected for the spin-dependent structure functions g_1 and g_2 which likewise reduce to functions of x only when the limit $Q^2\to\infty$ is taken.

2.5.3 Parton model

The approximate Q^2-independence of nucleon structure functions at large Q^2 has led to the conclusion that the virtual photon sees point-like constituents in the nucleon. This is the basis of the naive parton model which gives a simple interpretation of nucleon structure functions. In this picture the nucleon is composed of free pointlike constituents, the partons, identified with quarks and gluons. Introducing parton distributions $q_i(x)$ and $\bar{q}_i(x)$ of quarks and antiquarks with flavor i and fractional electric charge e_i, one finds:

$$F_1(x) = \frac{1}{2}\sum_i e_i^2\left(q_i(x)+\bar{q}_i(x)\right)\ , \tag{2.35}$$

$$F_2(x) = 2x\,F_1(x)\ . \tag{2.36}$$

The Bjorken variable x coincides with the fraction of the target light-cone momentum carried by the interacting quark with momentum l:

$$x=\frac{Q^2}{2P\cdot q}=\frac{l\cdot q}{P\cdot q}\ . \tag{2.37}$$

The Callan-Gross relation (2.36) connecting F_1 and F_2 reflects the spin-$1/2$ nature of the quarks. Corrections to the Callan-Gross relation occur at order α_s.

For the spin structure functions the naive parton model gives:

$$g_1(x) = \frac{1}{2}\sum_i e_i^2 \left[\Delta q_i(x) + \Delta\bar{q}_i(x)\right] , \tag{2.38}$$

$$g_2(x) = 0. \tag{2.39}$$

The structure function g_2 vanishes identically; there is no simple interpretation for g_2 in the parton model. The helicity distributions $\Delta q_i(x) = q_i^{\uparrow}(x) - q_i^{\downarrow}(x)$ and $\Delta\bar{q}_i(x) = \bar{q}_i^{\uparrow}(x) - \bar{q}_i^{\downarrow}(x)$ involve the differences of quark or antiquark distributions with helicities parallel and antiparallel with respect to the helicity of the target nucleon.

2.5.4 Virtual Compton scattering

The hadronic tensor (2.22) can be expressed as the Fourier transform of a correlation function of electromagnetic currents, with its expectation value taken for the nucleon ground state $|P,S\rangle$ normalized as $\langle P',S'|P,S\rangle = 2E_{\rm p}\,(2\pi)^3\,\delta^3(\vec{P}-\vec{P}')\,\delta_{SS'}$

$$W_{\mu\nu}(q;P,S) = \frac{1}{4\pi\,M}\int d^4z\, e^{iq\cdot z}\,\langle P,S|[J_\mu(z),J_\nu(0)]|P,S\rangle\ . \tag{2.40}$$

The forward virtual Compton scattering amplitude [13, 14] is given by:

$$T_{\mu\nu}(q;P,S) = i\int d^4z\, e^{iq\cdot z}\,\langle P,S|\mathcal{T}\left(J_\mu(z)J_\nu(0)\right)|P,S\rangle\ , \tag{2.41}$$

where $\mathcal{T}$ denotes the time-ordered product. The hadronic tensor, Eq.(2.40), is related to the forward virtual Compton scattering amplitude, Eq.(2.41), through the optical theorem:

$$2\pi M\,W_{\mu\nu} = \mathrm{Im}\,T_{\mu\nu}\ . \tag{2.42}$$

Thus, as a consequence, nucleon structure functions can be represented in terms of virtual photon-nucleon helicity amplitudes,

$$\mathcal{A}_{hH,h'H'} = e^2\epsilon_{h'}^{\mu *}T_{\mu\nu}(H,H')\,\epsilon_h^{\nu}\ . \tag{2.43}$$

Here ϵ_h and $\epsilon_{h'}$ are the polarization vectors of the incoming and scattered virtual photon with helicities h and h', respectively. They have values $+1,-1,0$ (abbreviated as $+,-,0$). Helicities of

the initial and final nucleon are denoted by H and H'. Their values are ± 1, symbolically denoted by $\uparrow, \downarrow$. Choosing the z-axis in space to coincide with $\vec{q}/|\vec{q}|$, the direction of the propagating virtual photon, and quantizing the angular momentum of the target and photon along this axis yields the following relations:

$$F_1 = \frac{1}{4\pi e^2} \left(\mathrm{Im}\, \mathcal{A}_{+\downarrow,+\downarrow} + \mathrm{Im}\, \mathcal{A}_{+\uparrow,+\uparrow} \right), \tag{2.44}$$

$$F_2 = \frac{x}{2\pi e^2 \kappa} \left(\mathrm{Im}\, \mathcal{A}_{+\downarrow,+\downarrow} + \mathrm{Im}\, \mathcal{A}_{+\uparrow,+\uparrow} + 2\, \mathrm{Im}\, \mathcal{A}_{0\uparrow,0\uparrow} \right) , \tag{2.45}$$

where $\kappa = 1 + (2Mx/Q)^2$. For the spin-dependent structure functions:

$$g_1 = \frac{1}{4\pi e^2 \kappa} \left(\mathrm{Im}\, \mathcal{A}_{+\downarrow,+\downarrow} - \mathrm{Im}\, \mathcal{A}_{+\uparrow,+\uparrow} + \sqrt{2(\kappa-1)}\, \mathrm{Im}\, \mathcal{A}_{+\downarrow,0\uparrow} \right) , \tag{2.46}$$

$$g_2 = \frac{1}{4\pi e^2 \kappa} \left(\mathrm{Im}\, \mathcal{A}_{+\uparrow,+\uparrow} - \mathrm{Im}\, \mathcal{A}_{+\downarrow,+\downarrow} + \frac{2}{\sqrt{2(\kappa-1)}}\, \mathrm{Im}\, \mathcal{A}_{+\downarrow,0\uparrow} \right) . \tag{2.47}$$

In the scaling limit the structure functions F_1, F_2 and g_1 are determined by helicity conserving amplitudes. It is therefore possible to express them through virtual photon-nucleon cross sections defined as:

$$\sigma_{hH} = \frac{1}{2MK} \mathrm{Im}\, \mathcal{A}_{hH,hH} , \tag{2.48}$$

with the virtual photon flux $K = (2P \cdot q - Q^2)/2M$. For example, the structure function F_2 reads:

$$F_2 = \frac{1-x}{1+(2Mx/Q)^2} \frac{Q^2}{4\pi^2 \alpha} \left(\sigma_L + \sigma_T \right) , \tag{2.49}$$

where the longitudinal and transverse photon-nucleon cross sections $\sigma_{L,T}(\nu, Q^2)$ are given by:

$$\sigma_L = \frac{1}{2} \left(\sigma_{0\uparrow} + \sigma_{0\downarrow} \right), \tag{2.50}$$

$$\sigma_T = \frac{1}{4} \left(\sigma_{+\uparrow} + \sigma_{+\downarrow} + \sigma_{-\uparrow} + \sigma_{-\downarrow} \right) . \tag{2.51}$$

An interesting quantity is their ratio:

$$R = \frac{\sigma_L}{\sigma_T} = \frac{F_2 (1 + (2Mx/Q)^2)}{2xF_1} - 1 . \tag{2.52}$$

In the simple parton model the Callan-Gross relation (2.36) implies $R = 0$ as $Q^2 \to \infty$. Due to their interaction with gluons, quarks receive momentum components transverse to the photon direction. Then they can absorb also longitudinally polarized photons. This leads to $R \neq 0$.

2.5.5 QCD-improved parton model

Nucleon structure functions systematically exhibit a weak Q^2-dependence, even at large Q^2. These scaling violations can be described within the framework of the QCD-improved parton model which incorporates the interaction between quarks and gluons in the nucleon in a perturbative way (see e.g. [13, 14]). The scale at which this interaction is resolved is determined by the momentum transfer. The Q^2-dependence of parton distributions, e.g.

$$F_2(x,Q^2) = \sum_i e_i^2\, x\, \left[q_i(x,Q^2)+\bar{q}_i(x,Q^2)\right] , \tag{2.53}$$

$$g_1(x,Q^2) = \frac{1}{2}\sum_i e_i^2 \left[\Delta q_i(x,Q^2)+\Delta\bar{q}_i(x,Q^2)\right] , \tag{2.54}$$

is described by the Dokshitzer-Gribov-Lipatov-Altarelli-Parisi (DGLAP) evolution equations, introduced in Sec.2.4. These equations are different for flavor non-singlet and singlet distribution functions. Typical examples of non-singlet combinations are the difference of quark and antiquark distribution functions, or the difference of up and down quark distributions. The difference of the proton and neutron structure function, $F_2^{\rm p}-F_2^{\rm n}$, also behaves as a flavor non-singlet, whereas the deuteron structure function $F_2^{\rm d}=F_2^{\rm p}+F_2^{\rm n}$ is an almost pure flavor singlet combination. For the flavor non-singlet quark distribution, $q^{\rm NS}$, and the flavor-singlet quark and gluon distributions, $q^{\rm S}$ and g, the DGLAP evolution equations (in a slightly modified notation compared to Eq. (2.16)) read as follows:

$$\frac{dq^{\rm NS}(x,Q^2)}{d\ln Q^2} = \frac{\alpha_s(Q^2)}{2\pi}\int_x^1 \frac{dy}{y} P_{qq}\left(\frac{x}{y}\right) q^{\rm NS}(y,Q^2) , \tag{2.55}$$

$$\frac{d}{d\ln Q^2}\begin{pmatrix} q^{\rm S}(x,Q^2) \\ g(x,Q^2)\end{pmatrix} = \frac{\alpha_s(Q^2)}{2\pi}\int_x^1 \frac{dy}{y} \begin{pmatrix} P_{qq}(\frac{x}{y}) & P_{qg}(\frac{x}{y}) \\ P_{gq}(\frac{x}{y}) & P_{gg}(\frac{x}{y})\end{pmatrix}\begin{pmatrix} q^{\rm S}(y,Q^2) \\ g(y,Q^2)\end{pmatrix} \tag{2.56}$$

Here $\alpha_s(Q^2)$ is the running QCD coupling strength. The splitting function $P_{qq}(x/y)$ determines the probability for a quark to radiate a gluon such that the quark momentum is reduced by a fraction x/y. Similar interpretations hold for the remaining splitting functions.

2.5.6 Global fits to nucleon parton distributions

Global analysis of parton distributions involves making use of experimental data from many physical processes and using the parton evolution equations to extract a set of universal parton distributions which best fit the existing data. These distributions can then be used in predicting physical observables at energy scales far beyond those presently available, and for other processes. In this sense the distributions are "universal".

A typical procedure for global analysis involves the following necessary steps [4]:

(i) Develop a program to solve the evolution equations numerically (a set of coupled integro-differential equations);

(ii) Make a choice of experimental data sets, such that the data can give the best constraints on parton distributions;

(iii) Select the factorization scheme — the DIS or the $\overline{\rm MS}$ scheme (and make consistent set of choices concerning a factorization scale for all the processes);

(iv) Choose the parametric form for the input parton distributions at μ_0, and then evolve the distribution to any other values of μ_f;

(v) Use the evolved distributions to calculate χ^2 between theory and data, and choose an algorithm to minimize the χ^2 by adjusting the parameterizations of the input distributions;

(vi) Parameterize the final parton distributions at discrete values of x and μ_f by some analytic functions.

In all high-energy data, deeply inelastic scattering of leptons on nucleons and nuclear targets remains the primary source of information on parton distributions, because of its high statistics. Such data are known to be mostly sensitive to certain combinations of quark distributions. Drell-Yan lepton pair production and direct photons at large transverse momenta provide important complimentary information on antiquark and gluon distributions. Most data used in obtaining parton distributions are at fixed-target energies, although the most recent fits incorporate data from colliders.

Several groups have performed "global fitting" of parton distributions, and in most cases several versions and updates are available. We will focus our attention to the MRST, CTEQ, and GRV fits:

• Martin, Roberts, Stirling and Thorne (MRST) [15],

• Botts, Huston, Lai, Morfin, Owens, Qiu, Tung, Weerts,... (CTEQ) [11].

• Gluck, Reya, and Vogt (GRV) [16]

As stated above, the idea of the global fitting is to adjust the parton distribution functions to make theory and experiment agree for a wide range of processes. For example, recent CTEQ fits have used the following processes:

$e + p \to X$

$\mu + p \to X \qquad \mu + {}^2H \to X$

$\nu + Fe \to X \qquad \bar{\nu} + Fe \to X$

$p + p \to \mu + \bar{\mu} + X \qquad p + {}^2H \to \mu + \bar{\mu} + X$

$p + Cu \to \mu + \bar{\mu} + X$

$p + \bar{p} \to W \to \ell + \bar{\ell} + X$

$p + \bar{p} \to \gamma + X$.

We now illustrate the steps listed above. One chooses a starting scale μ_0 (say 2 GeV). Then one writes the $f_{a/p}(x;\mu_0)$ in terms of several parameters for $a = g, u, \bar{u}, d, \bar{d}, s, \bar{s}$. (Typically the heavy quark distributions, for $a = c, \bar{c}, b, \bar{b}, t, \bar{t}$, are generated from evolution, not fit to data.) For example, since it is known that the distribution has to vanish at $x = 1$, one may choose

$$f(x;\mu_0) = Ax^B(1-x)^C \,. \tag{2.57}$$

where x^B dominates the small-x feature and $(1-x)^C$ determines the large-x behavior. Better fits are achieved using a more general form:

$$f(x;\mu_0) = Ax^B(1-x)^C(1+Ex^D) \,. \tag{2.58}$$

The parton distribution functions obey certain flavor and momentum sum rules, such as

$$\begin{aligned} \int_0^1 dx \, \left[f_{u/p}(x,\mu) - f_{\bar{u}/p}(x,\mu)\right] &= 2, \\ \sum_a \int_0^1 dx \, x f_{a/p}(x,\mu) &= 1 \,. \end{aligned} \tag{2.59}$$

These sum rules have a simple intuitive meaning, and formally follow from the definitions (2.12), (2.14), (2.15). The parameterizations are chosen so that the flavor and momentum sum rules are obeyed exactly.

Now one picks a trial set of parameters. This determines $f(x;\mu_0)$, from which one calculates $f(x;\mu)$ for all μ by evolution. Next, given the $f(x;\mu)$, one generates theory curves for each type of experiment used. Finally, one compares the results to the data.

This sequence is iterated, adjusting the parameters to get a good fit. There are more than 2000 data points and only about 25 parameters to be fit, so the fact that this procedure works at all is an indication that QCD is the correct theory of the strong interactions.

We show an example of parton distributions from a global fit. Fig. 2.9 is a graph of the gluon distribution and the up-quark distribution in a proton, according to a parton distribution set designated CTEQ3M [11]. The figure shows $x^2 f_{a/A}(x,\mu)$ for $a = g$ and $a = u$, $A = p$ at $\mu = 20$ GeV. Note that

$$\int_0^1 dx\; x\, f_{a/A}(x,\mu) = \int d\log x\; x^2 f_{a/A}(x,\mu)\;, \tag{2.60}$$

so the area under the curve is the momentum fraction carried by partons of species a.

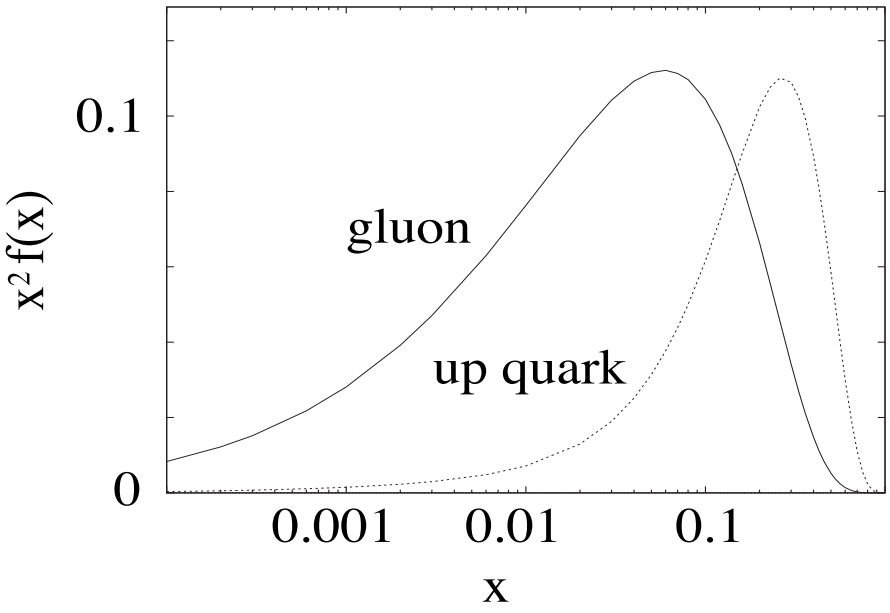


Fig. 2.9: Gluon and up quark distributions in the proton according to the CTEQ3M parton distribution set at $\mu = 20$ GeV.

CHAPTER 3

NUCLEAR MODIFICATIONS

3.1 Introduction

We now consider parton distributions in the nucleus, as opposed to distributions in free nucleons. The nuclear ratio, defined below, serves as a measure of nuclear modifications to parton distributions of free nucleons. In this chapter we briefly review the different facets of these modifications and their experimental manifestations. Most of the material in this review follows [2] and [17], where further details can be found.

3.2 Nuclear DIS and modifications of parton distributions

Nuclei represent systems with a natural, built-in length scale. The baryon density in the center of a typical heavy nucleus is $\rho_0 \simeq 0.15$ fm^{-3}. The average distance between two nucleons at this density is

$$d \simeq 1.9\,\mathrm{fm}. \tag{3.1}$$

The nucleons have a momentum distribution characterized by their Fermi momentum,

$$p_F = \left(\frac{3\pi^2}{2}\,\rho_0\right)^{1/3} \simeq 1.3\,\mathrm{fm}^{-1} \simeq 0.26\,\mathrm{GeV}\ . \tag{3.2}$$

A high energy virtual photon which scatters from this system can expect to see two sorts of genuine nuclear effects:

i) Incoherent scattering from A nucleons, but with their structure functions modified in the presence of the nuclear medium. Such modifications are expected to arise, for example, from the mean field that a nucleon experiences in the presence of other nucleons, and from its Fermi motion inside the nucleus;

ii) Coherent scattering processes involving more than one nucleon at a time. Such effects can occur when hadronic excitations (or fluctuations) produced by the high energy photon propagate over distances (in the laboratory frame) which are comparable to or larger than the characteristic length scale $d \sim 2$ fm of Eq. (3.1). A typical example of a coherence effect is shadowing.

Incoherent scattering takes place primarily in the range $0.1 < x < 1$ of the Bjorken variable. Strong coherence effects are observed at $x < 0.1$. Cooperative phenomena in which several nucleons participate can also occur at $x > 1$. (In fact, the Bjorken variable can extend, in principle, up to $x \leq A$ in a nucleus with A nucleons.)

3.2.1 Nuclear structure functions

The deep-inelastic scattering cross sections for free nucleons and nuclei have basically the same form as given by Eq. (2.17). All information about the target and its response to the interaction is included in the corresponding hadronic tensor. For nuclei with spin $1/2$ the hadronic tensor formally coincides with the one for free nucleons given in Eqs. (2.22,2.23,2.24). In this case nuclei are characterized by four structure functions, $F_{1,2}^{\mathrm{A}}$ and $g_{1,2}^{\mathrm{A}}$. For spin-0 targets, only the symmetric tensor (2.23) with the structure functions $F_{1,2}^{\mathrm{A}}$ is present. In the case of spin-1 targets the hadronic tensor is composed of eight independent structure functions [2]. For spin-$1/2$ nuclei the relations between nuclear structure functions and photon-nucleus helicity amplitudes $\mathcal{A}_{hH,h'H'}^{\gamma^* \mathrm{A}}$ are analogous to the ones for free nucleons in Eqs. (2.44–2.47). For spin-1 targets, see e.g. [18]

Nuclear structure functions depend on the Bjorken scaling variable of the target, $x_{\mathrm{A}} = Q^2/(2P \cdot q)$ with $0 \leq x_{\mathrm{A}} \leq 1$, and on the momentum transfer Q^2. It should be noted, however, that these functions are frequently expressed in terms of the Bjorken variable of the free nucleon which is $x = Q^2/(2M\nu) = x_{\mathrm{A}} M_{\mathrm{A}}/M$ in the lab frame, and which can extend over the interval $0 \leq x \leq M_{\mathrm{A}}/M \simeq A$.

Experiments on deep-inelastic scattering from nuclei are reviewed in [19, 20]. For a discussion of the data it is convenient to use structure functions which depend on the Bjorken scaling variable

for a free nucleon, $x = Q^2/(2M\nu)$. In charged lepton scattering from unpolarized nuclear targets these structure functions are defined by the differential cross section per nucleon:

$$\frac{d^2\sigma^{\rm A}}{dx\,dQ^2} = \frac{4\pi\alpha^2}{Q^4}\left[\left(1 - y - \frac{Mxy}{2E}\right)\frac{F_2^{\rm A}(x,Q^2)}{x} + y^2 F_1^{\rm A}(x,Q^2)\right] . \tag{3.3}$$

3.2.2 Nuclear Ratio

The nuclear ratio is defined as the nuclear structure function per nucleon divided by the nucleon structure function,

$$R_{F_2}^A(x,Q^2) = \frac{F_2^A(x,Q^2)}{A\,F_2^{\rm nucleon}(x,Q^2)} . \tag{3.4}$$

Here A is the nuclear mass number (number of nucleons in the nucleus)[1]. The nucleon structure function is usually defined through measurements on deuterium, $F_2^{\rm nucleon} = F_2^{\rm deuterium}/2$, assuming nuclear effects in deuterium to be negligible.

The behavior of $R_{F_2}^A(x,Q^2)$ as a function of x for a given fixed Q^2 is shown schematically in Fig. 3.1. It can be divided into four regions:

- $R_{F_2}^A < 1$ for $x \lesssim 0.1$: the shadowing region.
- $R_{F_2}^A > 1$ for $0.1 \lesssim x \lesssim 0.25 \sim 0.3$: the antishadowing region.
- $R_{F_2}^A < 1$ for $0.25 \sim 0.3 \lesssim x \lesssim 0.8$: the EMC region (EMC: European Muon Collaboration).
- $R_{F_2}^A > 1$ for $x \gtrsim 0.8$: the Fermi motion region.

Note: the deviation of the nuclear F_2-ratios from one in all four regions of x, is sometimes referred to as the EMC effect. At other places in the literature, it is also sometimes referred to as shadowing.We use the notation EMC only for the depletion observed for $0.25 \sim 0.3 \lesssim x \lesssim 0.8$ and reserve the name shadowing solely for the region $x \lesssim 0.1$. We now discuss the phenomenology of each region in more detail.

[1] Sometimes the ratio of nuclear ratios is used e.g. $R(A/B) = R_{F_2}^A/R_{F_2}^B$.

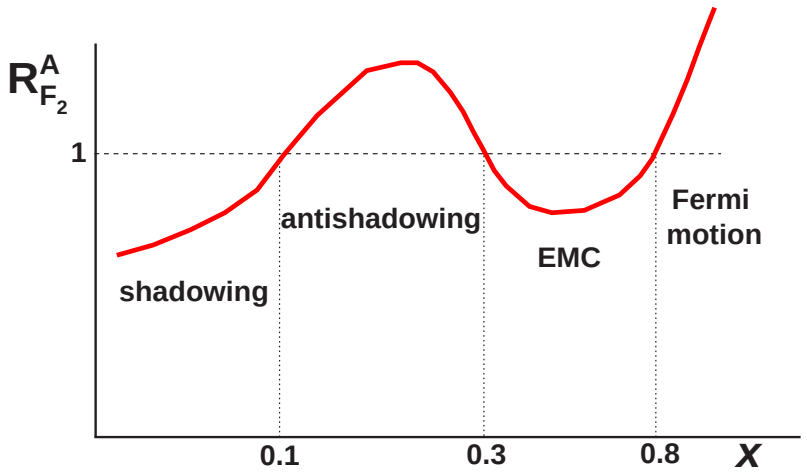


Fig. 3.1: Schematic behavior of $R^A_{F_2}(x, Q^2)$ as a function of x for a given fixed Q^2.

- **Shadowing region**

  Measurements of E665 [21, 22, 23] at Fermilab and NMC [24, 25, 26, 27, 28, 29] at CERN provide detailed and systematic information about the x- and A-dependence of the structure function ratios $F_2^{\rm A}/F_2^{\rm d}$. Nuclear targets ranging from He to Pb have been used. A sample of data for several nuclei is shown in Fig.3.2. While most experiments cover the region $x > 10^{-4}$, the E665 collaboration provides data for $F_2^{\rm Xe}/F_2^{\rm d}$ [21] down to $x \simeq 2{\cdot}10^{-5}$. Given the kinematic constraints in fixed target experiments, the small x-region has been explored at low Q^2 only. For example, at $x \simeq 5 \cdot 10^{-3}$ the typical momentum transfers are $Q^2 \simeq 1$ GeV^2 [25]. At extremely small values, $x \simeq 6 \cdot 10^{-5}$, one has $Q^2 \simeq 0.03$ GeV^2 [21].

  In the region $5 \cdot 10^{-3} < x < 0.1$ the structure function ratios systematically decrease with decreasing x. At still smaller x one enters the range of small momentum transfers, $Q^2 \simeq 0.5$ GeV^2, approaching the limit of high-energy photon-nucleus interactions with real photons.

  Shadowing systematically increases with the nuclear mass number A. For example, at $x \approx 0.01$ one finds $F_2^{\rm A}/F_2^{\rm C} \sim A^{\alpha-1}$ with $\alpha \approx 0.95$ [28]. A similar behavior has been observed in high-energy photonuclear cross sections where the A-dependence is roughly $\sigma_{\gamma{\rm A}} \approx A^{0.92}\sigma_{\gamma{\rm N}}$

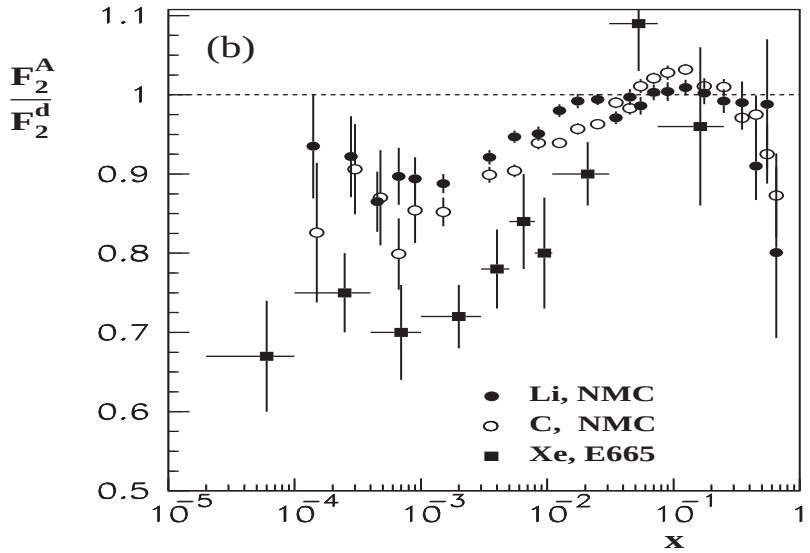


Fig. 3.2: Structure function ratio for some nuclei.

with $\sigma_{\gamma \mathrm{N}}$ the free photon-nucleon cross section averaged over proton and neutron [30].

The shadowing effect depends only weakly on the momentum transfer Q^2. The most precise investigation of this issue has been performed for the ratio of Sn and carbon structure functions. [29]. It reveals that shadowing decreases at most linearly with $\ln Q^2$ for $x < 0.1$. The rate of this decrease becomes smaller with rising x. At $x > 0.1$ no significant Q^2-dependence of $F_2^{\mathrm{Sn}}/F_2^{\mathrm{C}}$ is found.

Shadowing has also been observed in deep-inelastic scattering from deuterium, the lightest and most weakly bound nucleus. At $x < 0.1$ this ratio is systematically smaller than one.

- **Antishadowing region**

  The NMC data have established a small but statistically significant enhancement of the structure function ratio at $0.1 < x < 0.2$. The observed enhancement is of the order of a few percent. For carbon and calcium it amounts to typically 2% [29]. The most precise measurement of this enhancement has been obtained for $F_2^{\mathrm{Sn}}/F_2^{\mathrm{C}}$. Within the accuracy of the data no significant Q^2-dependence of this effect has been found in this region. Note: from normal-

ization considerations the existence of a shadowing region implies that of an antishadowing one, in order for the exact conservation of sum rules.

- **Region of "EMC effect"**

  The region of intermediate $0.2 < x < 0.8$ has been explored extensively at CERN and SLAC. In the range $2\,\mathrm{GeV}^2 < Q^2 < 15$ GeV^2, data were taken by the E139 collaboration [31] for a large sample of nuclear targets between deuterium and gold. The measured structure function ratios decrease with rising x and have a minimum at $x \approx 0.6$. The magnitude of this depletion grows approximately logarithmically with the nuclear mass number. The observed effect agrees well with data for the ratios of iron and nitrogen to deuterium structure functions from BCDMS taken at large Q^2 values, $14\,\mathrm{GeV}^2 < Q^2 < 200$ GeV^2 [32, 33]. These data imply that a strong Q^2-dependence of the structure function ratios is excluded.

- **Fermi motion region**

  At $x > 0.8$ the structure function ratios rise above unity [31], but experimental information is rather scarce. The free nucleon structure function F_2^{N} is known to drop as $(1-x)^3$ when approaching its kinematic limit at $x = 1$. Clearly, even minor nuclear effects appear artificially enhanced in this kinematic range when presented in the form of the ratio $F_2^{\mathrm{A}}/F_2^{\mathrm{N}}$.

- **The region** $x > 1$

  Data at large Bjorken x and large momentum transfer, $0.7 < x < 1.3$ and $50\,\mathrm{GeV}^2 < Q^2 < 200$ GeV^2, have been taken for carbon and iron by the BCDMS [34] and CCFR [35] collaborations, respectively. The results disagree with model calculations at $x \sim 1$ which account for Fermi motion effects only. For $Q^2 < 10$ GeV^2 data have been taken at SLAC for various nuclei. Both quasielastic scattering from nucleons as well as inelastic scattering turns out to be important here.

3.2.3 Other measurements of nuclear parton distributions

Nuclear deep-inelastic scattering is sensitive only to the sum of valence[2] and sea quark distributions (see e.g. Eq. (2.53)), weighted by their respective electric charges. In order to separate nuclear effects in the valence and sea quark sectors, and directly measure nuclear gluon distributions, other types of processes are required which we briefly summarize in the following.

3.2.3.1 Drell-Yan lepton pair production

In the Drell-Yan production of lepton pairs (mostly $\mu^+\mu^-$) in hadron-nucleus collisions, the underlying partonic sub-process is the annihilation of a quark and antiquark from beam and target into a time-like high energy photon, which subsequently converts into the observed dilepton. The Drell-Yan cross section reads (see e.g. [4]):

$$\frac{d^2\sigma}{dx_T dx_B} = \frac{4\pi\alpha^2}{9\,m_l^2}\,K\,\sum_i e_i^2\,\left[q_i^B(x_B,Q^2)\,\bar{q}_i^T(x_T,Q^2) + \bar{q}_i^B(x_B,Q^2)\,q_i^T(x_T,Q^2)\right]\,, \qquad (3.5)$$

where m_l is the invariant mass of the produced lepton pair. The flavor dependent quark distributions of the projectile and target are denoted by q_i^B and q_i^T, respectively. Seen from the center-of-mass frame the active quarks carry fractions x_B and x_T of the beam and target momenta. They are determined by the momentum component q_L of the produced dilepton parallel to the beam, its invariant mass m_l and the squared center-of-mass energy s:

$$x_T\,x_B = \frac{m_l^2}{s}, \quad x_F = \frac{2q_L}{\sqrt{s}} = x_B - x_T. \qquad (3.6)$$

Higher order QCD corrections to the production cross section (3.5) turn out to be significant. They are absorbed in the so-called "K-factor" and effectively double the leading order cross section.

The E772 experiment at FNAL [36] has investigated Drell-Yan dilepton production in proton-nucleus collisions at $s = 1600$ GeV^2. At $x_F > 0.2$ the production process is dominated by the annihilation of projectile quarks with target antiquarks. Outside the domain of quarkonium resonances, i.e. for $4\,\mathrm{GeV} < m_l < 9$ GeV and $m_l > 11$ GeV, this experiment explores possible mod-

[2] Valence quarks are distinguished from sea quarks based on the symmetry classifications of the simple quark model, according to which mesons are (valence) $q\bar{q}$ states, baryons appear as qqq bound states.

ifications of nuclear sea quark distributions. At $x_T > 0.1$ no significant nuclear effects have been observed within admittedly large experimental errors. This indicates the absence of strong modifications of nuclear sea quark distributions, as compared to those of free nucleons. At $x_T < 0.1$, on the other hand, the observed attenuation for heavy nuclei implies a substantial reduction of nuclear sea quarks, in qualitative agreement with the shadowing effects observed in nuclear deep-inelastic scattering at $x < 0.1$. The detailed comparison of shadowing in Drell-Yan versus DIS requires, of course, a careful separation of valence and sea quark effects as well as their Q^2 evolution [37].

3.2.3.2 Lepton-induced production of heavy quarks

The intrinsic heavy-quark (c- or b-quark) distributions in nucleons or nuclei are expected to be very small. Inelastic heavy-quark production is therefore assumed to receive its major contributions from photon-gluon fusion, i.e. the coupling of the exchanged virtual photon to a heavy quark pair which is attached to a gluon out of the target. This mechanism is a basic ingredient of the so-called color-singlet model [38].

In this model the cross section for heavy quark pair production is proportional to the gluon distribution of the target. A comparison of these cross sections for nucleons and nuclei can then be directly translated into a difference of the corresponding gluon distributions.

In this context NMC has analyzed J/ψ production data from Sn and carbon nuclei [39]. The average ratio of the corresponding inelastic J/ψ production cross sections was found slightly larger than one:

$$\frac{\sigma(\gamma^* + \mathrm{Sn} \to J/\psi + \mathrm{X})}{\sigma(\gamma^* + \mathrm{C} \to J/\psi + \mathrm{X})} = 1.13 \pm 0.08 \; . \tag{3.7}$$

Within the color singlet model this implies an enhancement by about 10% of the gluon distribution in Sn as compared to carbon in the region $x \sim 0.1$, though with large errors.

3.2.3.3 Neutrino scattering from nuclei

Deep-inelastic neutrino scattering, involving both charged and neutral currents, permits one to separate valence and sea quark distributions. It is therefore a promising tool to investigate modifications

of the different components of quark distributions in nuclei. The observed nuclear effects in neutrino experiments are qualitatively similar to the results from charged lepton scattering, although their statistical significance is poor, given the large experimental uncertainties.

3.2.4 Global fits to nuclear parton distributions

Global fits do not try to address the origin of nuclear shadowing (or of modifications of parton densities in nuclei in general) but to study the Q^2-evolution of nuclear ratios of parton densities,

$$R_i^A(x,Q^2) = \frac{f_i^A(x,Q^2)}{A\, f_i^{\rm nucleon}(x,Q^2)}\,, \quad f_i = q, \bar{q}, g, \tag{3.8}$$

through the DGLAP evolution equations [8, 9, 10]. From the very first attempts [40], several analyses have appeared [41, 42, 43, 44, 45, 46, 47, 48]. They try to perform for the nuclear case the same program developed for the nucleon: nuclear ratios are parameterized at some value $Q_0^2 \sim 2$ GeV^2 which is assumed large enough for perturbative DGLAP evolution to be applied reliably. These initial parameterizations for every parton density have to cover the full x range $0 < x < 1$. In the nuclear case, the nuclear size appears as an additional variable. Then these initial conditions are evolved through the DGLAP equations towards larger values of Q^2 and compared with experimental data. From this comparison the initial parameterizations are adjusted.

Different approaches differ in several details, see [49]:

- The form of the parameterizations at the initial scale. For example, in [43, 45] shadowing saturates for very small x, contrary to [48]. Also the value of Q_0^2 varies e.g. from ~ 0.4 GeV^2 [48] to 2.25 GeV^2 [43, 45]. The parametrizations for sea quarks and gluons in [46] do not show any EMC effect. Special mention has to be made of the approach in [41, 42] where the initial gluon density is taken from diffractive nucleon data at $Q_0^2 = 4$ GeV^2 and no attempt is made to modify it from the comparison with experimental data.

- The use of different sets of experimental data. For example, Drell-Yan data [36] are used in [43, 45, 47, 48] but not in [46]. These data give the main constraint to the valence and sea contributions in the antishadowing region in [43, 45] but the parametrizations in [47] do not

show antishadowing for sea quarks. HERMES data [50] are used in [47]. Also the data on the Q^2-dependence of nuclear ratios [29] are included in [43, 45, 47, 48], but not in [46]; they give the main constraint on the gluon distribution at small and moderate x, see below.

- The order of DGLAP evolution. The evolution is made at leading order (LO) in [43, 45] and at next-to-leading (NLO) order in [46, 47, 48]. This turns out to modify the Q^2-dependence of nuclear ratios.

- The treatment of isospin effects and the use of sum rules as additional constraints for evolution. For example, isospin symmetry of the nuclear ratios is assumed in [43, 45], but not in [46]. Momentum, charge and baryon number conservation are used in [46, 48], but charge conservation is not used in [43, 45]. In practice, these differences are numerically small.

- The different nucleon partons densities used in the analysis. In practice this choice is of little importance at the level of the nuclear ratios, as its effect appears in both the numerator and denominator in (3.8) and cancels to a large extent.

Gluons are almost unconstrained for $x < 0.02$, and sea quarks for $x < 0.005$. The stronger constraint on gluons in the region $0.02 < x < 0.2$ comes from the Q^2-dependence of nuclear ratios.

The DGLAP equations establish a relation between the logarithmic Q^2-evolution of the structure functions and the gluon distribution [51]. Such relation, valid at LO and small x, has been extended to the nuclear ratios [52]:

$$\frac{\partial R^A_{F_2}(x,Q^2)}{\partial \ln Q^2} \approx \frac{10\alpha_s}{27\pi} \frac{xg(2x,Q^2)}{\frac{1}{2}F_2^{\rm deuterium}(x,Q^2)} \left\{ R^A_g(2x,Q^2) - R^A_{F_2}(x,Q^2) \right\} . \tag{3.9}$$

In this way, $R^A_g(2x,Q^2) > R^A_{F_2}(x,Q^2)$ implies a positive Q^2 slope, while $R^A_g(2x,Q^2) < R^A_{F_2}(x,Q^2)$ gives a negative slope. The available data on the Q^2-dependence of nuclear ratios [29] allow to constrain within the DGLAP evolution scheme, the relation between the nuclear gluon distribution and the nuclear ratio for F_2. While in the parameterization [53] the ratio for all flavours is equal at the initial scale Q_0^2, and thus it gives a too small but positive slope, in the parameterization of [54] the shadowing for gluons is much larger than that for sea and valence quarks so it results in a negative slope at the smallest x and Q^2. Therefore, from the comparison with experimental data [29],

DGLAP analysis favors those sets in which gluons are less shadowed than quarks for $x \sim 0.01$. This is at variance with some approaches e.g. [41, 42], where gluons are more shadowed than quarks. The discrepancy between the data and the results of this model when evolved to smaller values of Q^2 from $Q_0^2 = 4$ GeV^2 is considered as evidence of the existence of large power-suppressed contributions.

While DGLAP approaches do not address the fundamental problem of the origin of shadowing, they are of great practical interest. They provide the parton densities required to compute cross sections for observables characterized by a hard scale for which collinear factorization [55] can be applied. Finally, the centrality dependence of shadowing is not addressed in these models as the existing experimental data do not allow its determination, although some approaches e.g. [54, 56] provide an ansatz for such a dependence.

3.2.5 Importance of Shadowing

The importance of the phenomenon of nuclear shadowing is twofold: First, on the theoretical side it offers an experimentally accessible testing ground for our understanding of Quantum Chromodynamics (QCD) in the high-energy regime [57]. Multiple scattering is unavoidable in a quantum field theory as a consequence of such a basic requirement of the theory as unitarity. The nuclear size gives the possibility to control the amount of multiple scattering at given values of momentum fraction x and scale Q. Besides, by varying the scale and the energy of the collision the interplay between the soft non-perturbative and the hard perturbative regimes can be addressed. Second, experimental studies on high-energy nuclear collisions like those at the Relativistic Heavy Ion Collider (RHIC) [58, 59, 60, 61] at the Brookhaven National Laboratory (BNL) are presently carried out. New facilities like the Large Hadron Collider (LHC) [49] at CERN or the Electron-Ion Collider (EIC) [62] under consideration, will become available in the future. They test the behavior of parton densities inside nuclei at larger energies/smaller x than those presently available in fixed target studies like those at the Super Proton Synchrotron (SPS) at CERN. These new experimental data offer the possibility to further constrain our knowledge on the behavior of nuclear cross sections and

structure functions, both for observables characterized by a large scale for which standard perturbation theory can be applied, and for those with intermediate and small scales where new methods have been developed.

CHAPTER 4

NUCLEAR SHADOWING AT SMALL x FROM GRIBOV THEORY

4.1 Introduction

In the region of small x, parton distributions are dominated by sea quarks and gluons. In most approaches, the origin of the depletion of the nuclear ratios in this region is related with the hadronic behavior of the virtual photon [63]. This resolved hadronic component of the photon wave function at high collision energies — equivalent to small values of x, — and at relatively low values of Q^2, will interact several times with the different nucleons in the nucleus, i.e. will experience multiple scattering. As will be discussed below, this results in a reduction of the corresponding cross sections. The cross section is related to the structure function through the nuclear analog of Eq. (2.49) (at very small x) as

$$F_2^A(x,Q^2) = \frac{Q^2(1-x)}{4\pi^2\alpha}\,\sigma_{\gamma^* A}\ , \tag{4.1}$$

with α the fine structure constant. Thus, the phenomenon of multiple scattering is responsible for the shadowing corrections.

Experimental data on shadowing indicate that:

i) shadowing increases with decreasing x, though at the smallest available values of x the behavior is compatible with either a saturation or a mild decrease [21];

ii) shadowing increases with the mass number of the nucleus [28]; and

iii) shadowing decreases with increasing Q^2 [29].

On the other hand, the existing experimental data do not allow a determination of the dependence of shadowing on the centrality of the collision. The available experimental data on shadowing at small x ($x \simeq 10^{-4}$), from NMC[24, 25] and E665[21, 22] experiments, are all at small Q^2 ($Q^2 < 1$ GeV^2). At such small virtualities the photons can be considered quasi-real, and it is thus a reasonable approximation to regard them as real photons with $Q^2 = 0$ GeV^2. The center-of-mass

energies are also low: $W \simeq 15$ GeV for the NMC and $W \simeq 25$ GeV for the E665 measurements.

The Gribov theory[64, 65], which relates shadowing to diffraction, is an efficient theoretical framework for understanding nuclear shadowing. For deuteron and other sufficiently light nuclei, the relationship involves the interaction of the diffractively produced hadronic excitations with only two nucleons. In the case of heavier nuclei, triple and higher-order scattering may be important and needs to be included in the formalism. This leads to some model dependence. In the Gribov theory shadowing is expressed in terms of the diffractive dissociation cross section. For low masses of the hadronic excitations, the diffractive dissociation cross section is well described by vector meson dominance (VMD), while for higher masses, the triple-Regge model is usually employed. The triple-Regge model involves parameters which are not given by the model. These parameters are usually determined from various experimental data on diffraction and photoproduction.

Since the available experimental data on shadowing at small x are all at very low Q^2 ($Q^2 < 1$ GeV^2), we need diffractive dissociation data at very small Q^2 also as input. Such data are available from both the FNAL experiment [66] ($Q^2 = 0$ GeV^2) at energies $W \simeq 12.8$ GeV and $W \simeq 15.2$ GeV and the experiments at the Hadron-Electron Ring Accelerator (HERA) [67, 68, 69, 70, 71] ($Q^2 < 0.01$ GeV^2) at average energies $W \simeq 187$ GeV and $W \simeq 231$ GeV. In our work, as also in [72] we employ a generalized form of the Gribov theory, incorporating the real part of the diffractive scattering amplitude, to calculate the shadowing ratio at very small Bjorken-x. The results have been published in [73, 74]

4.2 Shadowing Ratio and Generalized Gribov Theory

4.2.1 Nuclear Shadowing Ratio

From the previous chapter we have (see Eq. (3.4))

$$R_{F_2}^A(x, Q^2) = \frac{F_2^A(x, Q^2)}{A\, F_2^{\rm nucleon}(x, Q^2)} \ . \tag{4.2}$$

where $F_2^A(x, Q^2)$ is the nuclear structure function and $F_2^{\rm nucleon}(x, Q^2)$ is that of a free nucleon.

Writing Eq. (4.1) for both the nucleus and the nucleon,

$$F_2^A(x,Q^2) = \frac{Q^2(1-x)}{4\pi^2\alpha}\,\sigma_{\gamma^* A}\ , \tag{4.3}$$

and

$$F_2^{\rm nucleon}(x,Q^2) = \frac{Q^2(1-x)}{4\pi^2\alpha}\,\sigma_{\gamma^* N}\ , \tag{4.4}$$

then

$$R_{F_2}^A(x,Q^2) = \frac{F_2^A(x,Q^2)}{A\,F_2^{\rm nucleon}(x,Q^2)} \ = \ \frac{\sigma_{\gamma^* A}}{A\sigma_{\gamma^* N}}\ . \tag{4.5}$$

Since

$$x = \frac{Q^2}{2M\nu}\ , \tag{4.6}$$

we see that in the real-photon approximation $(Q^2 \to 0),\ x \to 0$ and thus

$$\frac{\sigma_{\gamma^* A}}{A\sigma_{\gamma^* N}} \to \frac{\sigma_{\gamma^A}}{A\sigma_{\gamma^N}}\ , \tag{4.7}$$

the real-photon shadowing ratio.

4.2.2 Gribov Theory

In 1969 V. Gribov [64, 65] proved the following theorem: consider the hadron-deuteron scattering at high energies within the approximation that the radius of the deuteron is much larger than the range of the strong interaction. Then the shadowing correction to the total cross section can be expressed in terms of the differential diffractive hadron-nucleon cross section. This is demonstrated in Fig.4.1: the forward hadron-deuteron rescattering amplitude giving rise to the nuclear shadowing correction contains the hadron-nucleon diffractive amplitude (denoted by the shaded blob) squared.

The hadron-deuteron cross section is separable into a part which accounts for the incoherent scattering from individual nucleons, and a correction (shadowing correction) from the coherent interaction with the two nucleons:

$$\sigma_{hd} = \sigma_{hp} + \sigma_{hn} + \delta\sigma_{hd} \tag{4.8}$$

The shadowing correction turns out to be negative; thus the total hadron-deuteron cross section is less than the sum of the incoherent hadron-nucleon cross sections.

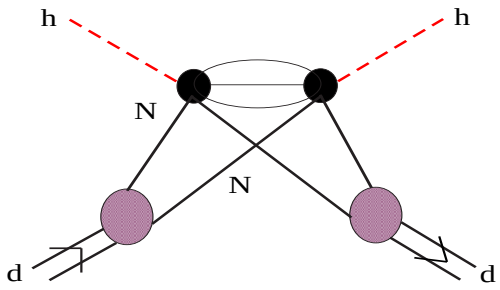


Fig. 4.1: Illustration of Gribov's Theorem: The forward hadron-deuteron rescattering amplitude giving rise to the nuclear shadowing is proportional to the differential hadron-nucleon diffractive cross section at small momentum transfer ($t \sim 0$).

4.2.3 Shadowing Correction From Generalized Gribov Theory

Photon-hadron interactions exhibit characteristics similar to hadron-hadron interactions. This similarity can be exploited to express the photon-deuteron interaction as

$$\sigma_{\gamma^* d} = \sigma_{\gamma^* p} + \sigma_{\gamma^* n} + \delta\sigma_{\gamma^* d} \tag{4.9}$$

in analogy with Gribov's description of hadron-deuteron interaction.

The generalization to photon-nucleus interaction is immediate. The (virtual) photon-nucleus cross section is separable into a part which accounts for the incoherent scattering from individual nucleons, and a correction (shadowing correction) from the coherent interaction with several nucleons:

$$\sigma_{\gamma^* A} = Z\,\sigma_{\gamma^* p} + (A - Z)\,\sigma_{\gamma^* n} + \delta\sigma_{\gamma^* A} \tag{4.10}$$

The single scattering part is the incoherent sum of photon-nucleon cross sections, where Z is the nuclear charge number, and $\sigma_{\gamma^* p}$ and $\sigma_{\gamma^* n}$ are the photon-proton and photon-neutron cross sections, respectively. The multiple scattering correction is expressible as an expansion in the number of nucleons in the target involved in the coherent scattering ($n \geq 2$). Expressed in terms of the

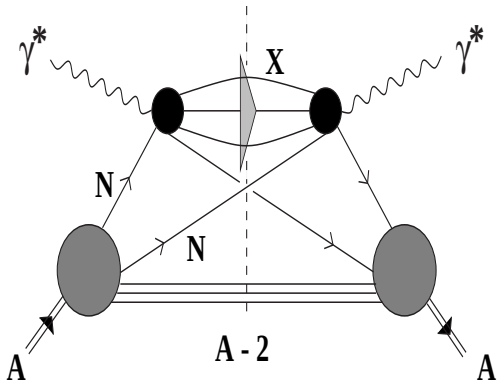


Fig. 4.2: Double scattering contribution to shadowing correction, $\delta\sigma_{\gamma^* A}$

corresponding multiple scattering amplitudes $\mathcal{A}^{(n)}_{\gamma^* \mathrm{A}}$ we have (see Eq. (2.48)):

$$\delta\sigma_{\gamma^* \mathrm{A}} = \frac{1}{2M_{\mathrm{A}}\nu} \sum_{n=2}^{A} \mathrm{Im}\, \mathcal{A}^{(n)}_{\gamma^* \mathrm{A}} \,, \tag{4.11}$$

where the photon flux is taken in the limit $x \ll 1$. The dominant contribution to nuclear shadowing comes from double scattering, since the probability that the propagating hadronic excitation coherently interacts with several nucleons decreases with the number of nucleons.

We generalize the original formulation of Gribov by including the real part of the diffractive scattering amplitude. We denote by η the ratio of the real to imaginary parts of the diffractive scattering amplitude. In this generalized form the shadowing correction at the level of double scattering is given by

$$\delta\sigma_{\gamma^* A} = \frac{A(A-1)}{2A^2}\, 16\pi\, \mathcal{R}e \left[\frac{(1-i\eta)^2}{1+\eta^2} \int d^2b \int_{-\infty}^{\infty} dz_1 \int_{z_1}^{\infty} dz_2 \right.$$
$$\left. \int_{4m_\pi^2}^{W^2} dM_X^2 \left. \frac{d^2\sigma^{\mathrm{diff}}_{\gamma^* N}}{dM_X^2 dt} \right|_{t\approx 0} \rho_A^{(2)}(\vec{b}, z_1; \vec{b}, z_2) \;\; \exp\left\{ i \frac{(z_1 - z_2)}{\lambda} \right\} \right] \tag{4.12}$$

with $\sigma^{\mathrm{diff}}_{\gamma^* N}$ the photon-nucleon diffractive cross section and M_X the mass of the hadronic excitation. The coherence length, λ, is

$$\lambda = \frac{1}{\sqrt{\nu^2 + Q^2} - \sqrt{\nu^2 - M_X^2}} \tag{4.13}$$

The factor $(1-i\eta)^2/(1+\eta^2)$ is a correction for the real part of the diffractive scattering amplitude $\mathcal{T}$. Since the shadowing correction is proportional to $(Im\mathcal{T})^2$, while the total diffractive

cross section is proportional to $|\mathcal{T}|^2$, the factor $(1-i\eta)^2/(1+\eta^2)$ emerges naturally, when nuclear shadowing is expressed in terms of the total diffractive cross section.

As illustrated in Fig. 4.2, a diffractive state with invariant mass M_X is produced in the interaction of the photon with a nucleon located at position $(\vec{b}, z_1)$ in the target. The hadronic excitation is assumed to propagate at fixed impact parameter $\vec{b}$ and to interact with a second nucleon at z_2. The probability to find two nucleons in the target at the same impact parameter is described by the two-body density $\rho_A^{(2)}(\vec{b}, z_1; \vec{b}, z_2)$ normalized as $\int d^3r\, d^3r'\, \rho_A^{(2)}(\vec{r}, \vec{r}\,') = A^2$. The phase factor, $\exp\{i[(z_1 - z_2)/\lambda]\}$ in Eq. (4.12) implies that only diffractively excited hadrons with a longitudinal propagation length larger than the average nucleon-nucleon distance in the target, $\lambda > d \simeq 2\,\mathrm{fm}$, can contribute significantly to double scattering. The limits of integration define the kinematically permitted range of diffractive excitations, with their invariant mass M_X above the two-pion production threshold and limited by the center-of-mass energy $W = \sqrt{s}$ of the scattering process.

We approximate the two-body density $\rho_A^{(2)}(\vec{b}, z_1; \vec{b}, z_2)$ by a product of one-body densities, $\rho_A^{(2)}(\vec{b}, z_1; \vec{b}, z_2) = \rho_A(\vec{r})\rho_A(\vec{r}\,')$, since short-range nucleon-nucleon correlations are relevant in nuclei only when $z_2 - z_1$ is comparable to the range of the short-range repulsive part of the nucleon-nucleon force, i.e. for distances $\lesssim 0.4\,\mathrm{fm}$. However, shadowing is negligible in this case and therefore short-range correlations are not important in the shadowing domain.

With increasing photon energies or decreasing x down to $x \ll 0.1$, the longitudinal propagation length of diffractively excited hadrons rises and eventually reaches nuclear dimensions. Thus, for heavy nuclei, interactions of the excited hadronic state with several nucleons in the target become important and should be accounted for. Following [72] we introduce an attenuation factor with an effective hadron-nucleon cross section, σ_eff. The shadowing correction can thus be written as

$$\delta\sigma_{\gamma^* A} = \frac{A(A-1)}{2A^2}\, 16\pi\, \mathcal{R}e\left[\frac{(1-i\eta)^2}{1+\eta^2}\int d^2b \int_{-\infty}^{\infty} dz_1 \int_{z_1}^{\infty} dz_2 \int_{4m_\pi^2}^{W^2} dM_X^2\, \frac{d^2\sigma^{\mathrm{diff}}_{\gamma^* N}}{dM_X^2 dt}\bigg|_{t\approx 0}\right.$$
$$\left.\rho_A^{(2)}(\vec{b}, z_1; \vec{b}, z_2)\, \exp\left\{i\frac{(z_1 - z_2)}{\lambda}\right\} \exp\left\{-(1/2)(1-i\eta)\sigma_\mathrm{eff}\int_{z_1}^{z_2} dz \rho_A(b,z)\right\}\right]. \quad (4.14)$$

The effective hadron-nucleon cross section, σ_eff in Eq. (4.14) is defined as

$$\sigma_\mathrm{eff} = \frac{16\pi}{\sigma_{\gamma N}(1+\eta^2)} \int_{4m_\pi^2}^{W^2} dM_X^2\, \frac{d^2\sigma^{\mathrm{diff}}_{\gamma^* N}}{dM_X^2 dt}\bigg|_{t\approx 0}, \quad (4.15)$$

where $\sigma_{\gamma N}$ is the photon-nucleon cross section. The details of this approach and the approximations inherent in the definition of σ_{eff} are treated thoroughly in [72]. For vector mesons as the intermediate hadronic excitations, we take σ_{VN} as σ_{eff} in the attenuation factor in Eq. (4.14), where σ_{VN} is the vector meson-nucleon scattering cross section.

4.3 Diffractive Dissociation

4.3.1 Diffractive production

In single diffractive scattering of a (virtual) photon off of a proton (see Fig. 4.3), the proton remains intact and does not dissociate during the process. The photon, on the other hand, dissociates into a hadronic final state X, with a well defined rapidity gap relative to the proton,

$$\gamma^{(*)} + p \to X + p' \,. \tag{4.16}$$

Such diffractive processes are important at small momentum transfer, with cross sections which decrease exponentially with the squared four-momentum transfer. In general they exhibit a weak energy dependence.

Diffractive dissociation of real photons,

$$\gamma + N \to X + N \,, \tag{4.17}$$

has been studied in both fixed target and collider experiments. Experiments were carried out at Fermi National Laboratory (FNAL) at average photon-proton center of mass energies of $W \simeq 12.8$ GeV and $W \simeq 15.2$ GeV[66]. Diffractive states with an invariant mass squared of up to $M_X^2 \simeq 18$ GeV^2 were produced. This experiment measured the differential diffractive dissociation cross section, $\frac{d\sigma^{\text{diff}}_{\gamma N}}{dM_X^2 dt}$, in both the invariant mass M_X and the squared four-momentum transfer t. Experiments at the Hadron-Electron Ring Accelerator (HERA)[67, 68, 69, 70, 71] were carried out at average energies $W \simeq 187$ GeV and $W \simeq 231$ GeV. Diffractive states with mass $M_X < 30$ GeV were produced. Unlike the FNAL experiment, only $d\sigma^{\text{diff}}_{\gamma^* N}/dM_X^2$ was measured due to poor resolution in t.

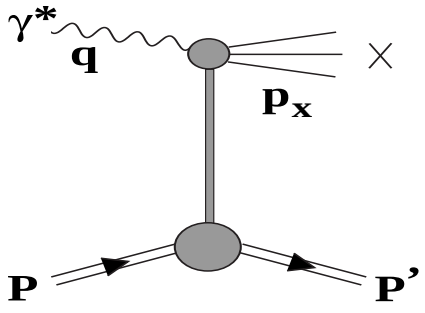


Fig. 4.3: Diffractive scattering from a proton.

4.3.2 Diffractive dissociation cross section

The analysis by the H1 collaboration[69] divides the HERA photoproduction data into effectively three intervals in M_X^2. We adopt this approach in the present study, taking the first interval ($0.16 - 1.58$) GeV^2 to contain the region of the low-mass vector mesons (ρ, ω and ϕ). The second interval ($1.58 - 4.0$ GeV^2) covers the ρ' resonance region. The third interval ($M_X^2 > 4.0$ GeV^2) is that of the high-mass continuum. The differential diffractive cross section is written as a sum over contributions from these three mass intervals,

$$\left.\frac{d\sigma_{\gamma N}^{\rm diff}}{dM_X^2 dt}\right|_{t\approx 0} = \sum_{V=\rho,\omega,\phi} \left.\frac{d\sigma_{\gamma N}^{V}}{dM_X^2 dt}\right|_{t\approx 0} + \sum_{V=\rho'} \left.\frac{d\sigma_{\gamma N}^{V}}{dM_X^2 dt}\right|_{t\approx 0} + \left.\frac{d\sigma_{\gamma N}^{cont}}{dM_X^2 dt}\right|_{t\approx 0} . \tag{4.18}$$

In the following, we briefly summarize the various treatments applied in the three regions.

4.3.2.1 Low-mass vector mesons

We utilize vector meson dominance (VMD) [75] to describe low-mass region of the differential diffractive cross section, i.e. the first term on the right-hand side of Eq. (4.18), yielding [75]:

$$\left.\frac{d\sigma_{\gamma N}^{V}}{dM_X^2 dt}\right|_{t\approx 0} = \frac{\alpha}{4}\Pi^V(M_X^2)\frac{M_X^2}{(Q^2+M_X^2)^2}\sigma_{VN}^2 \tag{4.19}$$

with $\Pi^V(M_X^2)$ the vector meson part of the photon spectral function $\Pi(M_X^2)$,

$$\Pi(M_X^2) = \frac{1}{12\pi^2}\frac{\sigma(e^+e^- \to hadrons)}{\sigma(e^+e^- \to \mu^+\mu^-)} . \tag{4.20}$$

In Eq. (4.19), σ_{VN} is the vector meson-nucleon cross section and $\alpha = e^2/4\pi = 1/137$ is the fine structure constant.

The ω and ϕ mesons are narrow and thus well approximated by delta functions. Their contribution to the photon spectral function can be written as

$$\Pi^V(M_X^2) = \left(\frac{m_V}{g_V}\right)^2 \delta(M_X^2 - m_V^2) \quad ; \quad V = \omega, \phi\,, \tag{4.21}$$

where m_V and g_V, ($V = \omega, \phi$) are the mass and the coupling constant of the ω and ϕ mesons, respectively.

The ρ-meson, unlike the ω and ϕ mesons, has a large width due to its strong coupling to two-pion states. We have followed the approach in [76] and taken this into account through the $\pi^+\pi^-$ part of the photon spectral function:

$$\Pi^\rho\big(M_X^2\big) = \frac{1}{48\pi^2}\Theta\big(M_X^2 - 4m_\pi^2\big)\left(1 - \frac{4m_\pi^2}{M_X^2}\right)^{3/2}\left|F_\pi\left(M_X^2\right)\right|^2\,, \tag{4.22}$$

where m_π is the mass of the pion and $M_X = M_{\pi\pi}$ is the invariant mass of the $\pi^+\pi^-$ pair. The pion form factor, F_π, is taken from Ref. [77]. A full discussion is given in [76]. We compared the result from the delta function approximation to this more exact calculation and found that taking into account the width of the ρ-meson increases the differential diffractive cross section by $\approx 10\%$.

The vector meson-nucleon cross section in Eq. (4.19) has an energy dependence of the form

$$\sigma_{VN} \sim W^{2(\alpha_{I\!P}(0)-1)} = W^{2\epsilon} \tag{4.23}$$

where $\alpha_{I\!P}(t=0) = 1 + \epsilon$, with $\epsilon = 0.08$, is referred to as the soft pomeron intercept [78].

4.3.2.2 Region of the ρ' resonances

The ρ' resonance region contains the $\rho(1450)$ and $\rho(1700)$ mesons. These resonances were formerly classified as the $\rho(1600)$ [79]. The FNAL data show an enhancement in this region. We treat this enhancement in terms of an average ρ' resonance, corresponding to the earlier classification of $\rho(1600)$, as done in Ref. [66]. We use the available information on the $\rho(1600)$ from Ref. [75] in a VMD-type calculation to evaluate the contribution from this region. The average ρ' resonance

should have a finite width, but encouraged by the fact that a delta function in the case of the ρ gives a good approximation to the full-width result, we employ a narrow resonance approximation for the $\rho(1600)$. Thus, for the second term of (4.18) we have

$$\left.\frac{d\sigma^V_{\gamma N}}{dM_X^2 dt}\right|_{t\approx 0} = \frac{\alpha}{4}\Pi^V(M_X^2)\frac{M_X^2}{(Q^2+M_X^2)^2}\sigma^2_{VN} \tag{4.24}$$

with

$$\Pi^V(M_X^2) = \left(\frac{m_V}{g_V}\right)^2 \delta(M_X^2 - m_V^2) \tag{4.25}$$

and $V = \rho(1600)$.

4.3.2.3 High-mass continuum

An appropriate framework in which to model dissociation processes is offered by 'triple-Regge' phenomenology [69]. The details of this approach are summarized in Appendix B.

The differential dissociation cross section including both the pomeron and subleading reggeons can be written as

$$\frac{\mathrm{d}^2\sigma}{\mathrm{d}t\,\mathrm{d}M_X^2} = \left[\frac{G_{\mathbb{P}\mathbb{P}\mathbb{P}}(0)\ s_0^{1-\alpha_{\mathbb{P}}(0)}}{M_X^{2\alpha_{\mathbb{P}}(0)}} + \frac{G_{\mathbb{P}\mathbb{P}\mathbb{R}}(0)\ s_0^{1-\alpha_{\mathbb{R}}(0)}}{M_X^{4\alpha_{\mathbb{P}}(0)-2\alpha_{\mathbb{R}}(0)}}\right]\left(W^2\right)^{2\alpha_{\mathbb{P}}(0)-2}\ e^{B(W^2,M_X^2)\,t}\,, \tag{4.26}$$

where $B(W^2, M_X^2) = 2b_{p\mathbb{P}} + 2\alpha'_{\mathbb{P}}\ln(W^2/M_X^2)$. The notation and meaning of the various symbols in Eq. (4.26) are given in Appendix B.

4.4 Data Analysis and Fits

At very small x NMC has two data points, corresponding to ^{6}Li and ^{12}C. For ^{6}Li, $x = 1.4\times10^{-4}$ and the average Q^2, $\langle Q^2\rangle = 0.034$ GeV^2, thus the virtual-photon energy, $E_{\gamma*} = 129.4$ GeV. This value is comparable to the photon energy from using the NMC cm energy $W = 200$ GeV and energy transferred fraction $\langle y\rangle = 0.64$, $E_{\gamma*} = 128$ GeV. In the case of ^{12}C, $x = 1.5\times10^{-4}$ and the average Q^2, $\langle Q^2\rangle = 0.035$ GeV^2, thus the virtual-photon energy, $E_{\gamma*} = 124.3$ GeV. Using the NMC cm energy $W = 200$ GeV and energy transferred fraction $\langle y\rangle = 0.65$, $E_{\gamma*} = 130$ GeV. Therefore

for both nuclei we use $E_{\gamma *} = 128$ GeV, corresponding to a photon-nucleon center-of-mass energy $W = 15.5$ GeV.

The E665 experiment, at very small x ($x \simeq 10^{-4}$) has four data points: ^{12}C, ^{40}Ca, ^{131}Xe, and ^{208}Pb. The reported photon energy is in the range $50 \leq E_{\gamma}* \leq 300$ GeV, and virtualities $0.1 < Q^2 < 80$ GeV^2. For the smallest x, $\langle Q^2 \rangle = 0.15$ GeV^2. Since for a fixed-target experiment the smallest x corresponds to the smallest Q^2 and largest $E_{\gamma}*$, we use $Q^2 = 0.15$ GeV^2 and $E_{\gamma}* = 300$ GeV in our calculations. Note that these values correspond to $x = 2.66 \times 10^{-4}$, well within the reported small-x values of E665. $E_{\gamma}* = 300$ GeV gives a cm energy $W = 23.75$ GeV.

The free parameters to be determined from experimental data are the triple-pomeron coupling $G_{\mathbb{P}\mathbb{P}\mathbb{P}}(0)$ and the pomeron-pomeron-reggeon coupling $G_{\mathbb{P}\mathbb{P}\mathbb{R}}(0)$. We adopt a simple fitting procedure: the experimental data are fitted to Eq. (4.26) at the average cms energies. These are $W \simeq 12.8$ GeV and $W \simeq 15.2$ GeV for the FNAL experiment, $W \simeq 187$ GeV and $W \simeq 231$ GeV for the HERA experiment. In the following subsections the units of $G_{\mathbb{P}\mathbb{P}\mathbb{P}}(0)$ and $G_{\mathbb{P}\mathbb{P}\mathbb{R}}(0)$ are μb/GeV^2.

4.4.1 FNAL Data

The FNAL data are presented at $t = -0.05$, thus the data are fitted to Eq. (4.26) at this value of t.

The best fit to Eq. (4.26) is given by $G_{\mathbb{P}\mathbb{P}\mathbb{P}}(0) = 12.0 \pm 0.4$ and $G_{\mathbb{P}\mathbb{P}\mathbb{R}}(0) = 1.5 \pm 0.1$ at $W \simeq 12.8$ GeV. For $W \simeq 15.2$ GeV, $G_{\mathbb{P}\mathbb{P}\mathbb{P}}(0) = 9.5 \pm 0.7$ and $G_{\mathbb{P}\mathbb{P}\mathbb{R}}(0) = 2.4 \pm 0.3$ respectively.

The quality of the fits is shown in Fig. 4.4.

4.4.2 HERA Data

The HERA data, unlike the FNAL data, are not presented at a specific value of t. The data have been integrated in t over a kinematic range relevant to the HERA experiment. Thus the first job is to deconvolute the t-integrated data to data at $t = 0$.

As commonly done we assume a t dependence of the form

$$\frac{\mathrm{d}^2\sigma}{\mathrm{d}M_X^2\,\mathrm{d}t} \;=\; \left.\frac{\mathrm{d}^2\sigma}{\mathrm{d}M_X^2\,\mathrm{d}t}\right|_{t=0} e^{B(W^2,M_X^2)\,t}\;, \tag{4.27}$$

and then integrate both sides of Eq. (4.27) over the measured range of t, $|t_{min}| < |t| < 1$ GeV^2. Here $|t_{min}|$ is the minimum kinematically accessible value of t [79]. In the following equations we suppress the W^2 and M_X^2 dependence of B. We can then write

$$\left.\frac{\mathrm{d}^2\sigma}{\mathrm{d}M_X^2\,\mathrm{d}t}\right|_{t=0} = \frac{B}{e^{-B|t_{\min}|} - e^{-B}} \int_{|t_{\min}|}^{1} dt \frac{\mathrm{d}^2\sigma}{\mathrm{d}M_X^2\,\mathrm{d}t} \,. \tag{4.28}$$

Making the identification

$$\int_{|t_{\min}|}^{1} dt \frac{\mathrm{d}^2\sigma}{\mathrm{d}M_X^2\,\mathrm{d}t} \equiv \frac{\mathrm{d}\sigma}{\mathrm{d}M_X^2} \,, \tag{4.29}$$

then

$$\left.\frac{\mathrm{d}^2\sigma}{\mathrm{d}M_X^2\,\mathrm{d}t}\right|_{t=0} = \frac{B}{e^{-B|t_{\min}|} - e^{-B}} \frac{\mathrm{d}\sigma}{\mathrm{d}M_X^2} \,. \tag{4.30}$$

Eq. (4.30) can now be applied to generate a new set of data at $t = 0$ from the HERA t-integrated data.

The fit, based on Eq. (4.26), yields $G_{\mathbb{P}\mathbb{P}\mathbb{P}}(0) = 5.0 \pm 0.8$ and $G_{\mathbb{P}\mathbb{P}\mathbb{R}}(0) = 6.3 \pm 0.8$ at $W \simeq 187$ GeV. For $W \simeq 231$ GeV, $G_{\mathbb{P}\mathbb{P}\mathbb{P}}(0) = 5.3 \pm 0.8$ and $G_{\mathbb{P}\mathbb{P}\mathbb{R}}(0) = 8.5 \pm 0.7$, respectively.

The fits are displayed in Fig. 4.4.

4.4.3 $W \simeq 24$ GeV

There are no experimental data at $W \simeq 24$ GeV, the cms energy relevant to the E665 measurements. Thus we are not able to extract both $G_{\mathbb{P}\mathbb{P}\mathbb{P}}(0)$ and $G_{\mathbb{P}\mathbb{P}\mathbb{R}}(0)$ directly from experiment. We therefore use an indirect method to estimate these parameters: we plot the fit parameters from Sec. 4.4.1 and Sec. 4.4.2 as a function of $W^{2(2\alpha_{\mathbb{P}}(0)-2)}$, the energy functional in Eq. (4.26) at $t = 0$, and then estimate the values at $W = 24$ GeV. We use the energy functional since it occurs explicitly in the extraction of the fit parameters from experimental data. Applying Eq. (4.26), $G_{\mathbb{P}\mathbb{P}\mathbb{P}}(0) = 8.04 \pm 0.79$ and $G_{\mathbb{P}\mathbb{P}\mathbb{R}}(0) = 2.65 \pm 0.32$. This approach, of course, impacts on the accuracy of the determination of the shadowing ratio at this energy due to greater uncertainties associated with the approximate nature of the fit parameters. The fits and corresponding estimates of the fit parameters are displayed in Fig. 4.5. Note that $W^{2(2\alpha_{\mathbb{P}}(0)-2)} = W^{0.272}$ using $\alpha_{\mathbb{P}}(0) = 1.068$.

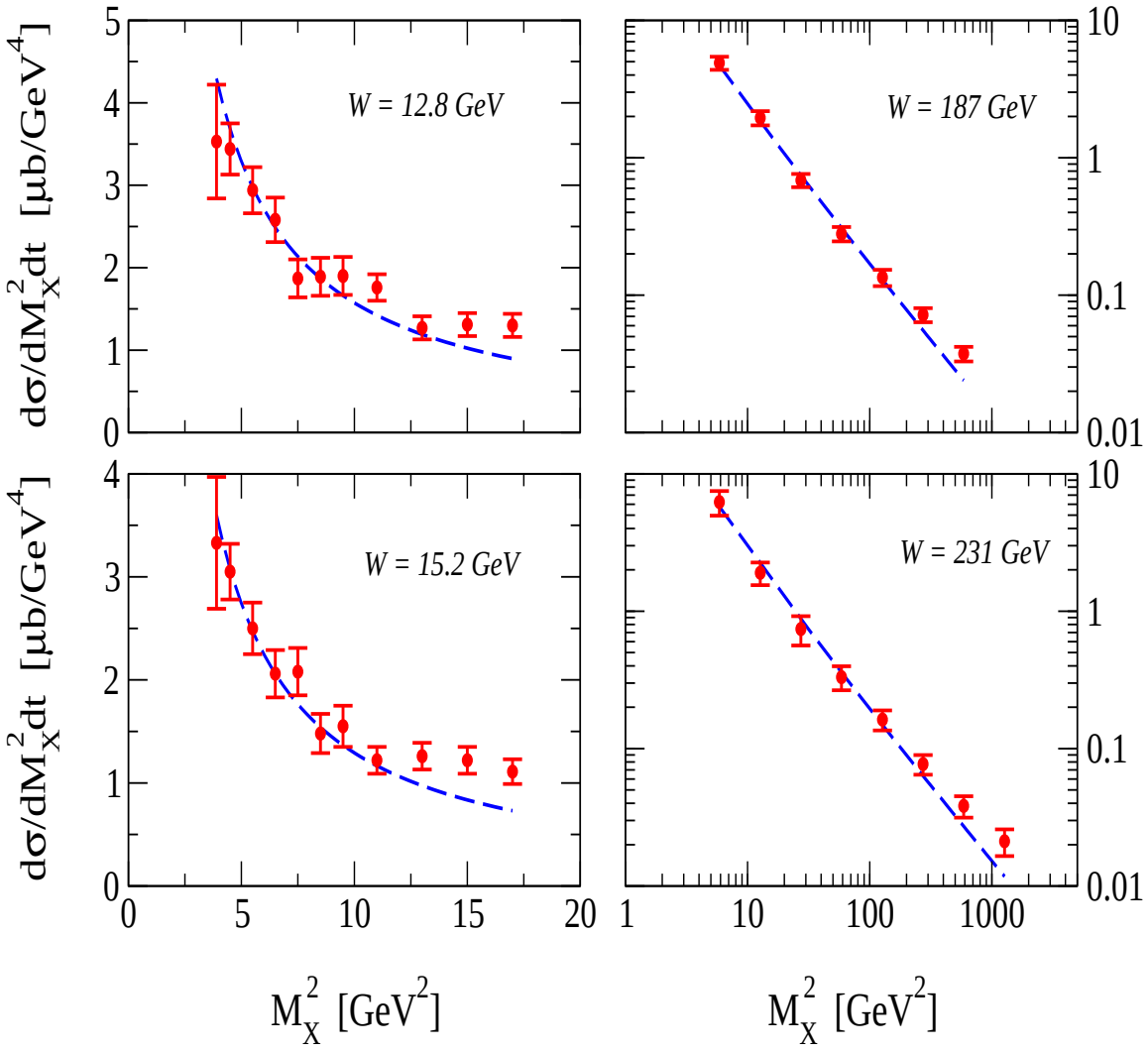


Fig. 4.4: (Color Online) Triple-Regge fit to the FNAL (12.8 GeV and 15.2 GeV) and HERA (187 GeV and 231 GeV) data in the nonresonant continuum ($M_X^2 > 4$ GeV^2). The dashed lines correspond to pomeron+reggeons. The shaded circles are experimental data.

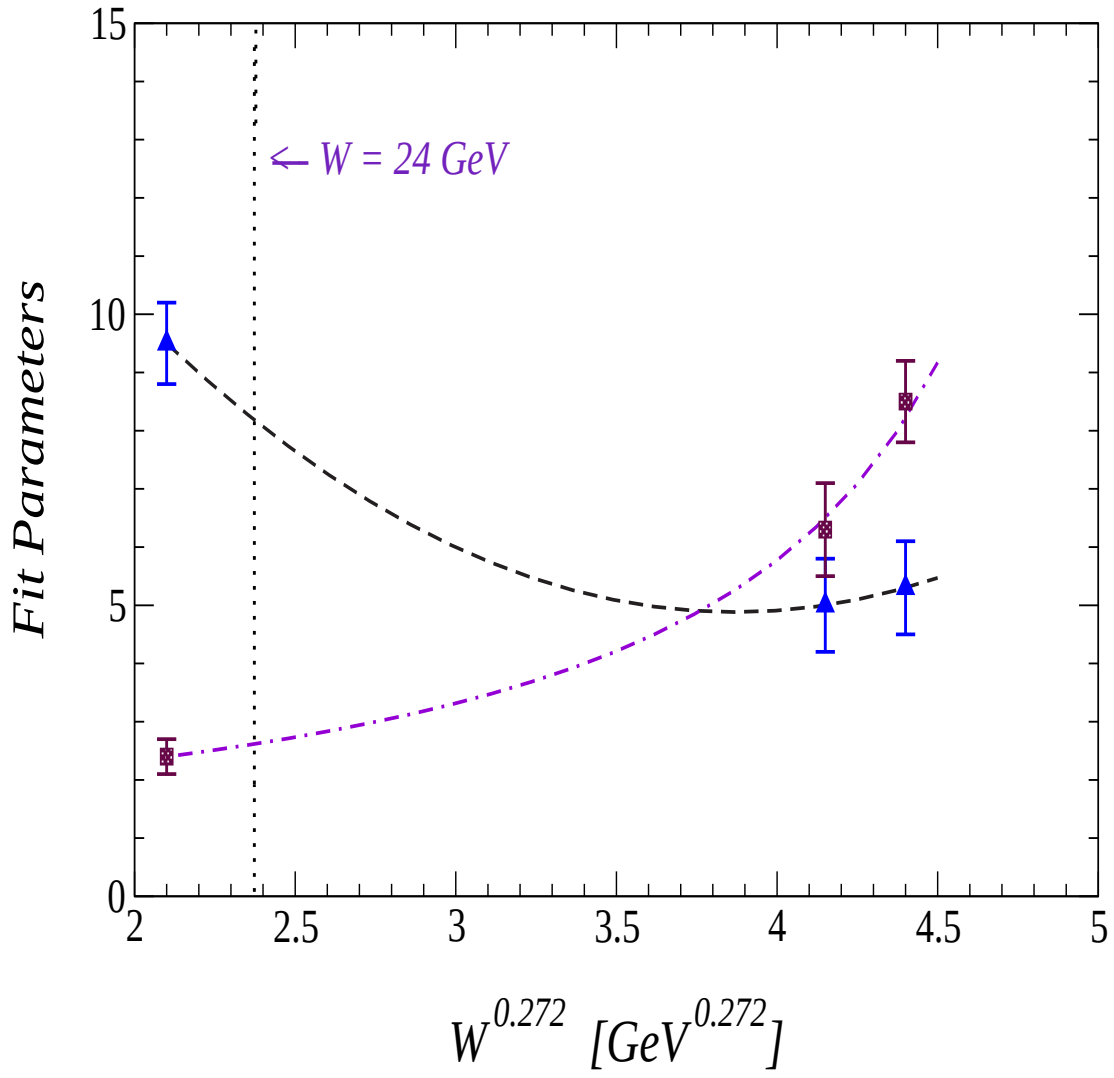


Fig. 4.5: (Color Online) Estimates for the fit parameters at $W = 24$ GeV as discussed in the text. The shaded upright triangles and squares are the $G_{\mathbb{P}\mathbb{P}\mathbb{P}}(0)$ and $G_{\mathbb{P}\mathbb{P}\mathbb{R}}(0)$ from Eq. (4.26) respectively. The dashed and dot-dashed lines are fits to the parameters respectively. The vertical dotted line corresponds to the values of these parameters at $W = 24$ GeV.

4.5 Results: Shadowing Ratio and Mass Dependence

The treatment outlined in the last three sections is now applied to calculate the shadowing correction, and hence the shadowing ratio. The basic equation is Eq. (4.14), which involves the ratio of the real to imaginary amplitudes η, the photon-nucleon cross section $\sigma_{\gamma N}$, the nuclear density $\rho_A(r)$, and the effective cross section $\sigma_{\rm eff}$ in terms of the diffractive dissociation cross section.

We use the energy-independent η's for the vector mesons from Ref. [75]. For both ρ and ω mesons, η takes values between 0 and -0.3. Here we take $\eta_\rho = \eta_\omega = -0.2$ in accordance with Ref. [75]. The results of our calculation are not very sensitive to the precise values of $\eta_{\rho(\omega)}$. For the ϕ meson, we take $\eta_\phi = 0.13$ [80]. For lack of information, we take $\eta_{\rho(1600)} = 0$. For the high-mass continuum, we follow Ref. [72] and define $\eta_{\rm I\!P}$ as

$$\eta_{\rm I\!P} = \frac{\pi}{2}\big(\alpha_{\rm I\!P}(0) - 1\big)\,, \tag{4.31}$$

using the result of Gribov and Migdal [81]. The ratio of the real to imaginary parts of the subleading exchange amplitude $\eta_{\rm I\!R}$ is given by

$$\eta_{\rm I\!R} = -\frac{\xi + \cos(\pi\alpha_{\rm I\!R}(0))}{\sin(\pi\alpha_{\rm I\!R}(0))} \tag{4.32}$$

with $\xi = \pm 1$ the signature factor of the exchanged reggeon. Using the value of $\alpha_{\rm I\!R}(0) = 0.55 \pm 0.10$ from [69], $\eta_{\rm I\!R}(\xi = -1) = 1.17$ and $\eta_{\rm I\!R}(\xi = +1) = -0.854$ respectively. The analysis in [69] assumes a single effective trajectory $\alpha_{\rm I\!R}(t)$ for the four subleading reggeons, thus $-0.854 \leq \eta_{\rm I\!R} \leq 1.17$. Due to the uncertainty in $\alpha_{\rm I\!R}(0)$ and for reasons of symmetry we take the uncertainty range to be $-1 \leq \eta_{\rm I\!R} \leq 1$ as in [72].

The small difference between the photon-proton cross section $\sigma_{\gamma p}$ and the photon-neutron cross section $\sigma_{\gamma n}$ is neglected in this study. We use the Donnachie-Landshoff parameterization of $\sigma_{\gamma p}$ [78] as the generic photon-nucleon cross section $\sigma_{\gamma N}$. For the nuclear densities, three-parameter Fermi ($3pF$) distributions are applied:

$$\rho_A(r) = \rho_0 \frac{1 + \omega(r/R_A)^2}{1 + e^{(r-R_A)/d}}\,, \tag{4.33}$$

with the parameter values taken from Ref. [82]. For mass numbers $A \lesssim 20$ a harmonic oscillator (HO) density distribution may be more appropriate than the $3pF$ distribution. For uniformity, we

use the $3pF$ distributions for the whole mass range in light of the fact that uncertainties associated with other parameters are at least comparable.

4.5.1 Shadowing: NMC

We carried out calculations at 15.5 GeV, the cm energy relevant to the NMC measurements at small x. The results are displayed in Fig. 4.6. At very small x ($x \simeq 10^{-4}$), NMC has two data points, corresponding to ^{6}Li and ^{12}C. In view of the large error bars of the data, the calculations can be said to describe the experimental information adequately well in the applicable mass range. The agreement with data at $A < 12$ can be further improved by using a more realistic density parameterization for that region. The shadowing ratio displays a systematic trend: a rapid decrease at small A and a more gradual one as A increases.

The gap between the $\eta = 1$ and $\eta = -1$ results can be taken as a measure of the uncertainty of the calculated results due to the uncertainty in the determination of $\eta_{\mathbb{IR}}$. This uncertainty is more pronounced for larger mass numbers, but it is reassuring that for the largest mass numbers considered, the gap is small.

4.5.2 Shadowing: E665

At very small x ($x \simeq 10^{-4}$) the E665 experiment has four data points: ^{12}C, ^{40}Ca, ^{131}Xe, and ^{208}Pb. The results of our calculations and the experimental data are shown in Fig. 4.7. The agreement with experimental result is quite good considering the approximations inherent in the determination of the fit parameters at this energy. The statement concerning small A above is also valid here. Also the trend is the same: for small A the shadowing ratio decreases rapidly with A, while for large A the decrease is more gradual.

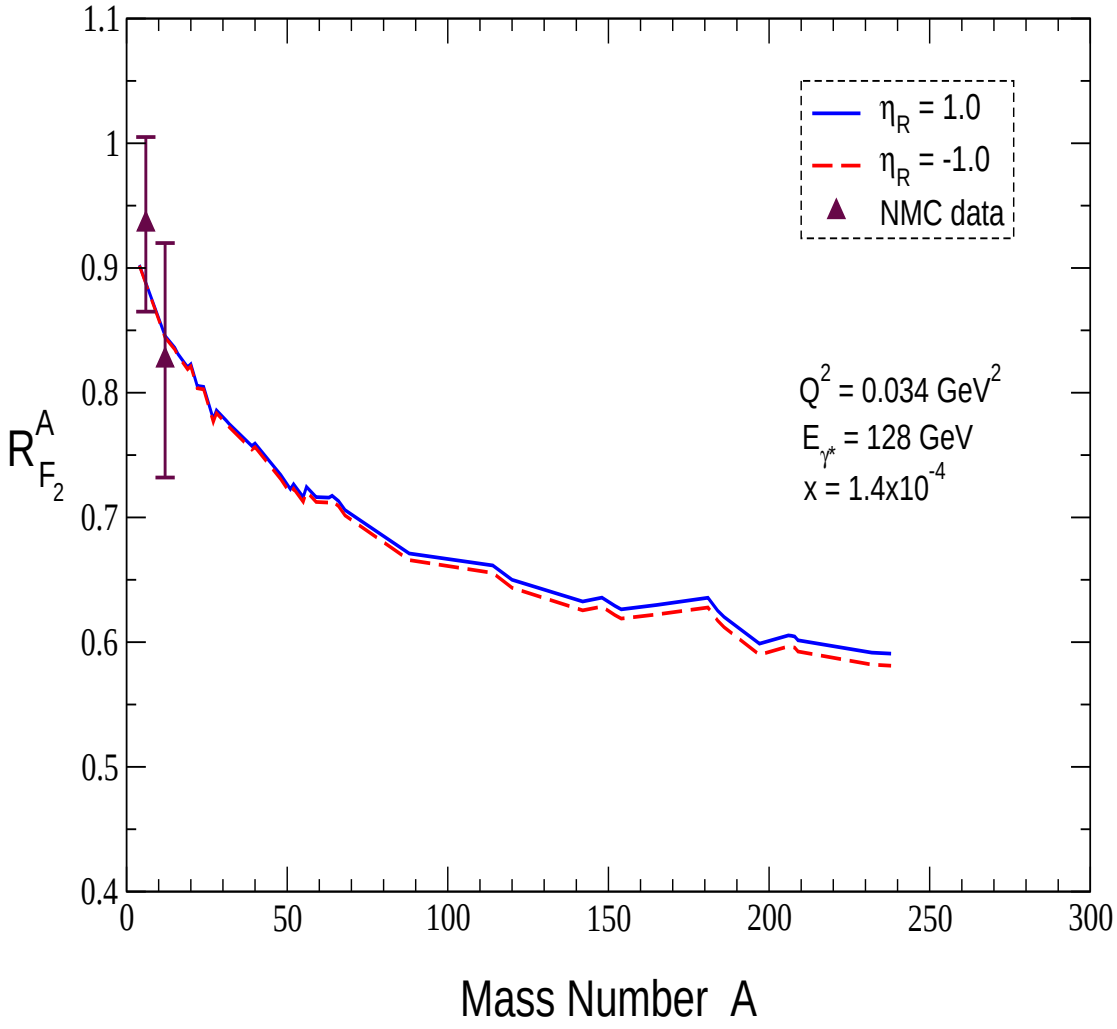


Fig. 4.6: (Color Online) Shadowing ratio at FNAL energies. The thick lines correspond to pomeron+subleading reggeons with $\eta = 1$ while the dashed lines correspond to pomeron+reggeons with $\eta = -1$. The full triangles are data from the NMC experiment.

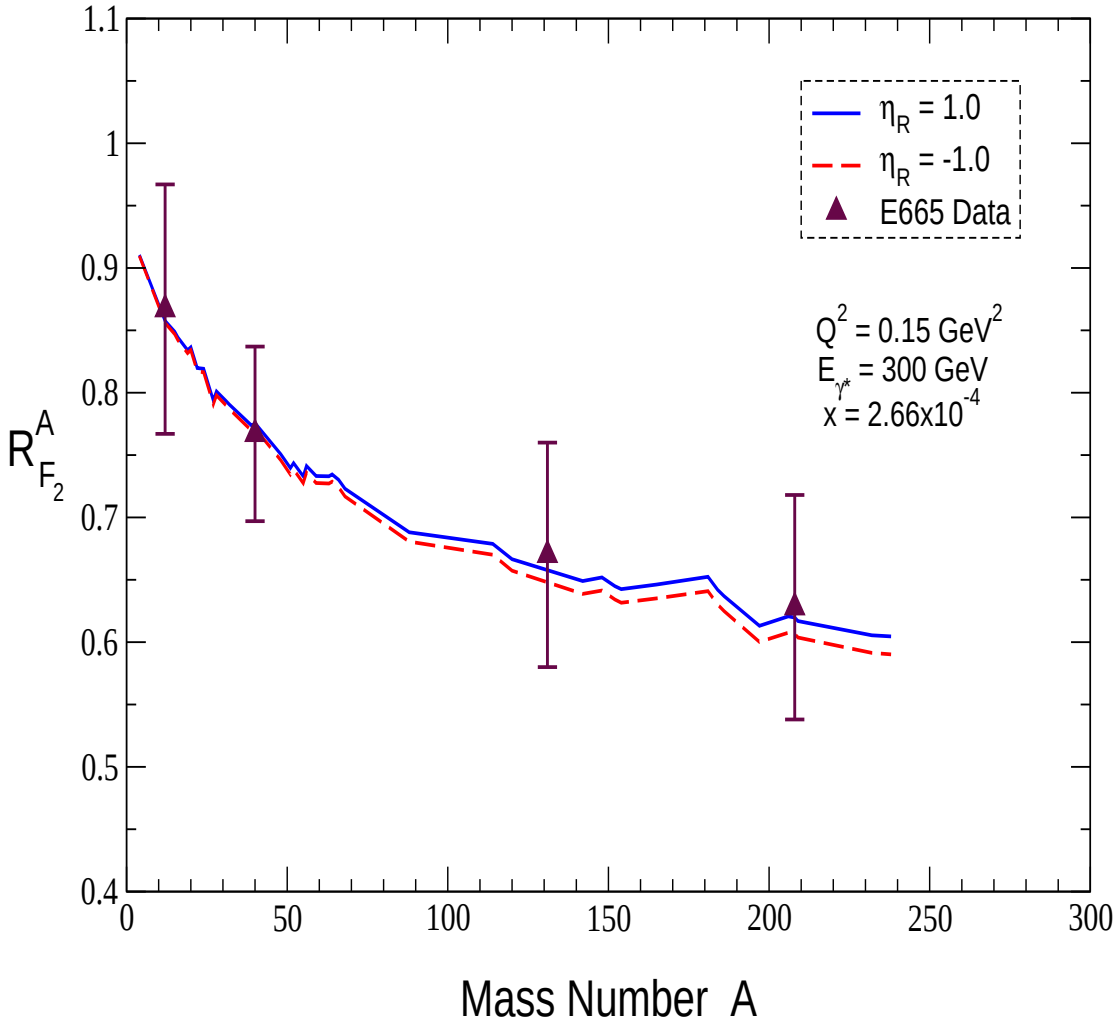


Fig. 4.7: (Color Online) Shadowing ratio at $W = 24$ GeV. The thick line is the result from both pomeron and subleading reggeons with $\eta = 1$ while the dashed line corresponds to pomeron+reggeons with with $\eta = -1$. The full triangles are data from the E665 experiment.

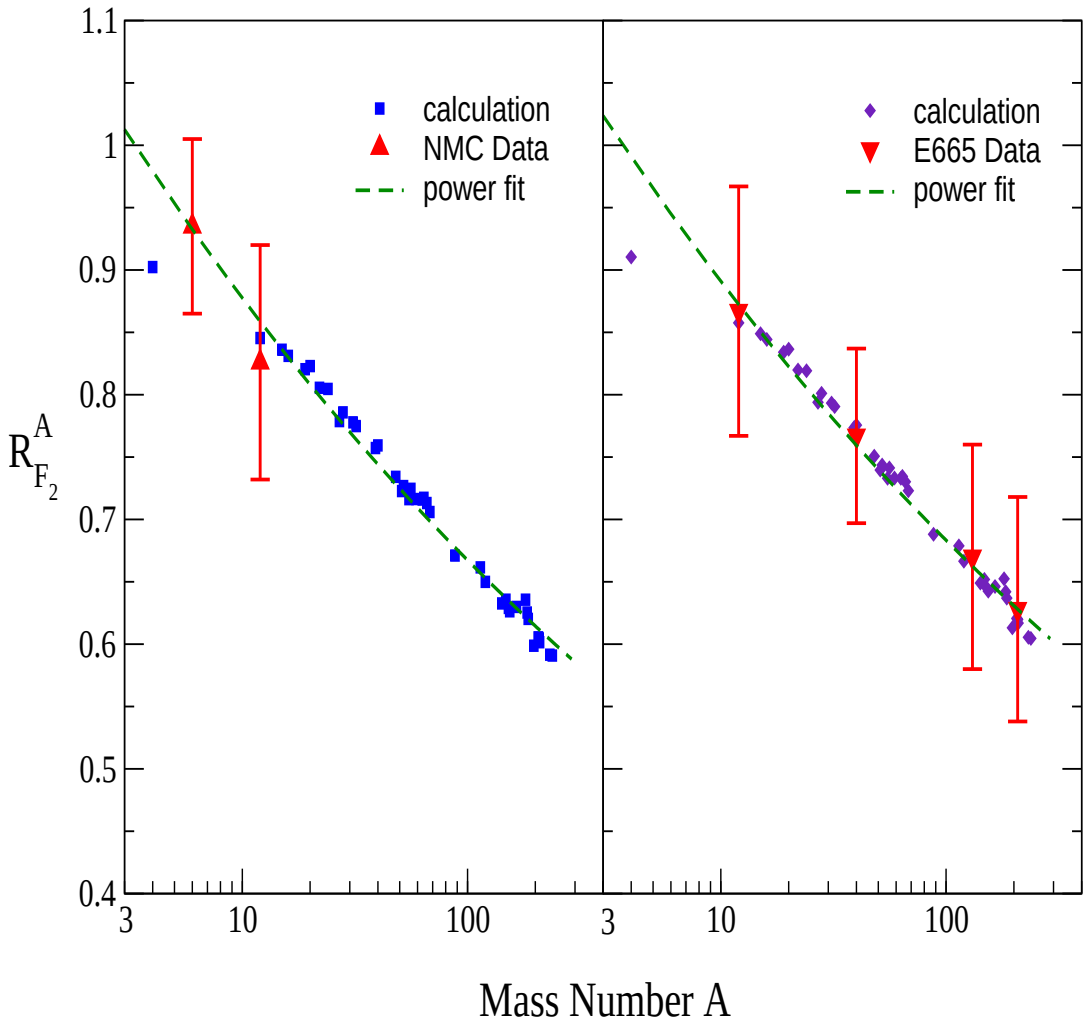


Fig. 4.8: (Color Online) Mass dependence of calculated shadowing ratio at small x for both the NMC (shaded squares) and E665 (shaded diamonds) kinematics. The dashed lines are fits according to Eq. (4.34) as described in the text.

4.5.3 Mass Dependence of Shadowing At Small x

The mass dependence of our calculated results is as shown in Fig. 4.8 for both the NMC and E665. The dashed lines represent a two-parameter fit of the standard form

$$\mathcal{R}_{F2}^{A} = \beta_0 A^{\beta_1 - 1} \tag{4.34}$$

to the calculated results, with fit parameters β_0 and β_1. For the NMC kinematics, $\beta_0 = 1.154$ and $\beta_1 = 0.881$ respectively. In the kinematical regime of the E665, $\beta_0 = 1.162$ and $\beta_1 = 0.885$ respectively.

4.6 A simple approximate picture of small-x shadowing

In this section we discuss a simple approximation to the formalism applied so far. This approximation furnishes a particularly simple picture of small-x shadowing in terms of a single parameter, the diffractive slope B.

We consider Eq. (4.12):

$$\delta\sigma_{\gamma^* A} = \frac{A(A-1)}{2A^2}\, 16\pi\, \mathcal{R}e \left[\frac{(1-i\eta)^2}{1+\eta^2} \int d^2b \int_{-\infty}^{\infty} dz_1 \int_{z_1}^{\infty} dz_2 \right.$$
$$\left. \int_{4m_\pi^2}^{W^2} dM_X^2 \left. \frac{d^2\sigma_{\gamma^* N}^{\rm diff}}{dM_X^2 dt} \right|_{t\approx 0} \rho_A^{(2)}(\vec{b}, z_1; \vec{b}, z_2)\ \exp\left\{ i \frac{(z_1 - z_2)}{\lambda} \right\} \right] \tag{4.35}$$

in the limit $\lambda \to \infty$ and $\eta = 0$. Then Eq. (4.35) simplifies to

$$\delta\sigma_{\gamma^* A} = \frac{A(A-1)}{2A^2}\, 16\pi \left[\int d^2b \int_{-\infty}^{\infty} dz_1 \int_{z_1}^{\infty} dz_2 \rho_A^{(2)}(\vec{b}, z_1; \vec{b}, z_2) \right.$$
$$\left. \int_{4m_\pi^2}^{W^2} dM_X^2 \left. \frac{d^2\sigma_{\gamma^* N}^{\rm diff}}{dM_X^2 dt} \right|_{t\approx 0} \right]. \tag{4.36}$$

Assuming a constant diffractive slope B in

$$\left. \frac{d^2\sigma_{\gamma^* N}^{\rm diff}}{dM_X^2 dt} \right|_{t\approx 0}, \tag{4.37}$$

we can carry out the integral over M_X^2 to yield:

$$\int_{4m_\pi^2}^{W^2} dM_X^2 \left. \frac{d^2\sigma_{\gamma^* N}^{\rm diff}}{dM_X^2 dt} \right|_{t\approx 0} = B\, \sigma_{\gamma^* N}^{\rm diff} \tag{4.38}$$

Thus the shadowing correction becomes

$$\delta\sigma_{\gamma^* A} = \frac{A(A-1)}{2A^2}\, 16\pi\, B\, \sigma^{\rm diff}_{\gamma^* N} \left[\int d^2b \int_{-\infty}^{\infty} dz_1 \int_{z_1}^{\infty} dz_2 \rho_A^{(2)}(\vec{b}, z_1; \vec{b}, z_2) \right], \tag{4.39}$$

and the shadowing ratio R is thus

$$R^A = 1.0 - \frac{(A-1)}{2A^2}\, 16\pi\, B\, \frac{\sigma^{\rm diff}_{\gamma^* N}}{\sigma_{\gamma^* N}} \left[\int d^2b \int_{-\infty}^{\infty} dz_1 \int_{z_1}^{\infty} dz_2 \rho_A^{(2)}(\vec{b}, z_1; \vec{b}, z_2) \right]. \tag{4.40}$$

Diffractive photo/leptoproduction of hadrons with mass $M_X^2 > 3$ GeV^2 at HERA and FNAL gives a range of values for the slope parameter B [66, 67, 83]:

$$B \simeq (5 \ldots 7)\ \text{GeV}^{-2}\ .$$

Diffractive production of low-mass vector mesons (ρ, ω, ϕ) from nucleons gives a wider range of values for B, depending on Q^2 and incident photon energy [66, 84]:

$$B \simeq (4 \ldots 10)\ \text{GeV}^{-2}\ .$$

From HERA at $x \simeq 10^{-4}$, the ratio of diffractive to total $\gamma^* N$ cross section is [69, 70, 71],

$$\frac{\sigma^{\rm diff}_{\gamma^* N}}{\sigma_{\gamma^* N}} \approx 0.1\ . \tag{4.41}$$

We use this value and $B \simeq (4 \ldots 10)$ GeV^{-2}. The result is shown in Fig. 4.9. As can be seen from the figure, values of B between 5 and 6 GeV^{-2} give good description of both NMC and E665 data.

4.7 Comparison with other related approaches and theoretical uncertainties

4.7.1 Comparison

We compare our results to two previous calculations similar in spirit to the present work.The approximate description treated in the last section is carried out in [2, 85]. Gaussian and square-well parameterizations are used to describe these nuclear densities. The ratio $\sigma^{\rm diff}_{\gamma^* N}/\sigma_{\gamma^* N} \simeq 0.1$ is used with $B \simeq 8$ GeV^{-2}. The calculated results are in good agreement with experimental data from the NMC and E665 experiments and are comparable to the results presented above.

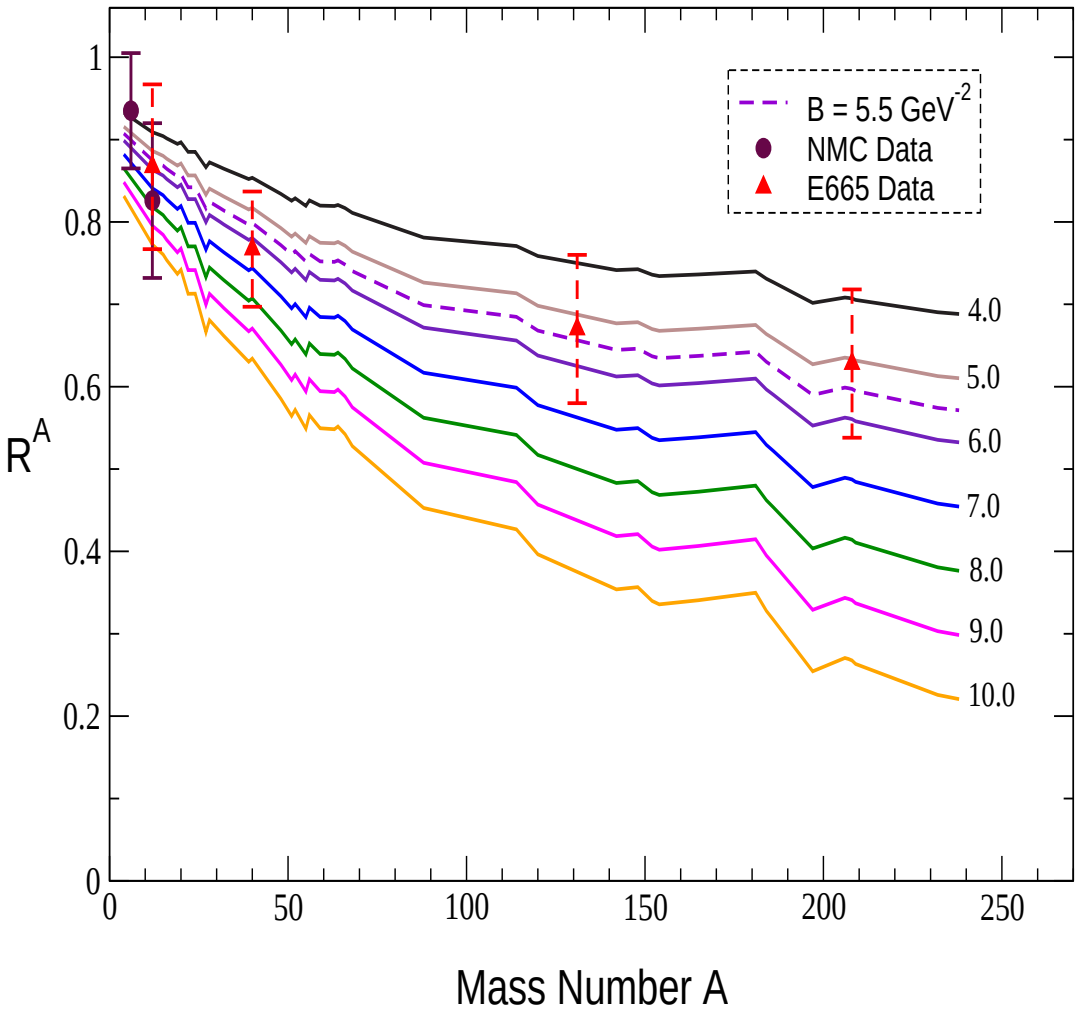


Fig. 4.9: (Color Online) Shadowing ratio calculated for different values of the diffractive slope B. Data are from the NMC (shaded circles) and E665 (shaded triangles) collaborations.

The approach in [86] is slightly different from that adopted in the present study. The basic equation is similar to Eq. (4.12) but a model form is utilized to describe the diffractive dissociation process. This model form is constructed to describe the HERA data adequately well. As in [2, 85] the real part of the amplitude is neglected. The same formalism is adopted in [87] where two models are used to account for higher order rescattering effects. Our results are comparable to the $x = 10^{-4}$ ratios of structure functions at $Q^2 = 5.0$ GeV^2 in [86] and the small-x $Q^2 = 0.5$ GeV^2 structure function ratios in [87] for the considered nuclei.

4.7.2 Uncertainties

The uncertainties of our calculation are directly related to the various uncertainties and approximations inherent in the practical usage of Eq. (4.14) to determine nuclear shadowing ratio. There are small but finite uncertainties in the nuclear density distribution parameters as well as the neglect of short-range correlations. The parameterizations of the diffractive dissociation cross section in different M_X^2 regions are the dominant sources of uncertainties. In the low-M_X^2 region described by vector meson dominance model (VMD), the largest contribution to the uncertainties comes from the vector-meson-nucleon cross sections. The delta function parameterization for the ω and ϕ mesons seems adequate, and the width of the ρ meson has been taken into account. Refinements of the spectral function (4.22) and improvements of the treatment of the ρ' resonance region are possible. In the continuum we have neglected interference between the pomeron and the subleading reggeons. Also the fit parameters at $W = 24$ GeV are subject to greater errors than the parameters from fits to actual experimental data. Furthermore, the use of an effective scattering cross section to account for multiple scattering is an approximation, as is using real-photon information ($Q^2 = 0$) at small, but non-vanishing Q^2.

Quantitatively, we estimate the overall uncertainty of our calculations as follows: we place a 10% uncertainty on the values of the vector-meson-nucleon cross sections used in the VMD calculations. The uncertainties in the fit parameters are as reported in Sec. 4.4. From Eq. (4.14) it can be seen that the uncertainties in the fit parameters propagate into uncertainties in the effective scatter-

ing cross section. We have therefore not placed any explicit uncertainty on the effective scattering cross section. We neglect the uncertainties in both $\alpha_{I\!P}(0)$ and $\alpha_{I\!R}(0)$ as well as in the other potential sources listed above. Since there are no experimental data in the interval between the FNAL energy (15.2 GeV) and the HERA energy (187 GeV), we place an additional 10% uncertainty on the $W = 24$ GeV fit parameters to offset the lack of constraints on the estimation of these parameters. We use Eq. (4.26) with $\eta_{I\!R} = 1$ to estimate the uncertainties at $W = 15.2$ and 24 GeV. The $\eta_{I\!R} = -1$ results are very similar. The percentage uncertainties are diplayed in Fig. 4.10.

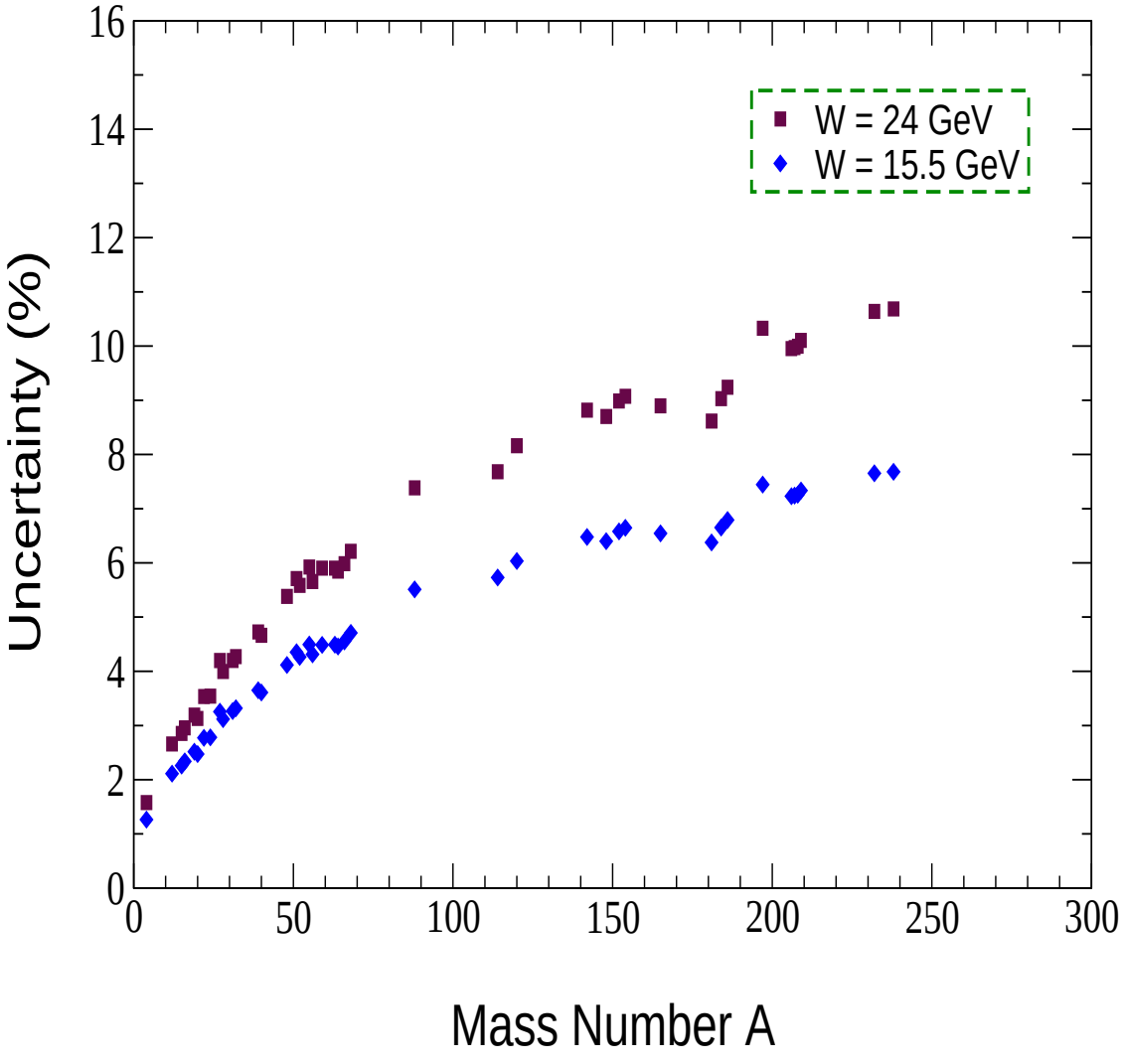


Fig. 4.10: (Color Online) Calculated uncertainties as discussed in the text for $\eta_{\mathbb{IR}} = 1$. From top: $W = 24$ GeV, $W = 15.5$ GeV.

CHAPTER 5

NUCLEAR PARTON DISTRIBUTIONS AND DEUTERON-GOLD (d+AU) COLLISIONS

In this chapter we apply nuclear parton distributions to calculate some experimentally observable quantities in d+Au collisions. These are the minimum bias nuclear modification factors, $R_{\rm dAu}$, central-to-peripheral ratios $R_{\rm CP}$, and pseudorapidity asymmetry, $Y_{\rm asy}$. Experimental data for comparison are from the BRAHMS collaboration [88] and the STAR collaboration [89]. Our results have been partially published in [90] and submitted for publication [91].

5.1 Introduction

In the rapidly-developing field of relativistic nuclear collision physics, questions related to the distribution of partons in nucleons and nuclei are of great current interest. The modification of the parton distribution functions (PDFs) in the nuclear environment has attracted growing attention ever since the pioneering EMC experiment[20, 92]. At the Relativistic Heavy Ion Collider (RHIC), we are well-positioned to study the nuclear PDFs (nPDFs) in a center-of-mass energy and transverse-momentum domain where perturbative Quantum Chromodynamics (pQCD) is expected to work well. Thus, hadron production in nuclear collision experiments at RHIC should provide information on how such nonperturbative ingredients of pQCD as the parton distribution functions are modified by the presence of the nuclear medium.

However, the description of nuclear collisions based on pQCD is a complicated task. Much of the complication derives from the intrinsically complex nature of the nuclear environment in collisions of heavy nuclei. In addition to the initial-state modification of the PDFs, the cross section of high-p_T hadron production is influenced by final-state effects (such as jet energy loss) and a complicated geometry. To better understand the physics of pQCD in the nuclear environment, it is

highly desirable to disentangle the different nuclear phenomena affecting high-p_T ($p_T \gtrsim 2$ GeV/c) hadron production. These phenomena (not present in proton-proton collisions) manifest themselves in e.g. the measured nuclear modification factors.

Deuteron-gold (d+Au) collisions provide a good compromise and testing ground for these purposes. The deuteron, being the simplest "real" nucleus, affords a complexity higher than a proton, but much less than that of a typical heavy nucleus like gold. Thus, a good understanding of d+Au collisions is invaluable in elucidating the added complexity associated with collisions of more complex heavy nuclei. Accordingly, d+Au collisions have been extensively studied at RHIC (see e.g. [88, 93, 94, 95]). A new feature, offered by nonidentical colliding beams like d+Au, is the pseudorapidity asymmetry, examined in some detail recently by the STAR collaboration[89].

As we have seen in Chapter 2, any pQCD calculation involves, in addition to partonic differential cross sections, parton distribution functions (PDFs) and (if final-state hadrons are measured) fragmentation functions (FFs) to connect to the observable level. The latter ingredients are nonperturbative, but universal in the absence of the nuclear environment. Typical pQCD-based calculations of nucleus-nucleus collisions use modified (nuclear) PDFs and deal with issues like jet energy loss (jet quenching) and collision geometry. In this work, we focus on the PDFs (and of course can not avoid treating the geometry of the collision). Even in the proton (nucleon), our knowledge of the PDFs is naturally limited; the nPDFs are much less well known in the wide range of momentum fraction x needed for reliable calculations. The nuclear gluon distribution, in particular, is poorly constrained. The uncertainties in the nPDFs directly affect the accuracy of pQCD calculations. It is therefore important not to rely on a single nPDF parameterization. Calculations utilizing different parameterizations offer a useful check on the performances of the different nPDFs in describing relevant observables.

In this chapter we compute nuclear modifications expressed in terms of the ratios R_{dAu} (nuclear modification factor, see eq. (5.12)) and R_{CP} (central-to-peripheral ratio, see eq. (5.13)). We also calculate the pseudorapidity asymmetry Y_{asy} (see eq. (5.14)) in certain pseudorapidity intervals. We focus attention on the phenomenon of nuclear shadowing, the difference between PDFs and nPDFs, leaving aside possible additional effects like jet quenching or intrinsic parton transverse

momentum and its broadening in nuclear collisions. In this way we establish a minimalist base line for experimental comparisons.

It should be noted that the nuclear modifications discussed in this chapter, as expressed in terms of $R_{\rm dAu}$, are somewhat different from the nuclear modifications discussed in Chapter 3. There the modifications are with respect to parton distributions, whereas here the modifications are with respect to cross sections, as will be discussed below. Since the calculation of cross sections necessarily involves nuclear parton distributions, the modifications in Chapter 3 are inherent in the underlying formalism and thus mainly responsible for the modifications manifest in $R_{\rm dAu}$.

5.2 Deuteron-gold Collisions: Basic Formalism

The invariant differential cross section for the d+Au→h+X reaction, with respect to pseudorapidity η and transverse momentum p_T can be written as

$$\frac{{\rm d}\sigma^h_{\rm dAu}}{{\rm d}\eta d^2p_T} = \sum_{abcd}\int {\rm d}^2b\ {\rm d}^2s\ {\rm d}x_a{\rm d}x_b{\rm d}z_c\ t_d(\vec{s})\ t_{Au}(|\vec{b}-\vec{s}|)F_{a/d}(x_a,Q^2,\vec{s},z)$$
$$F_{b/Au}(x_b,Q^2,|\vec{b}-\vec{s}|,z')\ \frac{{\rm d}\sigma(ab\to cd)}{{\rm d}\hat{t}}\ \frac{D_{h/c}(z_c,Q_f^2)}{\pi z_c^2}\hat{s}\,\delta(\hat{s}+\hat{t}+\hat{u})\ , \tag{5.1}$$

where x_a and x_b are parton momentum fractions in deuteron and gold, respectively, and z_c is the fraction of the parton momentum carried by the final-state hadron h. The factorization and fragmentation scales are Q and Q_f, respectively (see Sec.2.3 and 2.4). Here,

$$t_A(\vec{s}) = \int {\rm d}z\rho_A(\vec{s},z) \tag{5.2}$$

is the Glauber thickness function of nucleus A, with the nuclear density distribution, $\rho_A(\vec{s},z)$ subject to the normalization condition

$$\int {\rm d}^2s\ {\rm d}z\rho_A(\vec{s},z) = A\ . \tag{5.3}$$

The quantity ${\rm d}\sigma(ab\to cd)/{\rm d}\hat{t}$ in Eq. (5.1) represents the perturbatively calculable partonic cross section, and $D_{h/c}(z_c,{Q_f}^2)$ stands for the fragmentation function of parton c to produce hadron h, evaluated at momentum fraction z_c and fragmentation scale Q_f. Using the δ-function in Eq. (5.1), the integration over z_c can be carried out explicitly. Integration limits over x_a and x_b are then

($x_{a_{\min}}, 1$) and ($x_{b_{\min}}(x_a), 1$) respectively. Note that $x_{b_{\min}}$ is a function of x_a. In addition, z_c is also a function of both x_a and x_b.

In the present study, we are primarily concerned with $F_{a/A}(x, Q^2, \vec{s}, z)$, the nuclear parton distribution function (nPDF) for nucleus A. In light of the nuclear modifications discussed in Sec. 5.1, it is natural to assume that the nPDF depends on the location of the parton in the nucleus, $(\vec{s}, z)$ (or at least on its position relative to the beam axis $\vec{s}$). To connect this "inhomogeneous" nPDF to the geometry-independent (homogeneous) nPDF $\mathcal{F}_{a/A}(x, Q^2)$, the normalization condition

$$\int \mathrm{d}^2 s \; \mathrm{d}z \, \rho_A(\vec{s}, z) F_{a/A}(x, Q^2, \vec{s}, z) = \mathcal{F}_{a/A}(x, Q^2) \tag{5.4}$$

should be satisfied.

In the EPS08 [96], FGS [42], HIJING [54], and nDS [48] parameterizations the basic object is the (homogeneous) shadowing function $\mathcal{S}(x, Q^2)$ which encodes the nuclear modifications at all relevant x and Q^2. The nPDF can then be written as

$$\mathcal{F}_{a/A}(x, Q^2) = \mathcal{S}(A, x, Q^2) f_{a/N}(x, Q^2) \; , \tag{5.5}$$

where $f_{a/N}(x, Q^2)$ is any available PDF of the nucleon, which can be expressed as

$$f_{a/N}(x, Q^2) = \frac{Z}{A} f_{a/p}(x, Q^2) + (1 - \frac{Z}{A}) f_{a/n}(x, Q^2) \; , \tag{5.6}$$

with $f_{a/p}(x, Q^2)$ [$f_{a/n}(x, Q^2)$] being the proton [neutron] parton distribution function as a function of Bjorken x and factorization scale Q. The HKN07 [97] parameterization assumes this form at the initial scale Q_0^2 to generate the nPDFs at this initial scale, and then evolves to obtain nPDFS at other relevant Q^2.

We can define an inhomogenous shadowing function as

$$S'(A, x, Q^2, \vec{s}, z) = 1 + N_\Phi [S(A, x, Q^2) - 1] \Phi(\vec{s}, z) \, , \tag{5.7}$$

with $\Phi(\vec{s}, z)$ a dimensionless function of the relevant spatial coordinates and N_Φ a suitable normalization constant such that

$$\frac{1}{A} \int d^2 s dz \rho_A(\vec{s}, z) S'(A, x, Q^2, \vec{s}, z) = S(A, x, Q^2) \, . \tag{5.8}$$

Here $S(A, x, Q^2)$ denotes the homogenous shadowing function. The dimensionless function $\Phi(\vec{s}, z)$ encodes the spatial dependence of nuclear shadowing. We take the thickness function as an assumed form for $\Phi(\vec{s}, z)$. Another suitable form is using the local nuclear density.

We obtain the density distribution of the deuteron from the Hulthen wave function [98] (as in Ref. [99]), while a Woods-Saxon density distribution is used for gold with parameters from Ref. [82]. Since the Nijmegen deuteron wave function [100], which we also applied, gives similar results to the Hulthen wave function, we report only the calculations using the Hulthen wave function here.

We fix the scales as $Q = Q_f = p_T$, where p_T is the final hadronic transverse momentum. We also carried out calculations with the scales $Q = p_T/z_c$, $Q_f = p_T$. Results with the latter choice do not differ significantly from those obtained by having both scales fixed at p_T. The partonic differential cross sections, $\mathrm{d}\sigma(ab \to cd)/\mathrm{d}\hat{t}$ were evaluated at leading order (LO). For next-to-leading order (NLO) applications, we use a K factor to approximate the effects of higher orders. These effects tend to cancel though, in the ratios calculated in the present study. For the fragmentation functions we use the DSS set[101] throughout. The DSS fragmentation functions are available in both LO and NLO forms. We use the MRS98 [102] LO and NLO nucleon parton distributions throughout for consistency with the HKN07[97] parameterization where the underlying PDFs are the MRS98 set.

We employ three different nPDFs in the present study: EPS08[96] (an update of EKS[43], incorporating RHIC data at forward rapidity), FGS[42], and HKN07[97]. EPS08 is avilable only in LO, whereas FGS is available only in NLO. HKN07 is available in both LO and NLO forms. For consistency, we use LO EPS08 and HKN07 with LO DSS fragmentation functions. NLO DSS are used in conjuction with FGS and NLO HKN07. While EPS08 and HKN07 are similar in the sense that they are global fits to experimental data, FGS utilizes Gribov theory and diffractive deep inelastic scattering to derive nPDFs. Gluon shadowing is stronger in FGS than in EPS08 and HKN07. Because nuclear gluon distributions are poorly constrained experimentally, there are significant differences between the EPS08 and HKN07 gluon shadowing. On the other hand, since the Gribov formalism is not capable to predict valence quark shadowing, FGS uses EKS[43] shadowing for va-

lence quarks, and all three parameterizations are in agreement for valence quark shadowing. For sea quarks, EPS08 and HKN07 are in good agreement at $0.01 \lesssim x \lesssim 0.1$. At $x \gtrsim 0.2$ and in the small-x region $x \lesssim 0.01$ there are substantial deviations. The FGS predicts more nuclear shadowing for sea quarks than EPS08 and HKN07. Due to the x-integration, different nuclear effects [shadowing ($x \lesssim 0.1$, depletion), antishadowing ($0.1 \lesssim x \lesssim 0.3$, enhancement), EMC effect ($0.3 \lesssim x \lesssim 0.7$, depletion), etc] are superimposed, thus it is difficult to isolate these effects.

Since pQCD calculations are generally not reliable at low p_T, we do not wish to push our calculations below $p_T = 1.5$ GeV/c. With our scale choice, this corresponds to a minimum Q^2 (Q_f^2) of 2.25 GeV^2, while EPS08, FGS, and HKN07 give $1.69, 4.0$, and 1.0 GeV^2 for minimum Q^2, respectively. The minimum Q_f^2 for the DSS fragmentation functions is given as 1.0 GeV^2.

5.3 Minimum Bias Nuclear Modification Factor

The d+Au nuclear modification factor, $R_{\rm dAu}$ is defined as

$$R_{\rm dAu}(p_T) = \frac{\dfrac{1}{\langle N_{\rm bin}\rangle}\dfrac{{\rm d}\sigma^h_{\rm dAu}}{{\rm d}\eta\ {\rm d}^2p_T}}{\dfrac{{\rm d}\sigma^h_{pp}}{{\rm d}\eta\ d^2p_T}}\ , \tag{5.9}$$

where the average number of binary collisions, $\langle N_{\rm bin}\rangle$ in the various impact-parameter bins is given by

$$\langle N_{\rm bin}\rangle = \langle \sigma^{\rm in}_{NN}\, T_{\rm dAu}(b)\rangle\ . \tag{5.10}$$

Here $\sigma^{\rm in}_{NN}$ is the inelastic nucleon-nucleon cross section, and

$$T_{\rm dAu}(b) = \int {\rm d}^2s\ t_d(\vec{s})\ t_{Au}(|\vec{b}-\vec{s}|) \tag{5.11}$$

represents the deuteron-gold nuclear overlap function. The nuclear modification factor $R_{\rm dAu}$ is thus just the ratio of the d+Au and proton-proton (pp) cross sections, normalized by the average number of binary collisions, $\langle N_{\rm bin}\rangle$.

For minimum bias (integrating over all impact parameters), $\langle N_{\rm bin}\rangle = A_d \times A_{Au} = 394$ and

thus the modification factor becomes

$$R_{\rm dAu}(p_T) = \frac{\dfrac{1}{394}\dfrac{{\rm d}\sigma^h_{\rm dAu}}{{\rm d}\eta\,{\rm d}^2p_T}}{\dfrac{{\rm d}\sigma^h_{pp}}{{\rm d}\eta\,d^2p_T}}\ , \tag{5.12}$$

which is reminiscent of the nuclear ratio, Eq. (3.4), which encodes the nuclear modifications of parton distributions. Here though, we are at the level of differential cross sections whereas the nuclear ratio is at the level of structure functions.

The nuclear modification factors $R_{\rm dAu}$ have been measured at several pseudorapidities by the BRAHMS Collaboration, and are presented at $|\eta| \leq 0.2\,(\eta = 0)$, $0.8 \leq \eta \leq 1.2\,(\eta = 1)$, $1.9 \leq \eta \leq 2.35\,(\eta = 2.2)$, and $2.9 \leq \eta \leq 3.5\,(\eta = 3.2)$[88]. At small rapidities ($\eta = 0, 1$), the data are given for the sum of charged hadrons, while at forward rapidities negatively charged hadron data are available. The DSS fragmentation functions for average charged hadrons are employed for all calculations. It should be remembered that the calculated results for all rapidities are therefore for the average of charged hadrons.

We have calculated the minimum bias $R_{\rm dAu}$ for total charged hadron production at the BRAHMS pseudorapidities with the three nuclear parton distribution functions considered in this study. In the case of the FGS nPDFs we use the strong gluon shadowing for the gold nucleus. We have only calculated the p_T distributions for final-state total charged hadrons in the present study, since we are mainly interested in the performance of the different nPDFs. More detail for different hadron species and fractional contributions from quarks, antiquarks, and gluons for EKS and FGS nPDFS can be found in [103]. Here we limit our discussion of nuclear modification factors to the effect of the different nPDFs. We make two general observations:

i) At midrapidity (small η), processes initiated by both gluons and quarks are important. At forward rapidities (large η), x_b, the parton momentum fraction in gold becomes small and gluon-initiated processes become dominant.

ii) In both, the data and the calculations, $R_{\rm dAu}$ decreases systematically with increasing η. This reflects the increasing role of shadowing since smaller values of x_b are probed at forward rapidities.

It should be kept in mind that the range of integration over the partonic momentum fraction in the gold nucleus, x_b, is $(x_{bmin}, 1)$. Thus $x_{b_{\min}}$ gives an indication of the relevant contributions of the different regions (shadowing, antishadowing, etc) to the cross section. In Fig. 5.1 we display the variation of $x_{b_{\min}}$ with the transverse momentum p_T for the four BRAHMS pseudorapidity intervals. For each interval we calculate $x_{b_{\min}}$ for both the upper and lower limits of pseudorapidity. Shadowing corresponds to $x_b \lesssim 0.05$.

The results of our calculations are displayed in Fig. 5.2, together with the experimental data.

At $\eta = 0$ and $p_T < 2$ GeV/c, typical $x_{b_{\min}}$ values are significantly below 0.1. Thus there is substantial contribution from the shadowing region, and all three nPDFs predict $R_{\rm dAu} < 1$. Due to their steeper rise of $R_{\rm dAu}$ with p_T, the EPS08 and FGS nPDFs appear to describe the data better at around $p_T = 3 \sim 5$ GeV/c than the HKN07 nPDFs. At $p_T = 4$ GeV/c, $x_{b_{\min}}$ is close to the upper limit of shadowing, thus there is little contribution from the shadowing region. There is more contribution from the antishadowing region, and consequently $R_{\rm dAu} > 1$, with the HKN07 being the lowest. At $p_T = 8$ GeV/c, we have major contributions from both antishadowing and the EMC effect. Thus, while $R_{\rm dAu}$ is still > 1, the trend is towards 1 for both EPS08 and FGS. The HKN07 parameterization predicts a higher value at around 1.1.

The behavior is similar at $\eta = 1$. For $p_T < 3$ GeV/c both $x_{b_{\min}}$ values are small, and thus $R_{\rm dAu} < 1$. Around this p_T the HKN07 is identical with the FGS. At $p_T = 4$ GeV/c, $x_{b_{\min}}$ ranges higher, with $R_{\rm dAu} > 1$. The HKN07 is significantly below EPS08 and slightly below FGS in this region. At $p_T > 8$ GeV/c, $R_{\rm dAu} > 1$ with substantial contributions from both antishadowing and the EMC effect. All three are in good agreement with data except at low p_T, where the data are more suppressed than the calculated results.

The effect of increasing η is already apparent at $\eta = 2.2$, where all parameterizations predict $R_{\rm dAu} < 1$ for $p_T < 4$ GeV/c. The major contribution is from shadowing with the resultant $R_{\rm dAu} < 1$. The FGS is practically 1 for $p_T > 5$ GeV/c while $R_{\rm dAu} > 1$ for both EPS08 and HKN07. This is due to the stronger gluon shadowing in the FGS parameterization. The agreement with data is reasonable, although the reach of the data is rather poor ($p_T < 4$ GeV/c).

At $\eta = 3.2$ the dominant contribution is again from shadowing with $R_{\rm dAu} < 1$ for $p_T < 6$

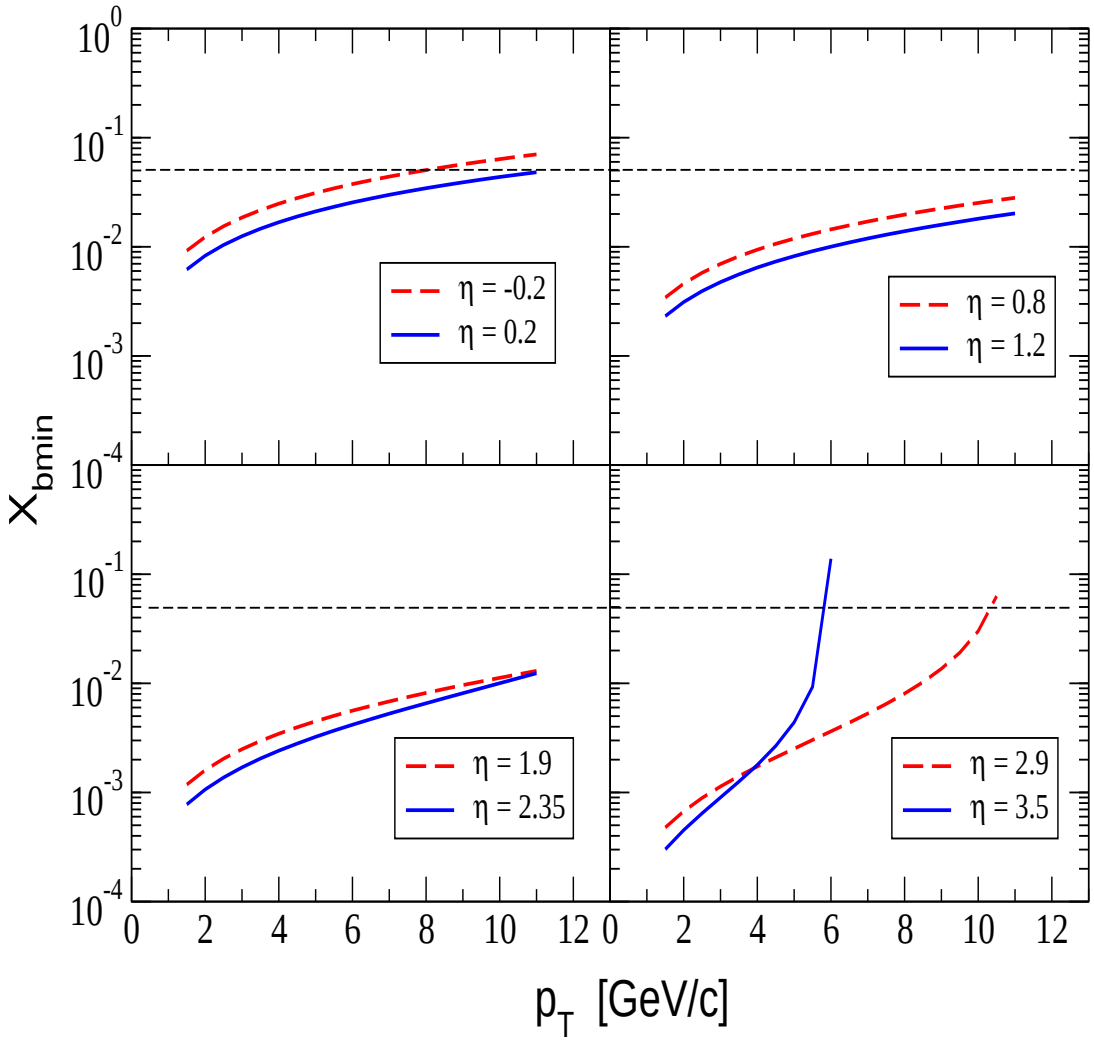


Fig. 5.1: (Color Online) $x_{b_{\min}}$ as a function of p_T for the four BRAHMS pseudorapidity intervals. The horizontal dashed line corresponds to $x_{bmin} = 0.05$, the approximate upper limit for shadowing.

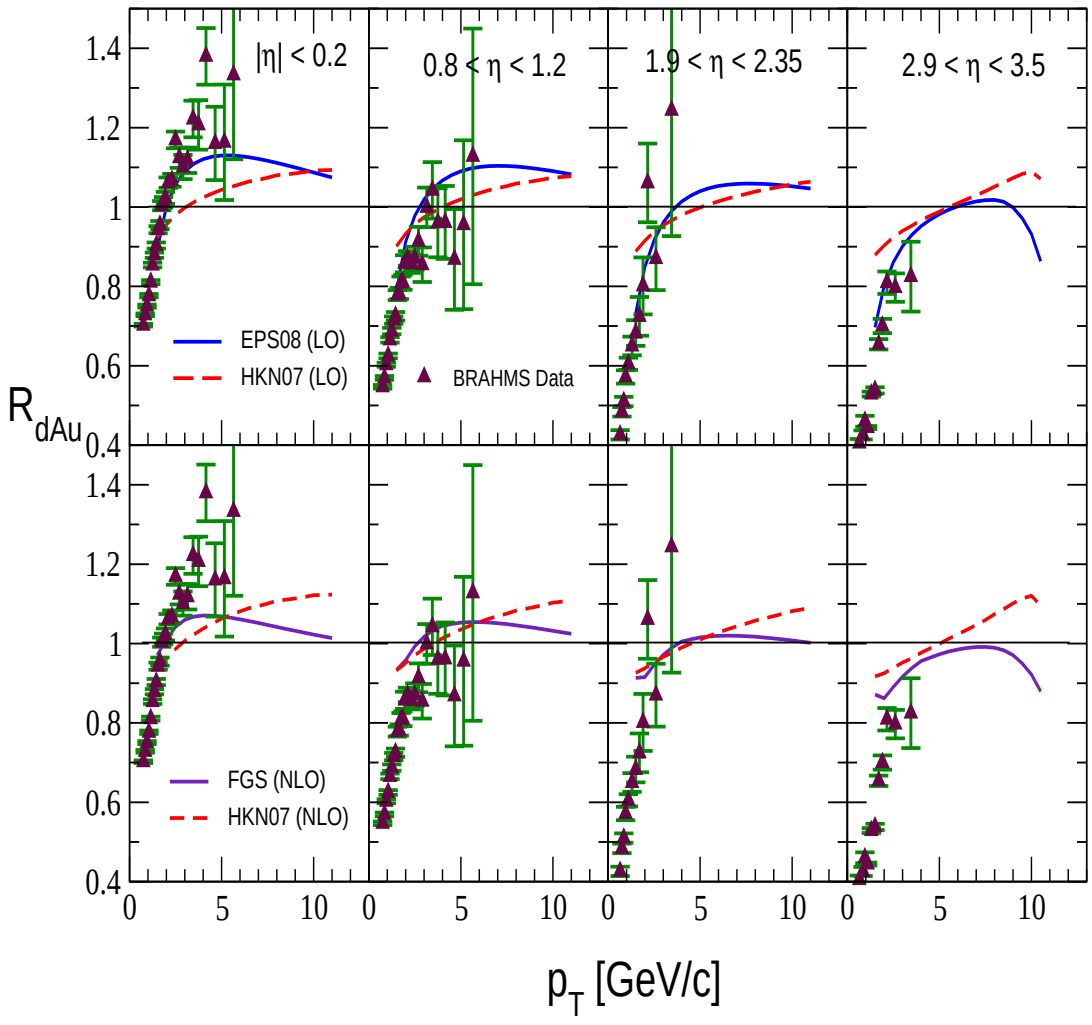


Fig. 5.2: (Color Online) Minimum bias nuclear modification factor R_{dAu} for total charged hadron production at different pseudorapidities. The solid line represents the EPS08 nPDFS (upper panels) and the FGS nPDFs (lower panels). The dashed line corresponds to the HKN07 LO (NLO) nPDFs for upper (lower) panels respectively. In the intervals $|\eta| \leq 0.2$ and $0.8 \leq \eta \leq 1.2$, the data are for average charged hadrons, while for the intervals $1.9 \leq \eta \leq 2.35$ and $2.9 \leq \eta \leq 3.5$, only negative hadrons are measured. The error bars represent statistical errors.

GeV/c for HKN07 while both FGS and EPS08 give $R_{\rm dAu} < 1$ essentially for all p_T. At low p_T the EPS08 describes the data best while at high p_T it is similar to the FGS. The HKN07 is less suppressed at high p_T than both EPS08 and FGS. As in the case of $\eta = 2.2$, the data is limited to $p_T < 4$ GeV/c.

5.4 Central-to-Peripheral Ratios

A related ratio, which dispenses with the need for a reference pp cross section and uses information from the same experiment in numerator and denominator, thus canceling most systematic errors, is the central to peripheral ratio defined as

$$R_{\rm CP}(p_T) = \frac{\dfrac{1}{\langle N_{\rm bin}\rangle_C}\dfrac{{\rm d}\sigma^{h\,C}_{\rm dAu}}{{\rm d}\eta\,{\rm d}^2p_T}}{\dfrac{1}{\langle N_{\rm bin}\rangle_P}\dfrac{{\rm d}\sigma^{h\,P}_{\rm dAu}}{{\rm d}\eta\,{\rm d}^2p_T}}\ , \tag{5.13}$$

where $\langle N_{\rm bin}\rangle$ is as defined in Eq. (5.10). The label C stands for the central event class, while P denotes the peripheral class. The centrality classes are chosen according to centrality cuts on the experimental data.

The BRAHMS data are given in three centrality classes: central (0-20)%, semicentral (30-50)%, and peripheral (60-80)% (as a percentile of the geometric cross section). With a Woods-Saxon density for gold and the Hulthen wave function for the deuteron, a Glauber calculation of $T_{\rm dAu}$ relates these classes to impact parameter intervals as[103] $0 \le b \le 3.81$ fm for central, $4.66 \le b \le 6.01$ fm for semicentral, and $6.59 \le b \le 7.74$ fm for peripheral. It should be noted that our calculation assumes exact impact parameter cuts while, experimentally, impact parameter is poorly measured on an event-by-event basis in $d + Au$ collisions. We will use the notation $R_{\rm CP}$ to refer to the central-to-peripheral ratio, while $R_{\rm SP}$ will be used to denote the semicentral-to-peripheral ratio in the following.

The results of our central-to-peripheral ratio ($R_{\rm CP}$) calculation are displayed in Fig. 5.3, together with the BRAHMS data. At $\eta = 0$, where the data indicate an $R_{\rm CP} > 1$ at $2 \lesssim p_T \lesssim 4$ GeV/c, the calculated results are below the data, while at both $\eta = 2.2$ and $\eta = 3.2$ the data show significant suppression, with the calculations giving $R_{\rm CP}$ close to unity. At $\eta = 1$ the calculation can be said

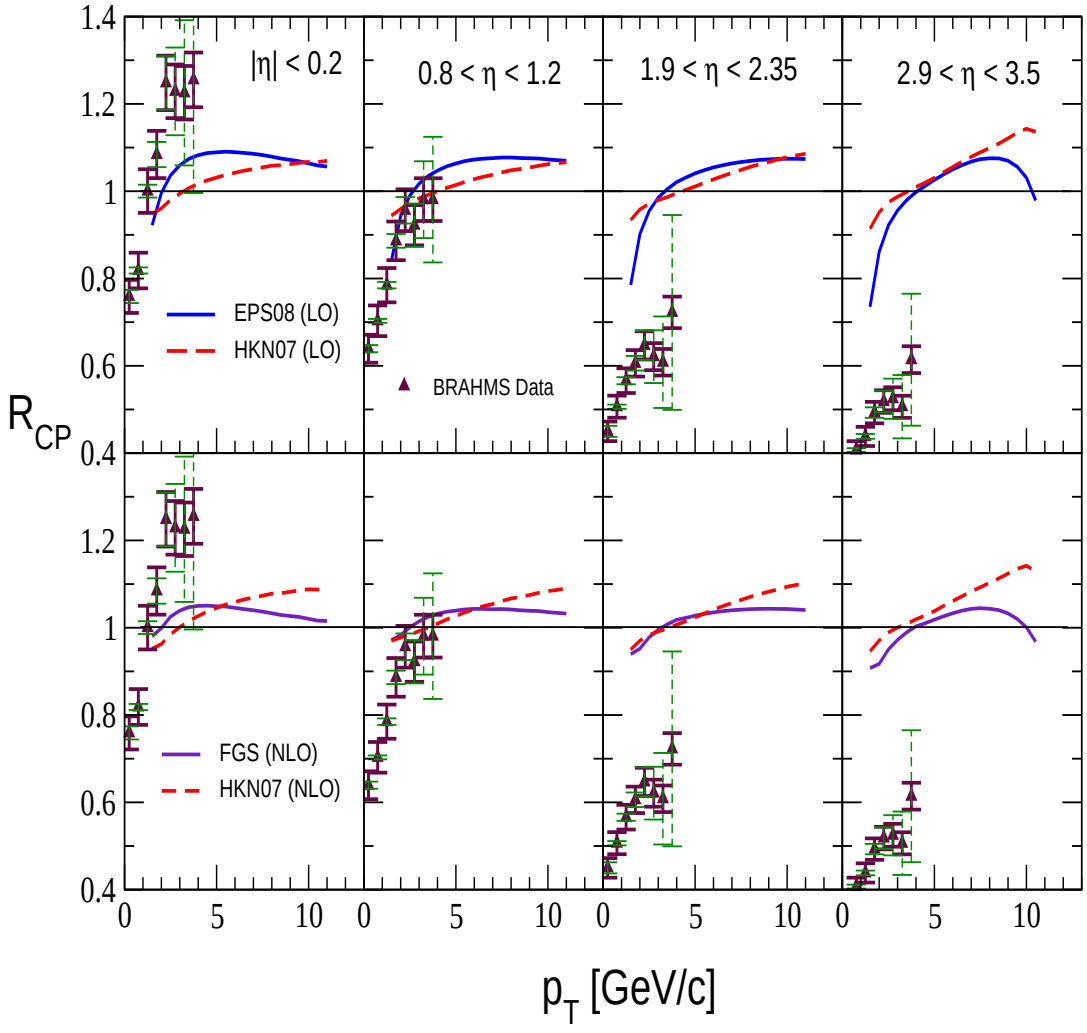


Fig. 5.3: (Color Online) Central-to-peripheral ratio $R_{\rm CP}$ for total charged hadron production at different pseudorapidities. The solid line represents the EPS08 nPDFS (upper panels) and the FGS nPDFs (lower panels). The dashed line corresponds to the HKN07 LO (NLO) nPDFs for upper (lower) panels respectively. Solid triangles denote BRAHMS data. In the intervals $|\eta| \leq 0.2$ and $0.8 \leq \eta \leq 1.2$, the data are for average charged hadrons, while for the intervals $1.9 \leq \eta \leq 2.35$ and $2.9 \leq \eta \leq 3.5$, only negative hadrons are measured. The solid error bars are systematic errors, while dashed error bars represent statistical errors.

to be in reasonable agreement with the data. Although the calculation exhibits the trend toward increasing suppression in the data as η increases, the calculated variation with η is much smaller than the one shown by the data. This shortcoming becomes increasingly evident at forward rapidities. Fig. 5.4 shows the calculated semicentral-to-peripheral ratio, $R_{\rm SP}$, using the three nPDFs, together with the BRAHMS data. The situation here mirrors that of the central-to-peripheral ratios. The results underpredict the data at $\eta = 0$, but overpredict at forward rapidities. The degree of suppression at forward rapidities is not as severe as in the central-to-peripheral ratios. In fact, due to the large error bars, there is reasonable agreement with data at p_T around 4 GeV/c.

Both $R_{\rm CP}$ and $R_{\rm SP}$ are geometry-dependent, thus the assumed spatial dependence of shadowing is important. We have checked that shadowing proportional to the local density gives worse agreement with data than shadowing proportional to the thickness function. A variation of the thickness function dependence where we used higher powers gives better agreement at $\eta = 0$ but still overpredicts significantly at other rapidities. With these shadowing parameterizations, a more radical spatial dependence is needed to describe the data for both ratios. Another factor that may be responsible is a too-weak x-dependence of the available shadowing parameterizations.

The absence of spatial dependency in minimum bias nuclear modification factor calculations plays an important role in the apparent better agreement of calculated results with experimental data. Even though the central-to-peripheral ratios should be more reliable experimentally due to the cancellation of systematic errors, the theoretical calculations of these ratios are heavily dependent on the totally unknown spatial dependence of the parton distributions and also the necessity of sharp impact parameter cuts. These constraints are primarily responsible for the apparently worse agreement of the calculated results with experimental data.

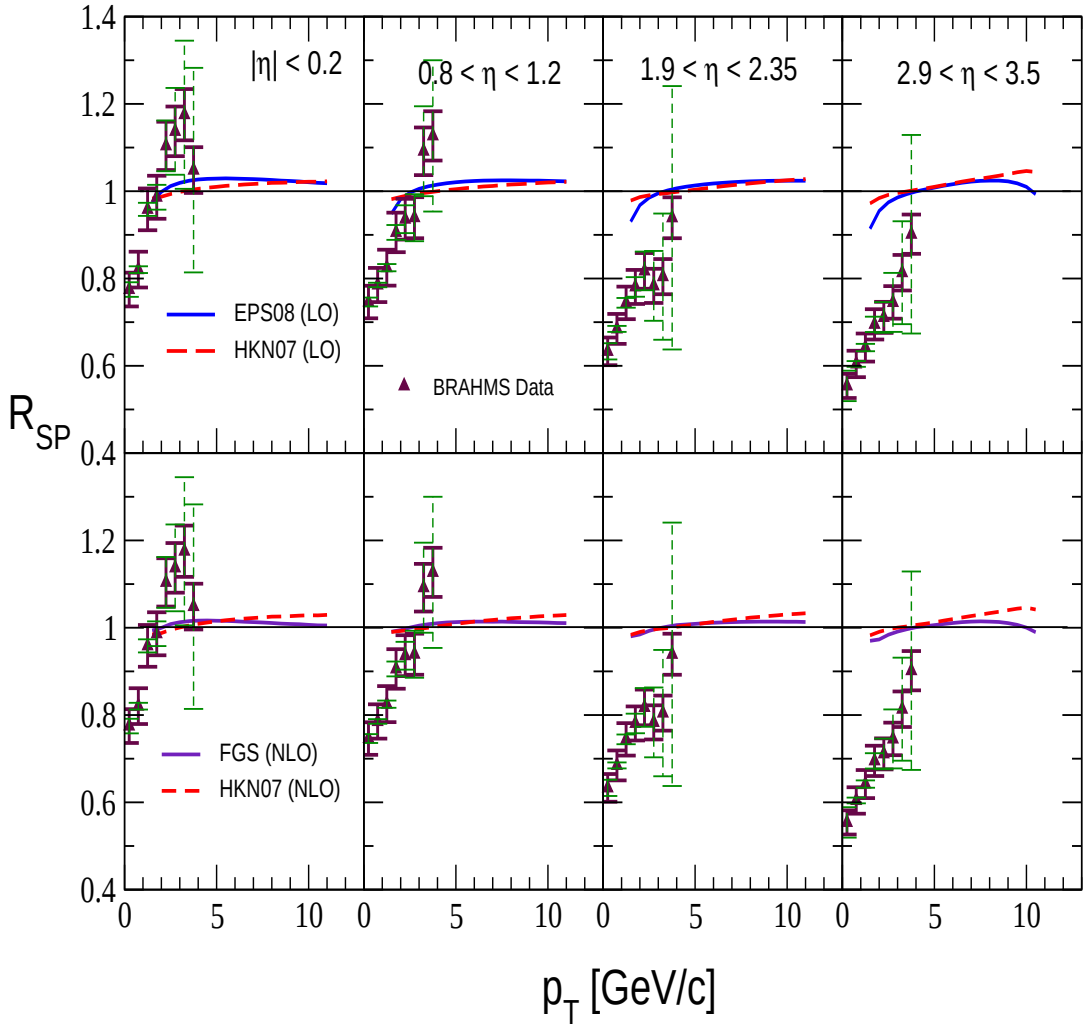


Fig. 5.4: (Color Online) Semicentral-to-peripheral ratio $R_{\rm CP}$ for total charged hadron production at different pseudorapidities. The solid line represents the EPS08 nPDFS (upper panels) and the FGS nPDFs (lower panels). The dashed line corresponds to the HKN07 LO (NLO) nPDFs for upper (lower) panels respectively. Solid triangles denote BRAHMS data. In the intervals $|\eta| \leq 0.2$ and $0.8 \leq \eta \leq 1.2$, the data are for average charged hadrons, while for the intervals $1.9 \leq \eta \leq 2.35$ and $2.9 \leq \eta \leq 3.5$, only negative hadrons are measured. The solid error bars are systematic errors, while dashed error bars represent statistical errors.

5.5 Pseudorapidity Asymmetry

As the mechanisms for hadron production in d+Au collisions may be different at forward rapidities (deuteron side) and backward rapidities (gold side), it is of interest to study ratios of particle yields between a given rapidity value and its negative in these collisions. The STAR Collaboration has measured pseudorapidity asymmetries[89], defined as

$$Y_{asy} = \frac{\frac{\mathrm{d}\sigma^{h}_{\mathrm{dAu}}}{\mathrm{d}\eta\,\mathrm{d}^2 p_T}(\text{Au-side})}{\frac{\mathrm{d}\sigma^{h}_{\mathrm{dAu}}}{\mathrm{d}\eta\,\mathrm{d}^2 p_T}(\text{d-side})} \quad , \tag{5.14}$$

in d+Au collisions for several identified hadron species and total charged hadrons in the pseudorapidity intervals $|\eta| \leq 0.5$ and $0.5 \leq |\eta| \leq 1.0$. Rapidity asymmetries with the backward/forward ratio above unity for transverse momenta up to ≈ 5 GeV/c are observed for charged pion, proton+antiproton, and total charged hadron production in both rapidity regions. We want to see if different nPDFs give significantly different rapidity asymmetries for the various hadron species.

In d+Au collisions at small rapidities, particle production may include contributions from gold-side partons that may have been modified by nuclear effects and from deuteron-side partons that have experienced multiple scattering while traversing the gold nucleus [89]. It should be kept in mind that the latter effect is not included in the present calculations.

We have calculated Y_{asy} for charged pions ($\pi^+ + \pi^-$), charged kaons, protons+antiprotons ($p + \bar{p}$), and total charged hadrons ($h^+ + h^-$). Below 2 GeV/c, data are available for total charged hadrons only. Above 2 GeV/c, separated data exist for $\pi^+ + \pi^-$ and for $p + \bar{p}$. A benefit of using a ratio is that the systematic errors largely cancel and are $\lesssim 5\%$ for both pions and protons, $< 3\%$ for charged hadrons [89]. For $p_T \lesssim 4.2$ GeV/c the errors are dominantly systematic and thus the statistical errors are not displayed. At higher p_T statistical errors tend to become dominant. Since the asymmetry is a ratio of the yields in two different rapidity intervals, the respective x_b-distributions are mostly responsible for the global trends observed in the calculations.

5.5.1 Pseudorapidity and nuclear modifications

Consider the (double) ratio of the forward and backward nuclear modification factors in dAu collisions for species h:

$$R^h_\eta(p_T) = \frac{R^h_{\rm dAu}(p_T,-\eta)}{R^h_{\rm dAu}(p_T,\eta)} = \frac{E_h {\rm d}^3\sigma^h_{\rm dAu}/{\rm d}^3p|_{-\eta}}{E_h {\rm d}^3\sigma^h_{pp}/{\rm d}^3p|_{-\eta}} \Bigg/ \frac{E_h {\rm d}^3\sigma^h_{\rm dAu}/{\rm d}^3p|_{\eta}}{E_h {\rm d}^3\sigma^h_{pp}/{\rm d}^3p|_{\eta}} \ . \tag{5.15}$$

As discussed in Ref. [91], since the pp rapidity distribution is symmetric around $\eta = 0$, if the same backward and forward (pseudo)rapidity ranges are taken in both directions (i.e. $|\eta_{min}| \leq |\eta| \leq |\eta_{max}|$), then the pp yields cancel in eq. (5.15) and one obtains that the ratio defined in (5.15) is identical to the pseudorapidity asymmetry (5.14):

$$Y^h_{\rm asy}(p_T) = R^h_\eta(p_T) = \frac{R^h_{\rm dAu}(p_T,-\eta)}{R^h_{\rm dAu}(p_T,\eta)} \ . \tag{5.16}$$

As an illustration we display, in Fig. 5.5, this connection for pion production in the two STAR intervals, $|\eta| \leq 0.5$ and $0.5 \leq |\eta| \leq 1.0$, for both EPS08 and HKN07 LO nPDFs. The features displayed are common to all hadronic species considered in the rest of this study.

5.5.2 Minimum-bias asymmetry: $|\eta| \leq 0.5$

Fig. 5.6 shows the result of our pseudorapidity asymmetry ratio calculations for the interval $|\eta| \leq 0.5$, together with the STAR data[89]. We plot the calculated results with the EPS08 (solid line,upper panels), FGS (solid line,lower panels), and HKN07 (dashed, LO upper panels, NLO lower panels) nuclear parton distributions. Around $\eta = 0$ one expects the degree of asymmetry to be small. This is borne out by both data and calculation. At very low p_T, there is more contribution from the shadowing region for the positive rapidity (deuteron-side) than the negative rapidity (gold-side). Thus the ratio is expected to be above unity. For $p_T > 3$ GeV/c, the x_b distributions are similar, with less contribution from the shadowing region as p_T increases. Thus the asymmetry is not far from unity. The EPS08 and FGS nPDFs give similar results for all hadronic species. The HKN07 nPDFs yield a different curvature and pseudorapidity asymmetries that remain above unity for a

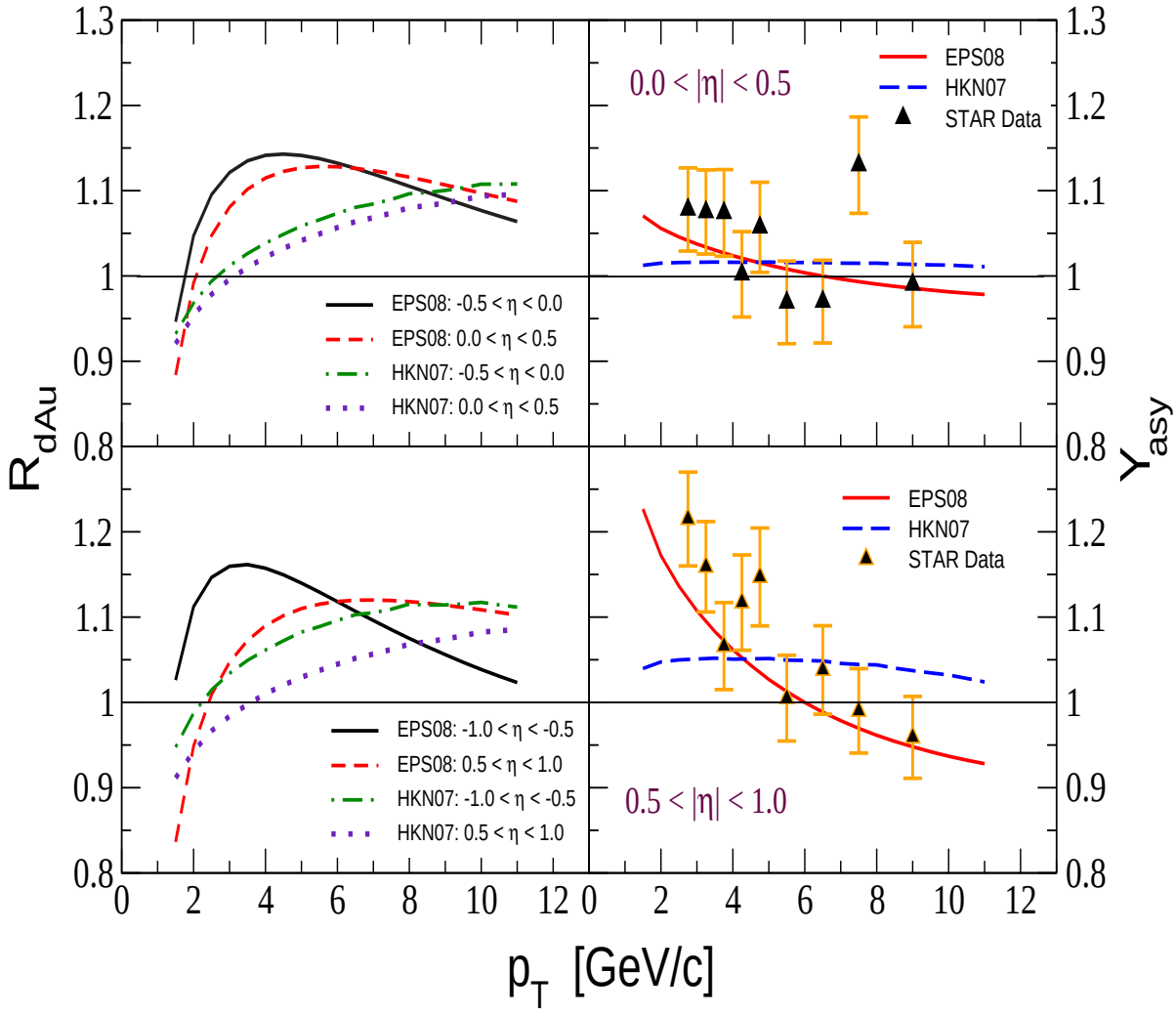


Fig. 5.5: (Color Online) Nuclear modifications, $R_{\rm dAu}$, (left panels), and pseudorapidity asymmetry, Y_{asy}, (right panels), for pions at $|\eta| \leq 0.5$ and $0.5 \leq |\eta| \leq 1.0$ using EPS08 and HKN07 LO nPDFs. Filled triangles denote the STAR data.

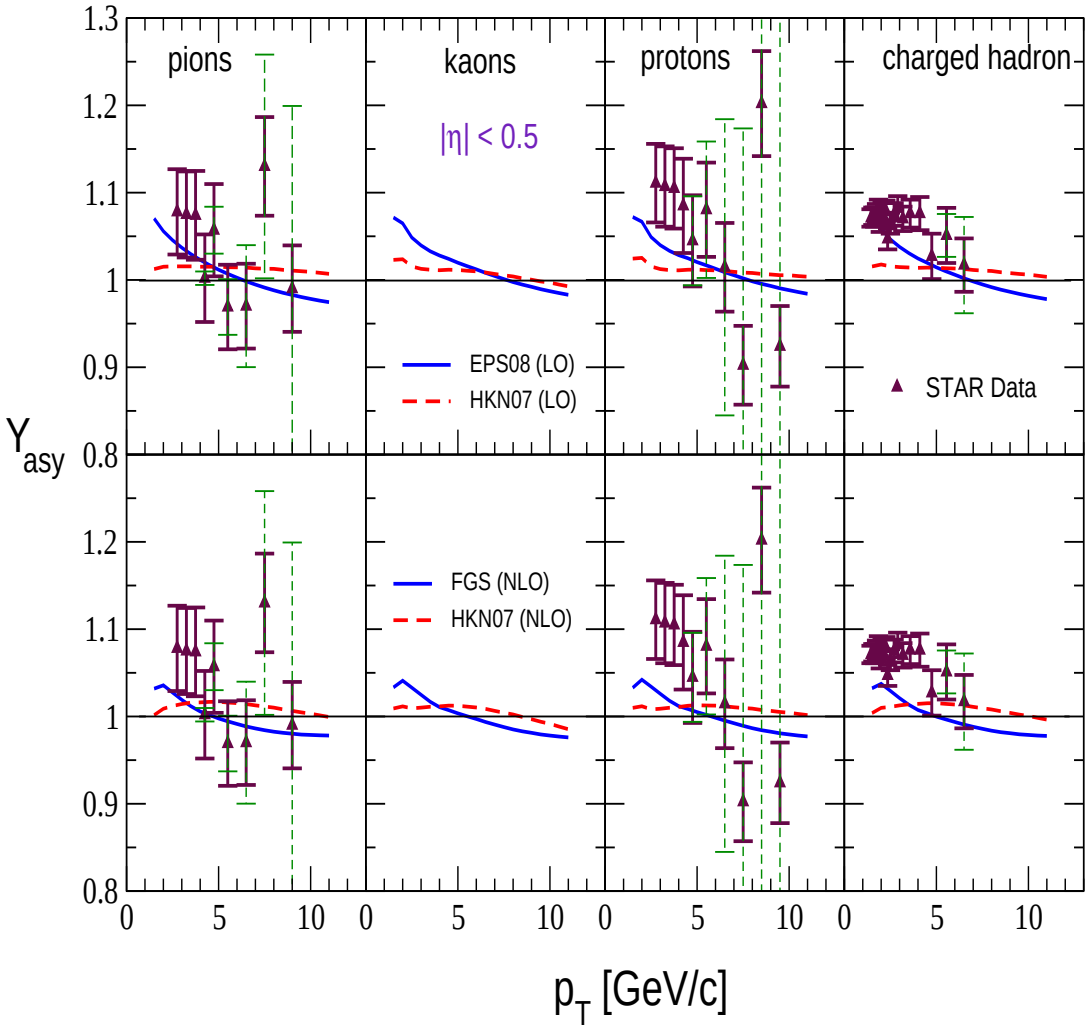


Fig. 5.6: (Color Online) Pseudorapidity asymmetry, Y_{asy} for different hadrons at $|\eta| \leq 0.5$. The solid line represents the EPS08 nPDFs (upper panels) and the FGS nPDFs (lower panels). The dashed line corresponds to the HKN07 LO (NLO) nPDFs for upper (lower) panels respectively. Filled triangles denote the STAR data. The solid error bars are systematic errors, while dashed error bars represent statistical errors.

wider range of transverse momenta. For the total charged hadrons ratio, the calculation is below the data for $p_T \lesssim 5$ GeV/c. At the present level of combined experimental and theoretical uncertainties, we can claim that $Y_{\rm asy}$ is reasonably reproduced for $\pi^+ + \pi^-$ and $p + \bar{p}$, in particular at large transverse momenta.

5.5.3 Centrality-selected asymmetry: $|\eta| \leq 0.5$

We have also calculated pseudorapidity asymmetry in two centrality classes ($0 - 20\%$ and $40 - 100\%$) for both pions and protons. The result of our calculations for pions is shown in Figure 5.7. In general, the experimental data are clustered around unity, especially for the $40 - 100\%$ centrality class. All parameterizations show trends similar respectively to those observed in the minimum bias case.

(i) pions: $0 - 20\%$ centrality class

Both EPS08 and FGS follow the trend of the data with increasing p_T, dropping below unity at higher values of p_T. The HKN07 results, on the other hand, remain essentially above unity for all p_T considered. The HKN07 underpredicts the data for the lowest p_T, where EPS08 and FGS give better agreement. For $p_T > 3$ GeV/c, all three parameterizations give good description of the data.

(ii) pions: $40 - 100\%$ centrality class

Here the data are heavily clustered around unity, and all three nPDFs considered give results reflecting this. The trends observed in both minimum bias and $0 - 20\%$ are still evident, although much less pronounced. In view of the magnitude of the error bars, all three parameterizations give good agreement with data for all p_T.

The result of our calculations for protons is displayed in Figure 5.8. Unlike the pion case, all data points are above unity for both centrality classes.

(i) protons: $0 - 20\%$ centrality class

The situation is similar to that of pion production. Both EPS08 and FGS give better reproduction of experimental data at low p_T than HKN07. For $p_T > 3$ GeV/c, all three parameterizations give reasonably good description of the data.

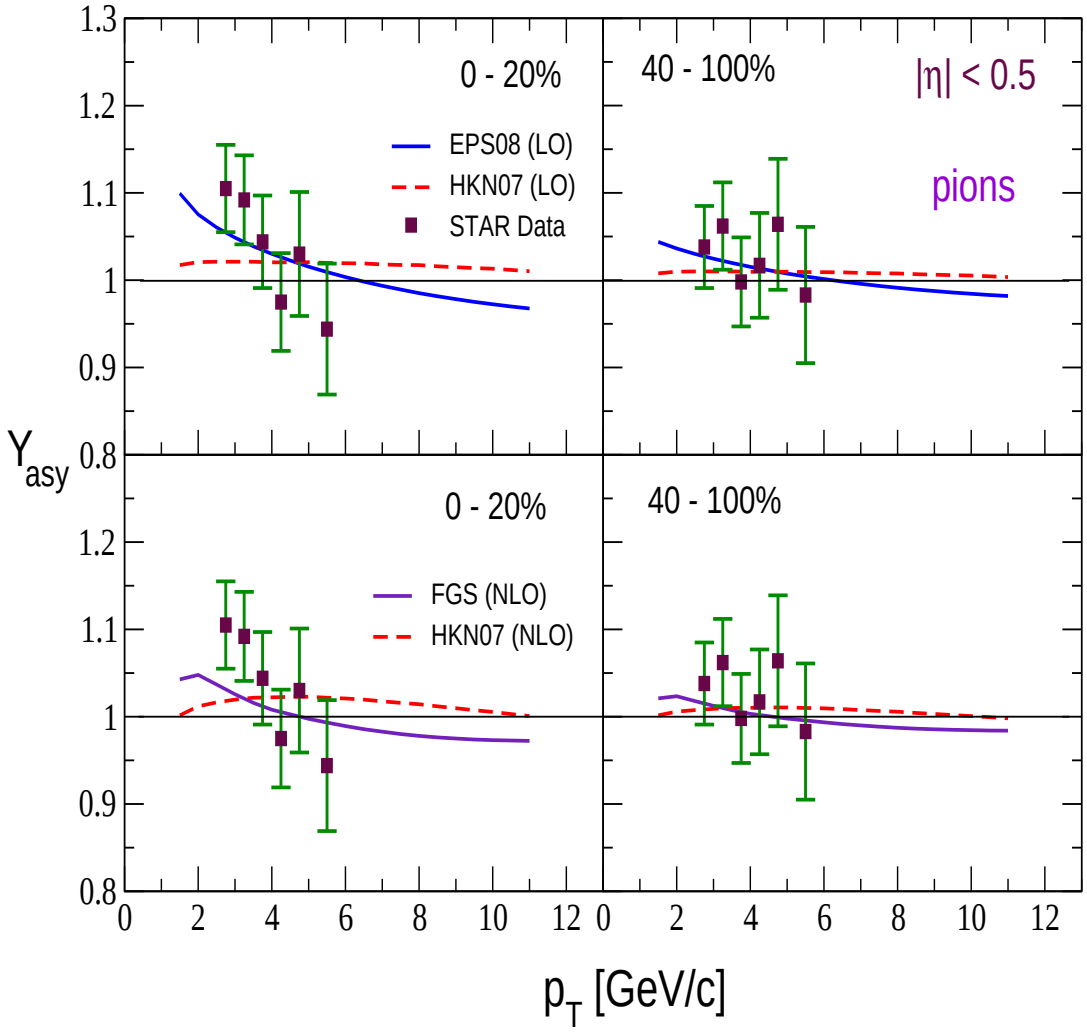


Fig. 5.7: (Color Online) Pseudorapidity asymmetry, Y_{asy}, for pions in two centrality classes at $|\eta| \leq 0.5$. The solid line represents the EPS08 nPDFs (upper panels) and the FGS nPDFs (lower panels). The dashed line corresponds to the HKN07 LO (NLO) nPDFs for upper (lower) panels respectively. Filled squares denote the STAR data.

(ii) protons: $40 - 100\%$ centrality class

The agreement with data for all four parameterizations, while reasonable, is not as good as that of the $0 - 20\%$ centrality class. All the nPDFs considered underpredict the data at low p_T, and give results close to unity.

5.5.4 Minimum-bias asymmetry: $0.5 \leq |\eta| \leq 1.0$

Figure 5.9 shows the result of our pseudorapidity asymmetry ratio calculations for the interval $0.5 \leq |\eta| \leq 1.0$. At low p_T, the situation is similar to $|\eta| \leq 0.5$. Thus the asymmetry is above unity. However, at $p_T > 3$ GeV/c, the x_b distributions start to become significantly different. While there are still some contributions from the shadowing region for the positive rapidity even up to the highest p_T, the negative rapidity yield has no shadowing contribution for $p_T \gtrsim 8$ GeV/c. Thus one expects the asymmetry to be more substantial than for $|\eta| \leq 0.5$. This is borne out by the calculations. As in $|\eta| \leq 0.5$, EPS08 and FGS give very similar results. The HKN07 nPDFs also behave similarly to what was seen at $|\eta| \leq 0.5$, the difference between EPS08 and FGS on the one side, and HKN07 on the other, becoming more pronounced. All calculations underpredict the data for $h^+ + h^-$. For $\pi^+ + \pi^-$ and $p + \bar{p}$, the calculation agrees with the data within error for large transverse momenta. It will be interesting to see the data for charged kaons, when they become available[104].

5.5.5 Centrality-selected asymmetry: $0.5 \leq |\eta| \leq 1.0$

Figure 5.10 shows the result of our calculations for pions for both centrality classes under considerations. The data shows a more pronounced asymmetry unlike the case of pion production in the interval $|\eta| \leq 0.5$. This reflects the observed trend of increasing asymmetry as one moves away from midrapidity.

(i) pions: $0 - 20\%$ centrality class

The EPS08 gives the best agreement with experimental data, reproducing nicely the trend of the data with p_T. The FGS shows a similar trend, but underpredicts the data especially at low p_T. The HKN07, as usual, has a different curvature from both EPS08 and FGS. It underpredicts the data at

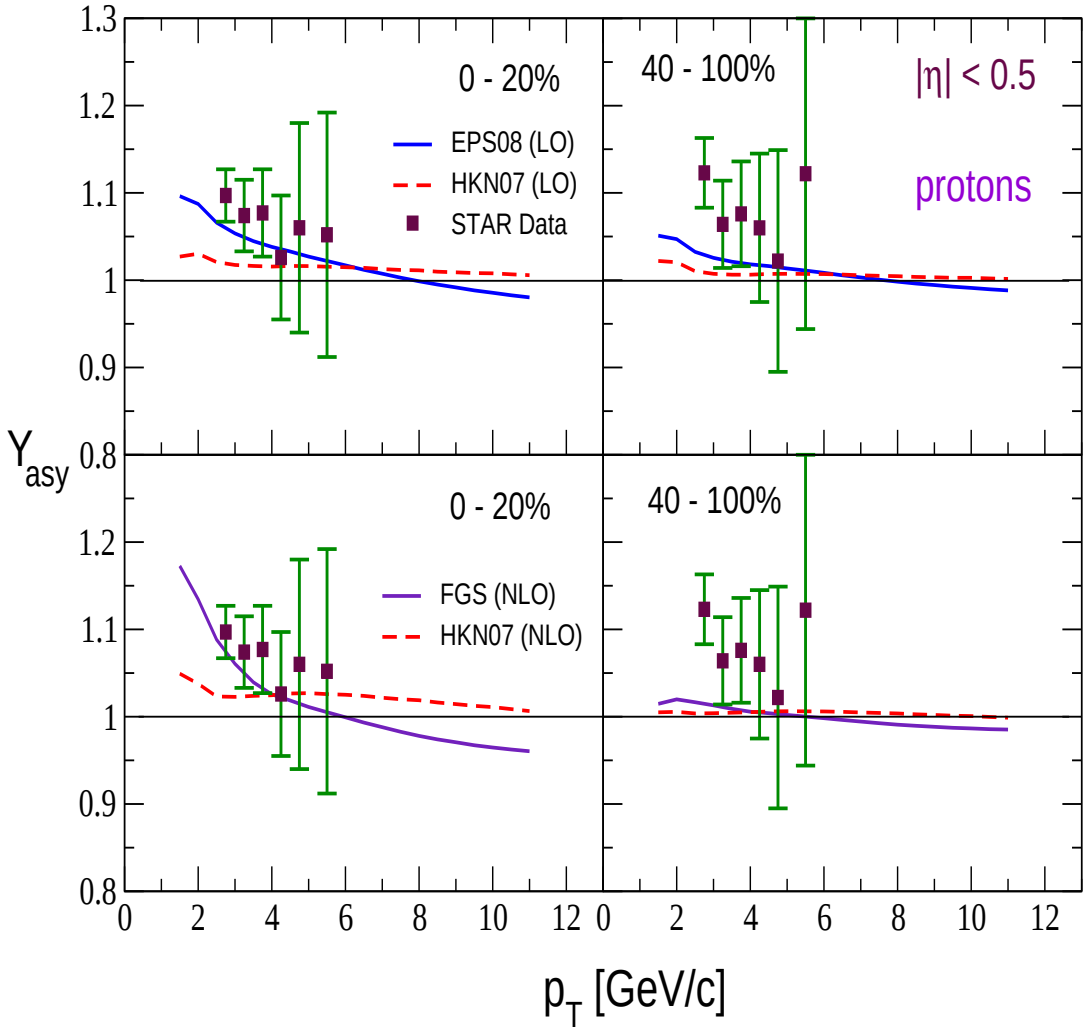


Fig. 5.8: (Color Online) Pseudorapidity asymmetry, Y_{asy}, for protons in two centrality classes at $|\eta| \leq 0.5$. The solid line represents the EPS08 nPDFs (upper panels) and the FGS nPDFs (lower panels). The dashed line corresponds to the HKN07 LO (NLO) nPDFs for upper (lower) panels respectively. Filled squares denote the STAR data.

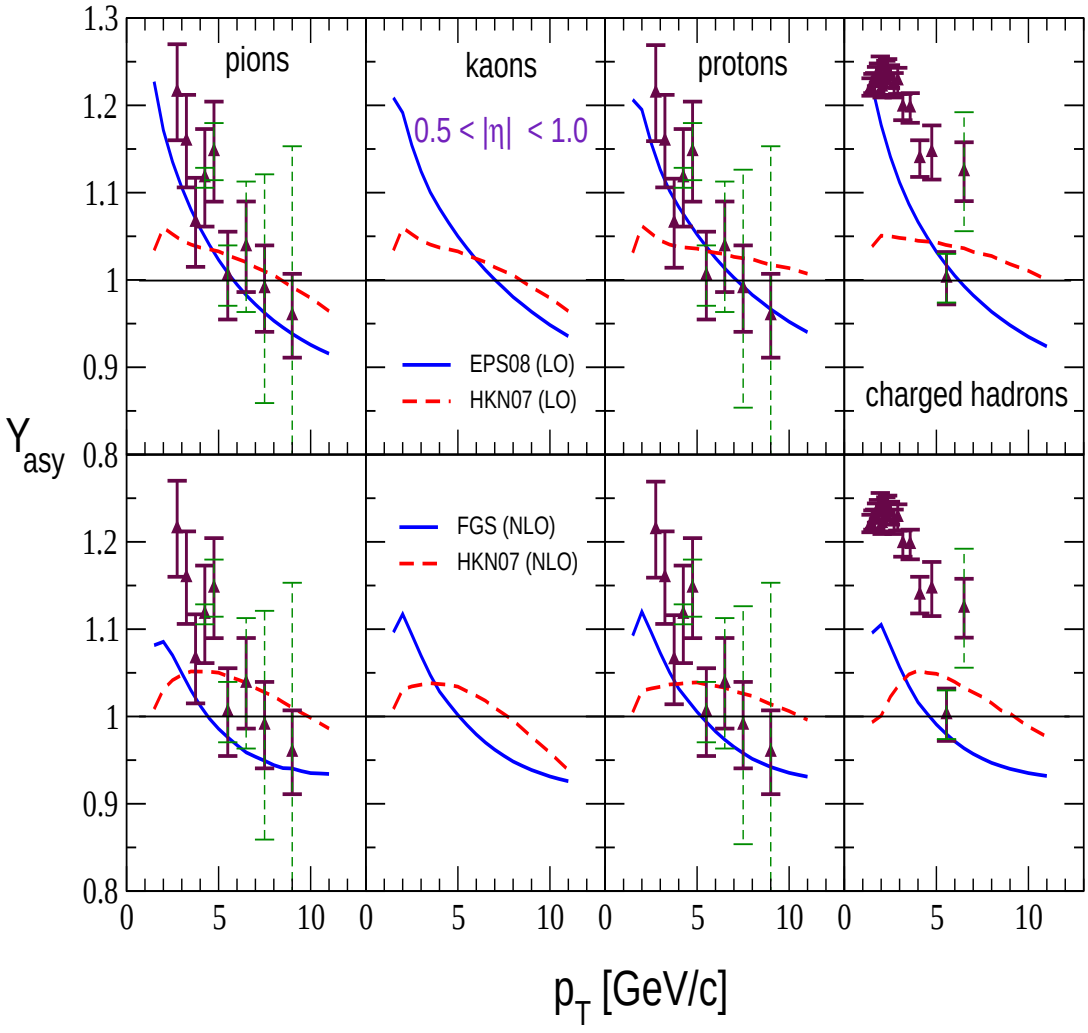


Fig. 5.9: (Color Online) Pseudorapidity asymmetry, Y_{asy} for different hadrons at $0.5 \leq |\eta| \leq 1.0$. The solid line represents the EPS08 nPDFs (upper panels) and the FGS nPDFs (lower panels). The dashed line corresponds to the HKN07 LO (NLO) nPDFs for upper (lower) panels respectively. Filled triangles denote the STAR data. The solid error bars are systematic errors, while dashed error bars represent statistical errors.

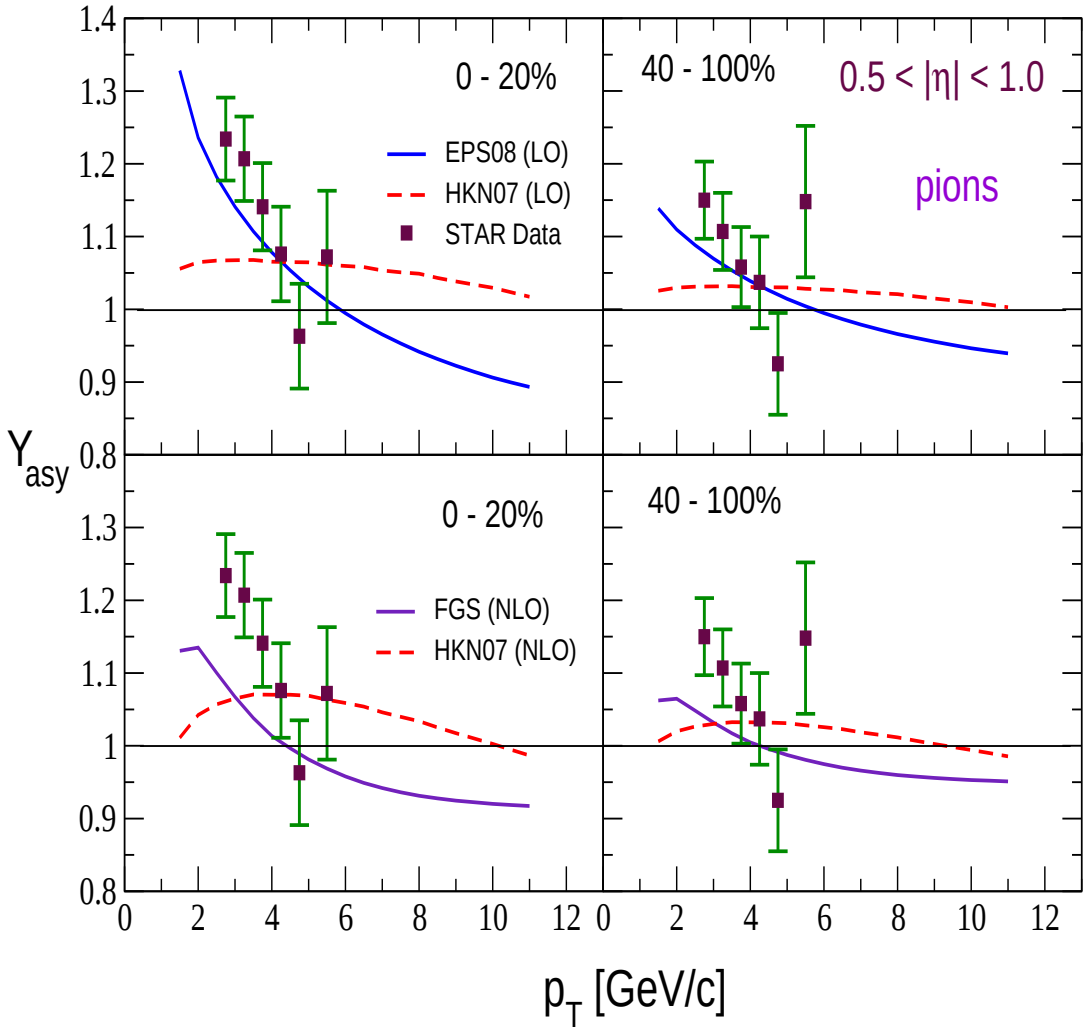


Fig. 5.10: (Color Online) Pseudorapidity asymmetry, Y_{asy}, for pions in two centrality classes at $0.5 \leq |\eta| \leq 1.0$. The solid line represents the EPS08 nPDFs (upper panels) and the FGS nPDFs (lower panels). The dashed line corresponds to the HKN07 LO (NLO) nPDFs for upper (lower) panels respectively. Filled squares denote the STAR data.

low p_T, but gives good agreement for $p_T > 3$ GeV/c.

(ii) pions: $40 - 100\%$ centrality class

The results re quite similar to those of $0-20\%$ centrality class. The EPS08 still gives the best agreement with data for most of the p_T considered. The FGS shows less underprediction than before. The behavior of HKN07 is the same as in the $0 - 20\%$ centrality class, with results closer to unity.

The results of our calculation for proton production in the two centrality classes are displayed in Figure 5.11. Both data and calculations exhibit trends similar to the pion case.

(i) protons: $0 - 20\%$ centrality class

The calculated results are similar to the pion case. The EPS08 still gives the best reproduction of data, while the FGS underpredicts the data especially at low p_T. The HKN07, while underpredicting significantly at low p_T, gives quite reasonable agreement at $p_T > 3$ GeV/c.

(i) protons: $40 - 100\%$ centrality class

Except for the lowest p_T, the data is close to unity and all three parameterizations give reasonable agreement with data. Thus both data and calculations suggest that the asymmetry for this centrality class is consistent with unity. This implies roughly equal proton production in both negative and positive pseudorapidity regions.

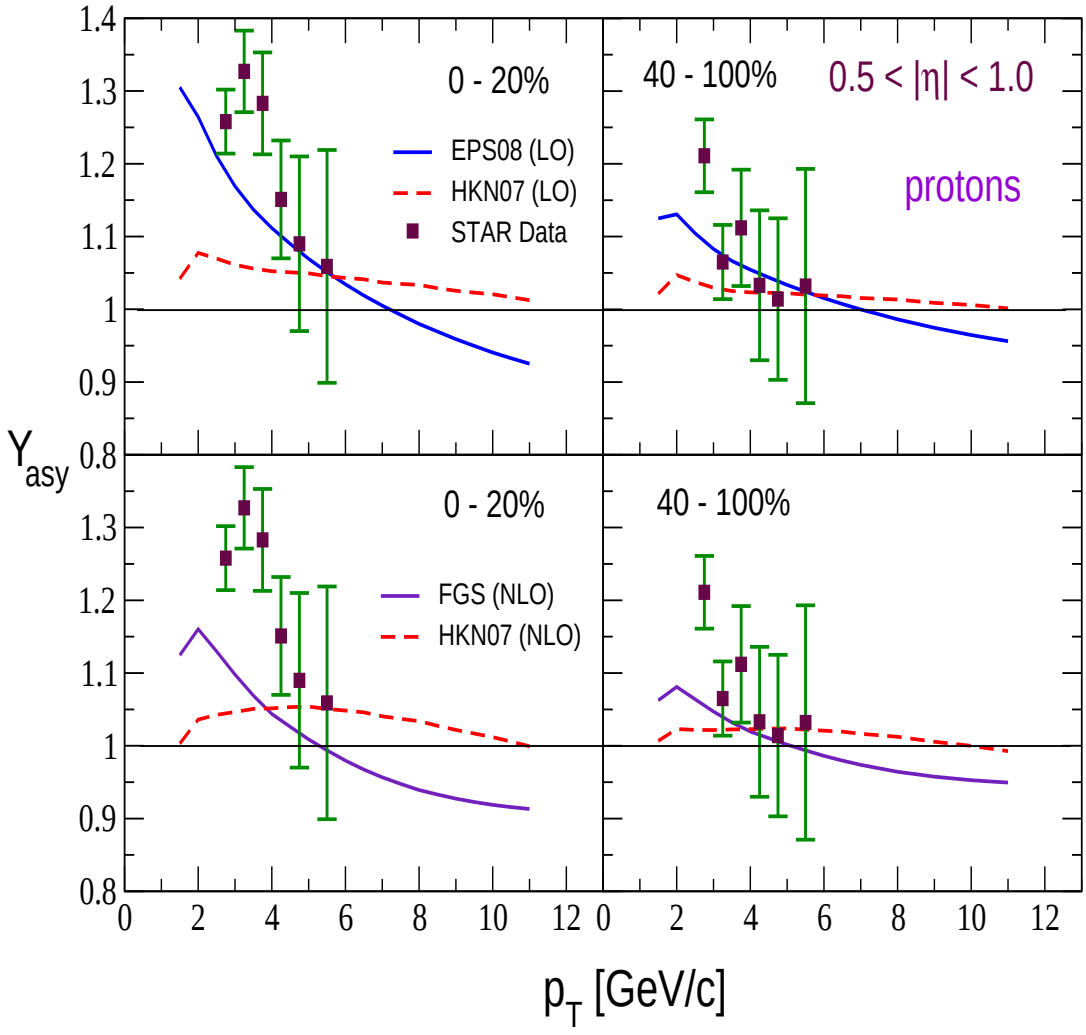


Fig. 5.11: (Color Online) Pseudorapidity asymmetry, Y_{asy}, for protons in two centrality classes at $0.5 \leq |\eta| \leq 1.0$. The solid line represents the EPS08 nPDFs (upper panels) and the FGS nPDFs (lower panels). The dashed line corresponds to the HKN07 LO (NLO) nPDFs for upper (lower) panels respectively. Filled squares denote the STAR data.

CHAPTER 6

SUMMARY AND CONCLUSION

The subject of parton distributions, even in a free nucleon, is both fascinating and quite complex. A detailed treatment involves the whole breadth of Quantum Chromodynamics (QCD): nonperturbative aspects are needed in the rigorous definition of PDFs (for example the moments of the distributions, calculable using lattice QCD) and perturbative aspect are required in their scale (Q^2) evolution. The modifications of PDFs in the nuclear environment add another layer of complexity. Different regions in the Bjorken x and scale Q^2 plane correspond to different physical phenomena (shadowing, EMC, Fermi motion, etc), which often involve quite diverse techniques to describe the physics. It is thus both necessary and economical to determine parton distributions, in free nucleons and in nuclei, from global fits to experimental data. Since the distributions are universal, they permit predictions of physical processes involving hard collisions, using the principle of factorization.

The work presented in this study can be divided into two complimentary parts. The first part deals with nuclear modifications of PDFs at small x, while the second part tests nuclear PDFs in deuteron-gold collisions. Since the subject of nuclear modifications to parton distributions is vast, we focus attention on the kinematic regime relevant to the experimental determination of nuclear modifications at very small x in the first part. Due to the correlation between x and Q^2 at fixed target experiments, small x necessarily implies small Q^2. Since data on small x nuclear modifications are only available presently from fixed target experiments, we investigate nuclear shadowing at both small x and small Q^2. In the second part, we apply the most up-to-date existing parameterizations of parton distributions (mostly from global analyses) to calculate experimental quantities which directly manifest the influence of modifications to parton distributions.

In Chapters 2 and 3 we review basic facts about parton distributions: their technical definitions, properties, and experimental determinations. These two chapters are not meant to provide a comprehensive overview; they are to summarize some definitions needed in later chapters and to give

an initial orientation. The cited references provide a more detailed and thorough coverage of the different aspects of parton distributions, in particular, areas not treated here.

Chapters 4 and 5 contain our original work. In Chapter 4 we study nuclear shadowing at small x and Q^2, the regime relevant to fixed target experiments (NMC and E665) which furnish the presently available low x data. The Gribov approach is particularly well suited for understanding small x nuclear shadowing. The physical picture is of the incident virtual photon fluctuating into an intermediate hadronic state, which then interacts coherently with more than one nucleon in the nucleus. The major requisite ingredient is thus the diffractive dissociation cross section, which includes both the resonance region and the high-mass continuum region. For the resonance region we use vector meson dominance, which accounts for the photon fluctuating into vector mesons. The high-mass region is treated using the triple-regge phenomenology. We include both the pomeron and the subleading reggeons to model the photon fluctuating into a continuum of quark-antiquark pairs. The results of our calculations are compared with experimental data from both the NMC and the E665 experiments. We find reasonably good agreement with experimental data, especially for mass numbers $A > 12$. Better agreement with data may be achieved, for $A < 12$, by using a different nuclear density distribution.

There are currently two "most recent" global analyses of nuclear parton distributions on the market: the EPS08 and the HKN07 sets. The earlier FGS parameterization uses Gribov theory and diffractive structure functions to generate parton distributions. In Chapter 5 we use these nuclear parton distributions to calculate various quantities of experimental interest. These are minimum bias nuclear modification factors, centrality-dependent modification factors (central-to-peripheral and semicentral-to-peripheral ratios), and pseudorapidity asymmetry, both minimum bias and centrality-selected. The experimental data are from BRAHMS and STAR collaborations. The modification factors from the BRAHMS experiment, both minimum bias and centrality-dependent, show a suppression with increasing pseudorapidity. The centrality dependent ratios, in particular, show a strong suppression as one moves to forward rapidities (large positive values of pseudorapidity). Our calculations give reasonable agreement with data for both minimum bias modification factors and centrality-dependent ratios around midrapidity (around $\eta = 0$). The calculations are unable to

describe the suppression of these ratios at forward rapidities, especially in the case of the central-to-peripheral (R_{CP}) ratio. The situation is slightly better for the semicentral-to-peripheral (R_{SP}) ratio, especially at higher p_T. Using different parameterizations of the spatial dependence of parton distributions is unable to cure this defect. Thus it seems likely that additional physics is needed to be able to adequately describe the data at forward rapidities.

Pseudorapidity asymmetry reveals differences between the various parton distributions that are not very apparent while considering modification factors. In general, both data and calculations are close to unity in the interval $|\eta| < 0.5$, but are enhanced as one moves from midrapidity to the interval $0.5 < |\eta| < 1.0$. Both EPS08 and FGS show quite similar behavior in the prediction of asymmetry as a function of p_T, while FGS tends to give smaller values due in part to the stronger gluon shadowing. The HKN07 set in general exhibits a different trend with p_T; it consistently underpredicts the data at low p_T and stays above unity at transverse momenta where both EPS08 and FGS are below unity. This feature is apparent for all measured hadron species and pseudorapidity intervals considered in this study.

In the interval $|\eta| < 0.5$ and for minimum bias, all three parameterizations give reasonable agreement with data for pions, protons and charged hadrons, especially for $p_T > 3$ GeV. We make predictions for the kaons. For the centrality-selected asymmetry, we also have good agreement for both pions and protons. The same trend is seen in the interval $0.5 < |\eta| < 1.0$ where, in the minimum bias case, the agreement is good for both pions and protons. For the charged hadrons the calculations generally underpredict the data, for all parameterizations. We have good agreement with data for both pions and protons for the two centrality classes presented in this study.

In conclusion, we demonstrate that a good description of nuclear shadowing at small values of x is achievable using Gribov theory and data on diffractive dissociation. We also show that nuclear modifications to parton distributions play an important role in describing experimental results on modification factors and pseudorapidity asymmetry. This work contributes to the evaluation of various competing PDF parameterizations on the market today. We can extend our calculations to higher rapidities, higher energies, and different collision systems, if and when such experimental results become available.

APPENDIX A

KINEMATICS

The use of light-cone variables, rapidity, and pseudorapidity is very common in treating high-energy scattering, particularly in hadron-hadron and lepton-hadron collisions. The essential features of these collisions that make these variables of utility are the presence of ultrarelativistic particles and a preferred axis. We collect the basic formulae in this Appendix, starting with the usual Minkowski space four-vectors.

A.1 Minkowski four-vectors and scalar product

Metric tensor: $g_{\mu\nu} = diag(1, -1, -1, -1)$

Contravariant 4-vector: $a^\mu = (a_0, \vec{a})$

Covariant 4-vector: $a_\mu = g_{\mu\nu}a^\nu = (a_0, -\vec{a})$

Scalar product: $a^2 = a_\mu a^\mu = a_0^2 - |\vec{a}|^2, \quad a \cdot b = a_\mu b^\mu = a_0 \cdot b_0 - \vec{a} \cdot \vec{b}$

Momentum 4-vector: $p^\mu = (E, p_x, p_y, p_z)$, where $E = (p^2 + m^2)^{1/2}$

A.2 Gamma Matrices

Anticommutation relations: $\{\gamma^\mu, \gamma^\nu\} = \gamma^\mu\gamma^\nu + \gamma^\nu\gamma^\mu = 2g^{\mu\nu}\,, \;\; \{\gamma^5, \gamma^\mu\} = 0$

Definition of γ^5: $\gamma_5 \equiv \gamma^5 \equiv i\gamma^0\gamma^1\gamma^2\gamma^3 = -i\gamma_0\gamma_1\gamma_2\gamma_3$

Hermitian conjugates: $\gamma^{0\dagger} = \gamma^0\,, \quad (\gamma^k)^\dagger = -\gamma^k\,, \quad (\gamma^5)^\dagger = \gamma^5\,, \quad (\gamma^\mu)^\dagger = \gamma^0\gamma^\mu\gamma^0$

Squares: $(\gamma^0)^2 = -(\gamma^k)^2 = (\gamma_5)^2 = I\,, \quad k = 1,\, 2,\, 3 \;\; I \equiv 2 \times 2$ identity matrix

A.3 Mandelstam variables

Two particles of 4-momenta p_1 and p_2 and masses m_1 and m_2 scatter to particles of 4-momenta p_3 and p_4 and masses m_3 and m_4; the Lorentz-invariant Mandelstam varaiables are defined by

$$s = (p_1 + p_2)^2 = (p_3 + p_4)^2 = m_1^2 + 2E_1E_2 - 2\vec{p_1} \cdot \vec{p_2} - m_2^2 \ , \tag{A.1}$$

$$t = (p_1 - p_3)^2 = (p_2 - p_4)^2 = m_1^2 - 2E_1E_3 + 2\vec{p_1} \cdot \vec{p_3} + m_3^2 \ , \tag{A.2}$$

$$u = (p_1 - p_4)^2 = (p_2 - p_3)^2 = m_1^2 - 2E_1E_4 + 2\vec{p_1} \cdot \vec{p_4} + m_4^2 \ , \tag{A.3}$$

and they satisfy

$$s + t + u = m_1^2 + m_2^2 + m_3^2 + m_4^2 \ . \tag{A.4}$$

A.4 Light-cone coordinates

A.4.1 Definitions

Light-cone coordinates are defined by a change of variables from the usual (t, x, y, z) or $(0, 1, 2, 3)$ coordinates. Given a vector V^μ, its light-cone components are defined by

$$V^+ = \frac{V^0 + V^3}{\sqrt{2}} \, , \quad V^- = \frac{V^0 - V^3}{\sqrt{2}} \, , \quad \vec{V}^T = (V^1, V^2) \, , \tag{A.5}$$

and $V^\mu = (V^+, V^-, \vec{V}^T)$. Thus for example,

$$\gamma^+ = \frac{\gamma^0 + \gamma^3}{\sqrt{2}} \, . \tag{A.6}$$

Some authors prefer to omit the $1/\sqrt{2}$ factor in Eq. (A.5). It can easily be verified that Lorentz invariant scalar products have the form

$$\begin{aligned} V \cdot W &= V^+W^- + V^-W^+ - \vec{V}^T \cdot \vec{W}^T \ , \\ V \cdot V &= 2V^+V^- - (V^T)^2. \end{aligned} \tag{A.7}$$

What are the motivations for defining such coordinates, which evidently depend on a particular choice of the z axis? One is that these coordinates transform very simply under boosts along the z-axis. Another is that when a vector is highly boosted along the z axis, light-cone coordinates nicely show what are the large and small components of momentum. Typically one uses light-cone coordinates in a situation like high-energy hadron scattering. In that situation, there is a natural choice of an axis, the collision axis, and one frequently needs to transform between different frames related by boosts along the axis. Commonly used frames include the rest frame of one of the incoming particles, the overall center-of-mass frame, and the center-of-mass of a partonic subprocess.

A.5 Rapidity and Pseudorapidity

A.5.1 Rapidity

A.5.1.1 Boost of particle momentum

Consider a particle of mass m that is obtained by a boost ψ from the rest frame. Its light-cone momentum is

$$\begin{aligned} p^\mu &= \left(p^+, \frac{m^2}{2p^+}, \vec{0}\right) \\ &= \left(\frac{m}{\sqrt{2}}\mathrm{e}^{\psi}, \frac{m}{\sqrt{2}}\mathrm{e}^{-\psi}, \vec{0}\right) \end{aligned} \tag{A.8}$$

Notice that if the boost is very large (positive or negative), only one of the two non-zero light-cone components of p^μ is large; the other component becomes small. With the usual components two of the components, p^0 and p^z, become large.

Suppose next that we have two such particles, p_1 and p_2, with the boost for particle 1 being much larger than that for particle 2. Then in the scalar product of the two momenta only one component of each momentum dominates the result, thus for example $(p_1 + p_2)^2 \simeq 2p_1^+ p_2^-$. This implies that, when analyzing the sizes of scalar products of highly boosted particles, it is simpler to use light-cone components than to use conventional components.

A.5.1.2 Definition of rapidity

Since the ratio p^+/p^- gives a measure $\mathrm{e}^{2\psi}$ of the boost from the rest frame, we are led to the following definition of a quantity called "rapidity":

$$y = \psi = \frac{1}{2}\ln\frac{p^+}{p^-} = \frac{1}{2}\ln\frac{E+p^z}{E-p^z}, \tag{A.9}$$

which can be applied to a particle of non-zero transverse momentum. The 4-momentum of a particle of rapidity y and transverse momentum p_T is

$$p^\mu = \left(\sqrt{\frac{m^2+p_T^2}{2}}\,\mathrm{e}^{y}, \sqrt{\frac{m^2+p_T^2}{2}}\,\mathrm{e}^{-y}, \vec{p}_T\right), \tag{A.10}$$

with $\sqrt{m^2+p_T^2}$ being called the transverse energy E_T of the particle. It can be checked that the scalar product of two momenta is

$$p_1 \cdot p_2 = E_{1T}E_{2T}\cosh(y_1-y_2) - \vec{p}_{1T}\cdot\vec{p}_{2T}. \tag{A.11}$$

In the case where the transverse momenta are negligible, this reduces to $m^2\cosh(y_1-y_2)$, which is like the formula for the product of two Euclidean vectors $\vec{p}_1\cdot\vec{p}_2 = p_1p_2\cos\theta$, with the trigonometric cosine being replaced by the hyperbolic cosine.

A.5.1.3 Transformation under boosts

Under a boost in the z direction, rapidity transforms additively:

$$y \to y' = y + \psi. \tag{A.12}$$

This implies that in situations where we have a frequent need to work with boosts along the z axis it is economical to label the momentum of a particle by its rapidity and transverse momentum, rather than to use 3-momentum.

A.5.1.4 Rapidity distributions in high-energy collisions

It also happens that in most collisions in high-energy hadronic scattering, the distribution of final-state hadrons is approximately uniform in rapidity, within kinematic limits. That is, the distribution

of final-state hadrons is approximately invariant under boosts in the z direction. This implies that rapidity and transverse momentum are appropriate variables for analyzing data and that detector elements should be approximately uniformly spaced in rapidity. (What is physically possible is to make a detector uniform in the angular variable pseudo-rapidity that I will discuss below.) This is in contrast to the situation for e^+e^- collisions where most of the interest is in events generated via annihilation into an electro-weak boson. Such events are much closer to uniform in solid angle than uniform in rapidity.

A.5.1.5 Non-relativistic limit

Observe that for a non-relativistic particle, rapidity is approximately the same as velocity along the z-axis, for then

$$y = \frac{1}{2}\ln\frac{E+p^z}{E-p^z} \simeq \frac{1}{2}\ln\frac{m+mv^z}{m-mv^z} = v^z. \tag{A.13}$$

Non-relativistic velocities transform additively under boosts, and the non-linear change of variable from velocity to rapidity allows this additive rule Eq. (A.12) to be transferred to relativistic particles (but only in one direction, the direction of boost).

One way of seeing this is as follows: The relativistic law for addition of velocities in one dimension is

$$\beta_{13} = \frac{\beta_{12}+\beta_{23}}{1+\beta_{12}\beta_{23}}, \tag{A.14}$$

where β_{12} is the velocity of some object 1 measured in the rest-frame of object 2, etc. This formula is reminiscent of the following property of hyperbolic tangents:

$$\tanh(A+B) = \frac{\tanh A + \tanh B}{1+\tanh A\tanh B}. \tag{A.15}$$

So to obtain a linear addition law, we should write $\beta_{12} = \tanh A_{12}$, and then the rule Eq. (A.14) for the addition of velocities becomes simply $A_{13} = A_{12} + A_{23}$. The A variables are exactly relative rapidities, since

$$v^z = \frac{p^z}{E} = \frac{p^+ - p^-}{p^+ + p^-} = \tanh y. \tag{A.16}$$

A.5.1.6 Relative velocity

Rapidity is the natural relativistic velocity variable. Suppose we have a proton and a pion with the same rapidity at $p_T = 0$. Then they have no relative velocity; to see this, one just boosts to the rest frame of one of the particles. But these same particles have very different energies: $E_p = \frac{m_p}{m_\pi} E_\pi$.

A.5.2 Pseudorapidity

The rapidity of a particle can easily be measured in a situation where its mass is negligible, for then it is simply related to the polar angle of the particle.

First let us define the pseudorapidity of a particle by

$$\eta = -\ln \tan \frac{\theta}{2}, \tag{A.17}$$

where θ is the angle of the 3-momentum of the particle relative to the $+z$ axis. It is easy to derive an expression for rapidity in terms of pseudorapidity and transverse momentum:

$$y = \ln \frac{\sqrt{m^2 + p_T^2 \cosh^2 \eta} + p_T \sinh \eta}{\sqrt{m^2 + p_T^2}}. \tag{A.18}$$

In the limit that $m \ll p_T$, $y \to \eta$. This accounts both for the name 'pseudorapidity' and for the ubiquitous use of pseudorapidity in high-transverse-momentum physics. Angles, and hence pseudorapidity, are easy to measure. But it is really the rapidity that is of physical significance: for example the distribution of particles in a minimum bias event is approximately uniform in rapidity over the kinematic range available.

The distinction between rapidity and pseudorapidity is very clear when one examines the kinematic limits on the two variables. In a collision of a given energy, there is a limit to the energy of the particles that can be produced. This can easily be translated to limits on the rapidities of the produced particles of a given mass. But there is no limit on the pseudorapidity, since a particle can be physically produced at zero angle (or at 180°), where its pseudorapidity is infinite. The particles for which the distinction is very significant are those for which the transverse momentum is substantially less than the mass. Note: from Eq. (A.18) it follows that $y < \eta$ always.

APPENDIX B

TRIPLE-REGGE MODEL OF HIGH-MASS CONTINUUM

In Sec. 4.3.2.3, the diffractive dissociation cross section is needed as an input to calculate the shadowing ratio. In this Apppendix we summarize the treatment of the high-mass continuum part of this cross section. The relevant diagram is shown in figure B.1.

For $W^2 \gg M_X^2$ the process $\gamma p \to Xp$ may be treated with a so-called Regge expansion. The amplitude at fixed M_X is then a sum of amplitudes for the exchange of "reggeons" i that produce all possible final states X. The corresponding cross section contains products of flux factors for reggeons i and j and amplitudes $T_{\gamma\alpha_i(t)\to X}\, T^{\star}_{\gamma\alpha_j(t)\to X}$ The generalised optical theorem relates the sum over X of these matrix elements to the forward amplitude for the process $\gamma\alpha_i(t) \to \gamma\alpha_j(t)$ at an effective centre of mass energy M_X. When M_X^2 is large by comparison with the hadronic mass scale s_0, a Regge expansion is also appropriate for the photon-reggeon scattering amplitude, such that the dissociation cross section may be decomposed into triple-Regge terms as shown in figure B.1. The cross section may then be expressed as a sum of contributions with reggeons i, j

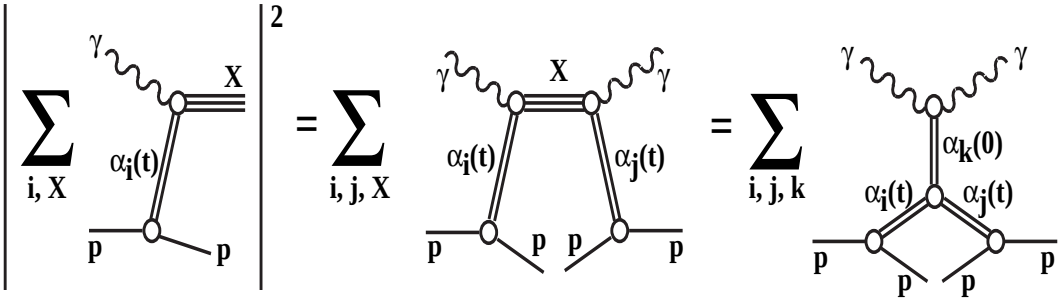


Fig. B.1: Triple-Regge model of difractive dissociation cross section

and k as

$$\frac{\mathrm{d}\sigma}{\mathrm{d}t\,\mathrm{d}M_X^2} = \frac{s_0}{W^4}\sum_{i,j,k} G_{ijk}(t)\,\left(\frac{W^2}{M_X^2}\right)^{\alpha_i(t)+\alpha_j(t)}\left(\frac{M_X^2}{s_0}\right)^{\alpha_k(0)}\cos\left[\phi_i(t)-\phi_j(t)\right]\ . \qquad \text{(B.1)}$$

The functions $G_{ijk}(t)$ and $\alpha_i(t)$ are not predicted by the model and must be determined from experimental measurements. The trajectories $\alpha_i(t)$ are assumed to take the linear form $\alpha_i(t) = \alpha_i(0)+\alpha_i' t$. The phase $\phi_i(t)$ of reggeon i is determined by the signature factor, $\eta_i(t) = \zeta + e^{-i\pi\alpha_i(t)}$, where $\zeta = \pm 1$ is the signature of the exchange. The signature factors are written as $\eta_i(t) = \eta_i^0(t)\ e^{i\phi_i(t)}$ with the moduli $\eta_i^0(t)$ absorbed into the β parameters introduced in equation (B.2). For photoproduction reggeons i and j must have the same signature such that $\phi_i(t) - \phi_j(t) = \frac{\pi}{2}\left[\alpha_j(t) - \alpha_i(t)\right]$. As is customary the scale $s_{_0}$ is set to 1 GeV^2. The functions $G_{ijk}(t)$ may be factored into products of couplings each of the form

$$G_{ijk}(t) = \frac{1}{16\pi}\ \beta_{pi}(t)\ \beta_{pj}(t)\ \beta_{\gamma k}(0)\ g_{ijk}(t)\ , \tag{B.2}$$

where the β terms describe the couplings of the reggeons to external particles and $g_{ijk}(t)$ is the appropriate three-reggeon coupling. The t dependence of the reggeon-proton and three-reggeon couplings are parameterised here as $\beta_{pi}(t) = \beta_{pi}(0)e^{b_{pi}t}$ and $g_{ijk}(t) = g_{ijk}(0)e^{b_{ijk}t}$.

The "pomeron" $\mathbb{P}$, with trajectory $\alpha_{_{\mathbb{P}}}(t)$, is unique in Regge theory in that its intercept is significantly larger than those of all other reggeons. In the limit in which both $W^2/M_{_X}^2$ and $M_{_X}^2 \to \infty$ only the $ijk = \mathbb{P}\mathbb{P}\mathbb{P}$ term survives and equation (B.1) reduces to

$$\frac{\mathrm{d}\sigma}{\mathrm{d}t\,\mathrm{d}M_{_X}^2} = \frac{G_{\mathbb{P}\mathbb{P}\mathbb{P}}(0)}{s_{_0}^{\alpha_{_{\mathbb{P}}}(0)-1}}\ \left(W^2\right)^{2\alpha_{_{\mathbb{P}}}(0)-2}\ \left(\frac{1}{M_{_X}^2}\right)^{\alpha_{_{\mathbb{P}}}(0)}\ e^{B(W^2,M_{_X}^2)\,t}\ , \tag{B.3}$$

where $B(W^2, M_{_X}^2) = 2b_{p\mathbb{P}} + b_{\mathbb{P}\mathbb{P}\mathbb{P}} + 2\alpha'_{_{\mathbb{P}}} \ln W^2/M_{_X}^2$. After the pomeron, the next-leading reggeons have approximately degenerate trajectories and carry the quantum numbers of the ρ, ω, a_2 and f_2 mesons. The reggeons under consideration are hereafter referred to as $\mathbb{P}$, ρ, ω, a and f. Their isospin, signature and C- and G-parities are $\mathbb{P}(0{+}{+}{+}{+})$, $\rho(1{-}{-}{+})$, $\omega(0{-}{-}{-})$, $a(1{+}{+}{-})$ and $f(0\,{+}{+}{+})$. In this analysis the symbol $\mathbb{R}$ is used to describe combinations of the four subleading reggeons and a single effective trajectory $\alpha_{_{\mathbb{R}}}(t)$ is assumed.

With the two trajectories, $\alpha_{_{\mathbb{P}}}(t)$ and $\alpha_{_{\mathbb{R}}}(t)$, equation (B.1) leads to a total of six terms with distinct W^2 and $M_{_X}^2$ dependences. Diffractive contributions correspond to the case where both reggeons i and j are the pomeron. In addition to the triple-pomeron diagram, a further diffractive

term arises from the $ijk = \mathbb{IP}\mathbb{IP}\mathbb{IR}$ diagram. The reggeon k must have the quantum numbers of the f meson in order to satisfy the requirements of conservation of C-parity at the photon vertex and C- and G-parity at the three-reggeon vertex.

The pomeron has $\mathbb{IP}(0 + ++)$ and is thus identical to the f meson, leading to interference. We neglect such interference effect in the present study.

The differential dissociation cross section including both the pomeron and subleading reggeons can thus be written as

$$\frac{\mathrm{d}^2\sigma}{\mathrm{d}t\,\mathrm{d}M_X^2} = \left[\frac{G_{\mathbb{IP}\mathbb{IP}\mathbb{IP}}(0)\ s_0^{1-\alpha_{\mathbb{IP}}(0)}}{M_X^{2\alpha_{\mathbb{IP}}(0)}} + \frac{G_{\mathbb{IP}\mathbb{IP}\mathbb{IR}}(0)\ \ s_0^{1-\alpha_{\mathbb{IR}}(0)}}{M_X^{4\alpha_{\mathbb{IP}}(0)-2\alpha_{\mathbb{IR}}(0)}}\right] \left(W^2\right)^{2\alpha_{\mathbb{IP}}(0)-2}\ e^{B(W^2,M_X^2)\,t}\,, \quad \text{(B.4)}$$

where $B(W^2, M_X^2) = 2b_{p\mathbb{IP}} + 2\alpha'_{\mathbb{IP}} \ln(W^2/M_X^2)$. Here $b_{p\mathbb{IP}}$ is the proton-pomeron slope parameter and $\alpha'_{\mathbb{IP}}$ is the slope of the pomeron trajectory. $\alpha_{\mathbb{IP}}$ and $\alpha_{\mathbb{IR}}$ are the pomeron and (effective) reggeon intercept respectively. We use the values in [69] for these parameters. Note that the value of $\alpha_{\mathbb{IP}}(0)$ ($\alpha_{\mathbb{IP}}(0) = 1.068 \pm 0.0492$) agrees within error with the soft pomeron intercept in Ref. [78] ($\alpha_{\mathbb{IP}}(0) \simeq 1.081$). The usual triple-pomeron approximation corresponds to putting $G_{\mathbb{IP}\mathbb{IP}\mathbb{IR}}(0) = 0$ in eq. (B.4). Note that the subleading reggeons are expected to have appreciable effects at low M_X^2 since their contribution goes like M_X^{-3} and is thus negligible at high M_X^2.

BIBLIOGRAPHY

[1] D. E. Soper, Nucl. Phys. Proc. Suppl. **53**, 69 (1997).

[2] G. Piller and W. Weise, Phys. Rept. **330**, 1 (2000).

[3] J. C. Collins and D. E. Soper, Ann. Rev. Nucl. Part. Sci. **37** (1987) 383; J. C. Collins, D. E. Soper and G. Sterman, in A. H. Mueller, ed., *P*erturbative Quantum Chromodynamics (World Scientific, 1989).

[4] G. Sterman *e*t al. (CTEQ Collaboration), Rev. Mod. Phys. **67** (1995) 157.

[5] J. C. Collins and D. E. Soper, Nucl. Phys. B **194** (1982) 445.

[6] G. Curci, W. Furmanski and R. Petronzio, Nucl. Phys. B **175** (1980) 27.

[7] J. B. Kogut and D. E. Soper, Phys. Rev. D **1** (1970) 2901; J. D. Bjorken, J. B. Kogut and D. E. Soper, Phys. Rev. D **3** (1971) 1382.

[8] Dokshitzer Y L 1977 *S*ov. Phys. JETP **46** 641 [Zh. Eksp. Teor. Fiz. **73**, 1216 (1977)].

[9] Gribov V N and Lipatov L N 1972 *S*ov. J. Nucl. Phys. **15** 438 [Yad. Fiz. **15**, 781 (1972)].

[10] Altarelli G and Parisi G 1977 Nucl. Phys. B **126** 298.

[11] H. L. Lai *e*t al. (CTEQ Collaboration), Phys. Rev. D **51** (1995) 4763.

[12] P. Anandam and D. E. Soper, World Wide Web page, "A Potpourri of Partons," http://zebu.uoregon.edu/~parton/.

[13] T. Muta, *Foundations of Quantum Chromodynamics*, (World Scientific 1987).

[14] T. P. Cheng, L. F. Li, *G*auge Theory of Elementary Particle Physics, (Oxford University Press, New York 1984).

[15] A. D. Martin, R. G. Roberts, W. J. Stirling and R. S. Thorne, Eur. Phys. J. C **23**, 73 (2002).

[16] M. Glück, E. Reya and A. Vogt, Z. Phys. C **67** (1995) 433.

[17] N. Armesto, J. Phys. G **32**, R367 (2006) [arXiv:hep-ph/0604108].

[18] P. Hoodbhoy, R. L. Jaffe and A. Manohar, Nucl. Phys. B **312**, 571 (1989).

[19] M. Arneodo *e*t al. [New Muon Collaboration], Phys. Rev. D **50**, 1 (1994).

[20] D. F. Geesaman, K. Saito and A. W. Thomas, Ann. Rev. Nucl. Part. Sci. **45**, 337 (1995).

[21] M. R. Adams *e*t al. [E665 Collaboration], Phys. Rev. Lett. **68**, 3266 (1992).

[22] M. R. Adams *e*t al. [E665 Collaboration], Z. Phys. C **67**, 403 (1995).

[23] M. R. Adams *e*t al. [Fermilab E665 Collaboration], Phys. Lett. B **287**, 375 (1992).

[24] P. Amaudruz *e*t al. [New Muon Collaboration], Nucl. Phys. B **441**, 3 (1995).

[25] M. Arneodo *e*t al. [New Muon Collaboration.], Nucl. Phys. B **441**, 12 (1995).

[26] P. Amaudruz *e*t al. [New Muon Collaboration], Z. Phys. C **51**, 387 (1991).

[27] P. Amaudruz *e*t al. [New Muon Collaboration], Z. Phys. C **53**, 73 (1992).

[28] M. Arneodo *e*t al. [New Muon Collaboration], Nucl. Phys. B **481**, 3 (1996).

[29] M. Arneodo *e*t al. [New Muon Collaboration], Nucl. Phys. B **481**, 23 (1996).

[30] W. Weise, Nucl. Phys. A **553**, 59C (1993).

[31] J. Gomez *e*t al., Phys. Rev. D **49**, 4348 (1994).

[32] A. C. Benvenuti *e*t al. [BCDMS Collaboration], Phys. Lett. B **189**, 483 (1987).

[33] G. Bari *e*t al. [BCDMS Collaboration], Phys. Lett. B **163**, 282 (1985).

[34] A. C. Benvenuti *e*t al. [BCDMS Collaboration], Z. Phys. C **63**, 29 (1994).

[35] M. Vakili *e*t al. [CCFR Collaboration], Phys. Rev. D **61**, 052003 (2000) [arXiv:hep-ex/9905052].

[36] D. M. Alde *e*t al., Phys. Rev. Lett. **64**, 2479 (1990).

[37] L. L. Frankfurt, M. I. Strikman and S. Liuti, Phys. Rev. Lett. **65**, 1725 (1990).

[38] E. L. Berger and D. L. Jones, Phys. Rev. D **23**, 1521 (1981).

[39] P. Amaudruz *e*t al. [New Muon Collaboration], Nucl. Phys. B **371**, 553 (1992).

[40] Eskola K J Nucl. Phys. B **400** 240 1993.

[41] Frankfurt L L, Guzey V, McDermott M and Strikman M I *J*HEP **0202** 027 2002.

[42] Frankfurt L L, Guzey V and Strikman M I Phys. Rev. D **71** 054001 2005.

[43] Eskola K J, Kolhinen V J and Salgado C A *E*ur. Phys. J. C **9** 61 1999.

[44] Indumathi D and Zhu W *Z*. Phys. C **74** 119 1997.

[45] Eskola K J, Kolhinen V J and Ruuskanen P V 1998 Nucl. Phys. B **535** 351

[46] Hirai M, Kumano S and Miyama M Phys. Rev. D **64** 034003 2001.

[47] Hirai M, Kumano S and Nagai T H Phys. Rev. C **70** 044905 2004.

[48] de Florian D and Sassot R Phys. Rev. D **69** 074028 2004.

[49] Accardi A *e*t al. 2004 *C*ERN Yellow Report on Hard probes in Heavy-Ion Collisions at the LHC (CERN-2004-009), Chapter 1: pdf's, shadowing and pA collisions (Geneva: CERN Scientific Information Service) (*P*reprint hep-ph/0308248) [arXiv:hep-ph/0308248].

[50] K. Ackerstaff *e*t al. [HERMES Collaboration], Phys. Lett. B **475**, 386 (2000) [Erratum-ibid. B **567**, 339 (2003)] [arXiv:hep-ex/9910071].

[51] Prytz K Phys. Lett. B **311** 286 1993.

[52] Eskola K J, Honkanen H, Kolhinen V J and Salgado C A 2002 Phys. Lett. B **532** 222

[53] Czyzewski J, Eskola K J and Qiu J W 1995 *I*II International Workshop on Hard Probes of Dense Matter (ECT*, Trento, June 1995).

[54] Li S y and Wang X N Phys. Lett. B **527** 85 2002.

[55] Collins J C, Soper D E and Sterman G *A*dv. Ser. Direct. High Energy Phys. **5** 1 1988.

[56] Emel'yanov V, Khodinov A, Klein S R and Vogt R Phys. Rev. C **61** 044904 2000.

[57] Blaizot J-P and Iancu E (eds) 2002 *Q*CD Perspectives on Hot and Dense Matter *(*NATO Science Series II: Mathematics, Physics and Chemistry vol. 87) (Kluwer Academic Publishers).

[58] Adcox K *e*t al. [PHENIX Collaboration] *N*ucl. Phys. A **757** 184 2005.

[59] Back B B *e*t al. [PHOBOS Collaboration] 2005 *N*ucl. Phys. A **757** 28

[60] Arsene I *e*t al. [BRAHMS Collaboration] *N*ucl. Phys. A **757** 1 2005.

[61] Adams J *e*t al. [STAR Collaboration] *N*ucl. Phys. A **757** 102 2005.

[62] Deshpande A, Milner R, Venugopalan R and Vogelsang W 2005 *A*nn. Rev. Nucl. Part. Sci. **55** 165

[63] Brodsky S J, Close F E and Gunion J F Phys. Rev. D **6** 177 1972.

[64] V. N. Gribov, Sov. Phys. JETP **30**, 709 (1970) [Zh. Eksp. Teor. Fiz. **57**, 1306 (1969)].

[65] Gribov V N 1969 *S*ov. Phys. JETP **29** 483 [Zh. Eksp. Teor. Fiz. **56** (1969) 892].

[66] T. J. Chapin *e*t al., Phys. Rev. D **31**, 17 (1985).

[67] J. Breitweg *e*t al. [ZEUS Collaboration], Eur. Phys. J. C **2**, 237 (1998).

[68] J. Breitweg *e*t al. [ZEUS Collaboration], Z. Phys. C **75**, 421 (1997). [arXiv:hep-ex/9704008].

[69] C. Adloff *e*t al. [H1 Collaboration], Z. Phys. C **74**, 221 (1997).

[70] S. Aid *e*t al. [H1 Collaboration], Z. Phys. C **69**, 27 (1995).

[71] M. Derrick *e*t al. [ZEUS Collaboration], Z. Phys. C **63**, 391 (1994).

[72] L. Frankfurt, V. Guzey and M. Strikman, Phys. Lett. B **586**, 41 (2004).

[73] A. Adeluyi and G. Fai, Phys. Rev. C **74**, 054904 (2006) [arXiv:hep-ph/0610214].

[74] A. Adeluyi and T. Nguyen, Phys. Rev. C **75**, 054911 (2007).

[75] T. H. Bauer, R. D. Spital, D. R. Yennie and F. M. Pipkin, Rev. Mod. Phys. **50**, 261 (1978) [Erratum-ibid. **51**, 407 (1979)].

[76] G. Piller, G. Niesler and W. Weise, Z. Phys. A **358**, 407 (1997). [arXiv:hep-ph/9707266].

[77] F. Klingl, N. Kaiser and W. Weise, "Effective Lagrangian approach to vector mesons, their structure and Z. Phys. A **356**, 193 (1996). [arXiv:hep-ph/9607431].

[78] A. Donnachie and P. V. Landshoff, Phys. Lett. B **296**, 227 (1992).

[79] K. Hagiwara *e*t al. [Particle Data Group], Phys. Rev. D **66**, 010001 (2002).

[80] L. Frankfurt, G. Piller, M. Sargsian and M. Strikman, Eur. Phys. J. A **2**, 301 (1998). [arXiv:nucl-th/9801041].

[81] V. N. Gribov and A. A. Migdal, "Properties of the pomeranchuk pole and the branch cuts related to it at low Sov. J. Nucl. Phys. **8**, 583 (1969) [Yad. Fiz. **8**, 1002 (1968)].

[82] C. W. De Jager, H. De Vries and C. De Vries, Atom. Data Nucl. Data Tabl. **14**, 479 (1974).

[83] J. Breitweg *e*t al. [ZEUS Collaboration], Eur. Phys. J. C **1**, 81 (1998) [arXiv:hep-ex/9709021].

[84] J. A. Crittenden, Tracts in Modern Physics, Volume 140, Springer 1997. arXiv:hep-ex/9704009.

[85] G. Piller, L. Ferreira and W. Weise, Eur. Phys. J. A **4**, 287 (1999) [arXiv:hep-ph/9812341].

[86] A. Capella, A. Kaidalov, C. Merino, D. Pertermann and J. Tran Thanh Van, Eur. Phys. J. C **5**, 111 (1998) [arXiv:hep-ph/9707466].

[87] N. Armesto, A. Capella, A. B. Kaidalov, J. Lopez-Albacete and C. A. Salgado, Eur. Phys. J. C **29**, 531 (2003) [arXiv:hep-ph/0304119].

[88] I. Arsene *e*t al. [BRAHMS Collaboration], Phys. Rev. Lett. **93**, 242303 (2004).

[89] B. I. Abelev *e*t al. [STAR Collaboration], Phys. Rev. C **76**, 054903 (2007) arXiv:nucl-ex/0609021. J. Adams *e*t al. [STAR Collaboration], Phys. Rev. C **70**, 064907 (2004) [arXiv:nucl-ex/0408016].

[90] A. Adeluyi and G. Fai, Phys. Rev. C **76**, 054904 (2007) [arXiv:0710.1453 [hep-ph]].

[91] A. Adeluyi, G. G. Barnafoldi, G. Fai and P. Levai, arXiv:0808.0682 [hep-ph].

[92] J. J. Aubert *e*t al. [European Muon Collaboration], Phys. Lett. B **123**, 275 (1983).

[93] S.S. Adler *e*t al. [PHENIX Collaboration], Phys. Rev. Lett. **91**, 072303 (2003); Phys. Rev. **C74**, 024904 (2006).

[94] J. Adams *e*t al. [STAR Collaboration], Phys. Rev. Lett. **91**, 072304 (2003); Phys. Rev. **C70**, 064907 (2004).

[95] H. Yang, [BRAHMS Collaboration], J. Phys. G **34**, S619 (2007) [arXiv:nucl-ex/0702004].

[96] K. J. Eskola, H. Paukkunen and C. A. Salgado, JHEP **0807**, 102 (2008) [arXiv:0802.0139 [hep-ph]].

[97] M. Hirai, S. Kumano and T. H. Nagai, Phys. Rev. C **76**, 065207 (2007) [arXiv:0709.3038 [hep-ph]].

[98] L. Hulthen and M. Sugawara, “Handbuch der Physik”, vol. 39 (1957).

[99] D. Kharzeev, E. Levin and M. Nardi, Nucl. Phys. A **730**, 448 (2004) [Erratum-ibid. A **743**, 329 (2004)].

[100] http://nn-online.org.

[101] D. de Florian, R. Sassot and M. Stratmann, Phys. Rev. D **75**, 114010 (2007). Phys. Rev. D **76**, 074033 (2007).

[102] A. D. Martin, R. G. Roberts, W. J. Stirling and R. S. Thorne, Eur. Phys. J. C **4**, 463 (1998) [arXiv:hep-ph/9803445].

[103] R. Vogt, Phys. Rev. C **70**, 064902 (2004).

[104] N. Xu, private communication (2007).